2020-04-09

# Design, Synthesis, and Characterization of New Non-Centrosymmetric Organic Crystals for Terahertz Generation

Gabriel Alejandro Valdivia-Berroeta
*Brigham Young University*

BYU ScholarsArchive Citation
Valdivia-Berroeta, Gabriel Alejandro, "Design, Synthesis, and Characterization of New Non-Centrosymmetric Organic Crystals for Terahertz Generation" (2020). *Theses and Dissertations*. 8411.
https://scholarsarchive.byu.edu/etd/8411

# Synthesis, Design, and Characterization of New Non-Centrosymmetric Organic Crystals for Terahertz Generation

Gabriel A. Valdivia-Berroeta

A dissertation submitted to the faculty of
Brigham Young University
in partial fulfillment of the requirements for the degree of

Doctor of Philosophy

David J. Michaelis, Chair
Jeremy A. Johnson, Chair
Matthew C. Asplund
James E. Patterson

Department of Chemistry and Biochemistry

Brigham Young University

# ABSTRACT

## Design, Synthesis, and Characterization of New Non-Centrosymmetric Organic Crystals for Terahertz Generation

Gabriel A. Valdivia-Berroeta
Department of Chemistry and Biochemistry, BYU
Doctor of Philosophy

Terahertz (THz) spectroscopy is an emerging technology with promising applications in imaging, homeland security, and material detection and quantification. Frequencies in the THz region can be generated by optical rectification of ultrafast near-infrared laser pulses in the presence of a nonlinear optical (NLO) materials such as organic crystals. Non-centrosymmetric organic THz generating crystals such as DAST, HMQ-TMS, and OH1 have received special attention due to the strong generated fields on the order of MV/cm. The cation of these organic salts is designed by connecting electron-donating with electron-accepting groups via a highly planar aromatic system. To improve the performance of organic crystals for THz generation, the molecular hyperpolarizability (β) can be optimized by introducing modifications in the architecture of these push-pull chromophores. However, the large dipole moments associated with molecules that have a large β promote the formation of NLO inactive centrosymmetric molecular alignments in the crystal state.

This dissertation provides important insights into the design of new push-pull chromophores that feature a) higher β values compared with state-of-the-art organic crystals, and b) non-centrosymmetric molecular packing in the crystalline state. The first strategy presented on this dissertation relates to the introduction of a triple bond instead of a double bond in the cation of DAST to improve the β parameter. The newly designed 4DEP core was combined with different anions to promote non-centrosymmetric molecular packing with almost ideal arrangements for THz generation. However, large single crystals were difficult to obtain and high THz generation was not achieved. The second strategy presented in this dissertation raises the value of β by extending the π-conjugation length in different cations with dimethylamino and methoxy electron-donating groups. A new molecular cation, 6MNEP, was found to have large β value combined with ideal non-centrosymmetric molecular packing. Combining these two factors, a ~ 75% higher performance for THz generation is expected for 6MNEP compared with DAST. Currently, we are testing different crystallization techniques to grow large single crystals of 6MNEP.

In addition to the strategies developed to increase the β parameter value, we also introduce a new molecular modification to induce non-centrosymmetric packing in organic salt THz generating crystals. This is achieved by substituting a methyl by an ethyl group in the quaternary nitrogen of hydrogen-bonded crystals. We showed the applicability of this method for changing molecular packing in the crystal state from centrosymmetric to non-centrosymmetric in two different molecular cations. We also demonstrated the generation of strong THz fields in the novel NLO crystal EHPSI-4NBS.

Keywords: Terahertz generation, non-centrosymmetric organic crystals, nonlinear optical

# ACKNOWLEDGEMENTS

I would like to express my gratitude to my family, especially my wonderful wife Priscilla, and three amazing kids, Antonella, Isidora, and Esteban. Without their help this dissertation would not be possible. The happiness and emotional support they have provided during the past five years is priceless.

Particular thanks to my advisors, Dr. David J. Michaelis, Dr. Jeremy A. Johnson and Dr. Stacey J. Smith and the other members of my PhD committee for their valuable suggestions and guidance.

I am very grateful to all the graduate and undergraduate students that have helped me during this amazing experience, including, Michael Kinghorn, Jacob Parkman, Adam Wayment, Chloe Ence, Erin Martinez, Hadi Nazari, Millicent Campbell, Sevanna Ahern, Lindsey Foote, Erika Jackson, Karissa Kenney, Daniel Brock, Zac Zaccardi, Bruce Wayne, Ryan Carter, Jess DeLange, Sydney Fuller, Isaac Tangen, Charlie Bahr, Larry Heki, Emmalee Mc Murray, and Steven Kauwe.

TABLE OF CONTENTS

TABLE OF FIGURES

# LIST OF TABLES

# Chapter 1 Theoretical background

## 1.1 Introduction

Terahertz (THz) radiation covers the electromagnetic spectrum from 0.1 to 10 THz (30 μm - 3mm) and it is located between infrared and microwave radiation. This frequency region was formerly known as the terahertz gap because only in the last few years optic components and ultrafast lasers have been developed to generate high-field THz radiation.[1] Inorganic and organic materials show vibrations that have resonance in the THz region, similar to what has been observed in infrared (IR) spectroscopy. However, some materials such as paper, cloth, and plastic, which are opaque in the near-infrared region, are transparent to THz radiation. This unique property, in conjunction with high sensitivity to water,[2] makes THz radiation a promising alternative for imaging applications.

The unique capabilities of THz waves have been leveraged to develop technological applications in the pharmaceutical and food industry,[3] biology, imaging,[4] homeland security,[5] and spectroscopy.[6] For instance, drug tablet coating integrity and thickness can be assessed fast and non-destructively using THz pulses.[4] This technique contrasts with time-consuming one-tablet analysis usually performed in drug quality control laboratories. Similarly, fast pulses of THz radiation have been employed to quantitatively analyze water content in dried food, taking advantage of the high-sensitivity of THz for water molecules.[7] The non-ionizing and material-penetrating nature of THz radiation has been utilized to image dangerous objects, such as ceramic knives and plastic explosives, that are not identifiable with metal detectors.[8]

In the medical field, fast and non-invasive THz methods to detect epithelial cancer and assess skin burn damage have been developed.[9] These measurements identify cancerous or damaged tissue based on the water content of epithelial cells.[10] At the molecular level, the THz susceptibility of water molecules has been used to probe hydration dynamics in biomolecules.[11] Another unique capability of THz waves is the possibility of obtaining spectral information with just one pulse of broadband frequency. Single-pulse measurements enable fast fingerprint spectroscopic identification of different chemical compounds. For instance, spectral discrimination of single-base changes in DNA is possible because of distinct spectral features present in the THz region.[12] Even in more challenging cases such as lactose sample featuring different crystalline polymorphs, THz spectroscopy has been able to differentiate between them.[13] Other applications using fingerprint spectroscopy have been developed to detect food oils,[14] antibiotics in food matrices, pesticides in fruits, and to discriminate between saturated versus unsaturated fatty acids.[7] In addition to these qualitative studies, quantification of acid compounds in seed oils was achieved and showed results comparable to high-performance liquid chromatography.[15]

To date, THz radiation has been generated using laser-based methods including photoconductive antennas,[16] laser-induced plasma generation,[17] and optical rectification in nonlinear optical crystals.[18] Optical rectification shows the most promising results with generated electric fields in the order of GV/m.[19] These strong fields have been obtained using non-centrosymmetric organic crystals, which are characterized by their low dielectric constant, high nonlinear susceptibility, and improved performance compared with inorganic counterparts.

In this dissertation, we present the design, synthesis, and characterization of novel non-centrosymmetric crystals for THz generation. To achieve this goal, organic molecules were designed to optimize the hyperpolarizability. Then the most promising molecules were synthesized and crystallized. To evaluate the centro or non-centrosymmetric nature of the crystals obtained in this way, single-crystal x-ray diffraction experiments were performed. Then, non-centrosymmetric crystals were grown by the slow evaporation method. Finally, we tested the crystals to evaluate the THz generation profile and compare them with state-of-the-art organic THz generating crystals.

In this chapter, we cover foundational aspects of the techniques and methods utilized in the development of this work designing new organic THz generators. Section 1.2 discusses the design and organic synthesis of new molecules for THz generation. In section 1.3, the basics of X-ray diffraction and the methodology to grow and characterize the crystal structures of the new materials are reviewed. Finally, in Section 1.4, we present a brief explanation of THz generation by optical rectification and the detection of these frequencies using electro-optic sampling.

## 1.2 Design and synthesis of organic molecules for THz generation

Efficient THz generation in molecular crystals is achieved by designing molecules with high hyperpolarizability values that feature non-centrosymmetric conformations in the crystalline state. The hyperpolarizability (β) is a measure of how easily a dipole moment can be induced in the presence of an electric field, in our case an infrared laser, and is directly related to the magnitude of the second-order nonlinear susceptibility ($\chi^{(2)}$).[20] In order to optimize β, push-pull π-conjugated molecules with large dipole moments are utilized in the design of organic NLO materials.[21] In this section, we will discuss the computational methods employed to design this class of molecules and the organic synthetic strategies to synthesize them in the laboratory. We will also discuss the main challenges encountered in attempting to achieve non-centrosymmetric packing in the solid state.

### 1.2.1 Push-pull chromophores design

Push-pull chromophores are designed to feature electron-donating (ED) and electron-accepting (EA) groups on opposite sides of the organic framework. These groups are connected by a π-conjugated bridge, which increases both the planarity of the molecular system and the β parameter value. **Figure 1.1a** shows the different ED and EA groups that have been utilized in the design of push-pull chromophores and applied in high field THz generation.[22] **Figure 1.1b** shows the molecular structures of three common molecules used for THz generation, including DAST (4-N,N-dimethylamino-4'-N'-methyl-stilbazolium tosylate),[23] OH1 (2-(3-(4-Hydroxystyryl)-5,5-dimethylcyclohex-2-enylidene)malononitrile),[24] and HMQ-TMS (2-(4-hydroxy-3-methoxystyryl)-1-methylquinolinium 2,4,6-trimethylbenzenesulfonate).[25] DAST features a dimethylamino ED group connected through a styryl π-bridge to an EA methyl pyridinium group. On the other hand, OH1 and HMQ-TMS share a hydroxyl ED moiety connected through the same styryl bridge to malononitrile and quinolinium accepting groups, respectively. The additional methoxy group in HMQ-TMS is not located in a conjugated position with respect to the π-system and therefore its contribution to the hyperpolarizability of the molecule is not significant. The strength of each ED and EA groups can be increased by varying its identity or by substituting it at different positions in the aromatic system. Increasing the planarity and conjugation length of the π system also have positive impacts on the value of β. To obtain a better idea of the combined effects of the mentioned factors, quantum chemical calculations can be performed in order to predict β-values for specific derivatives, as will be described below.

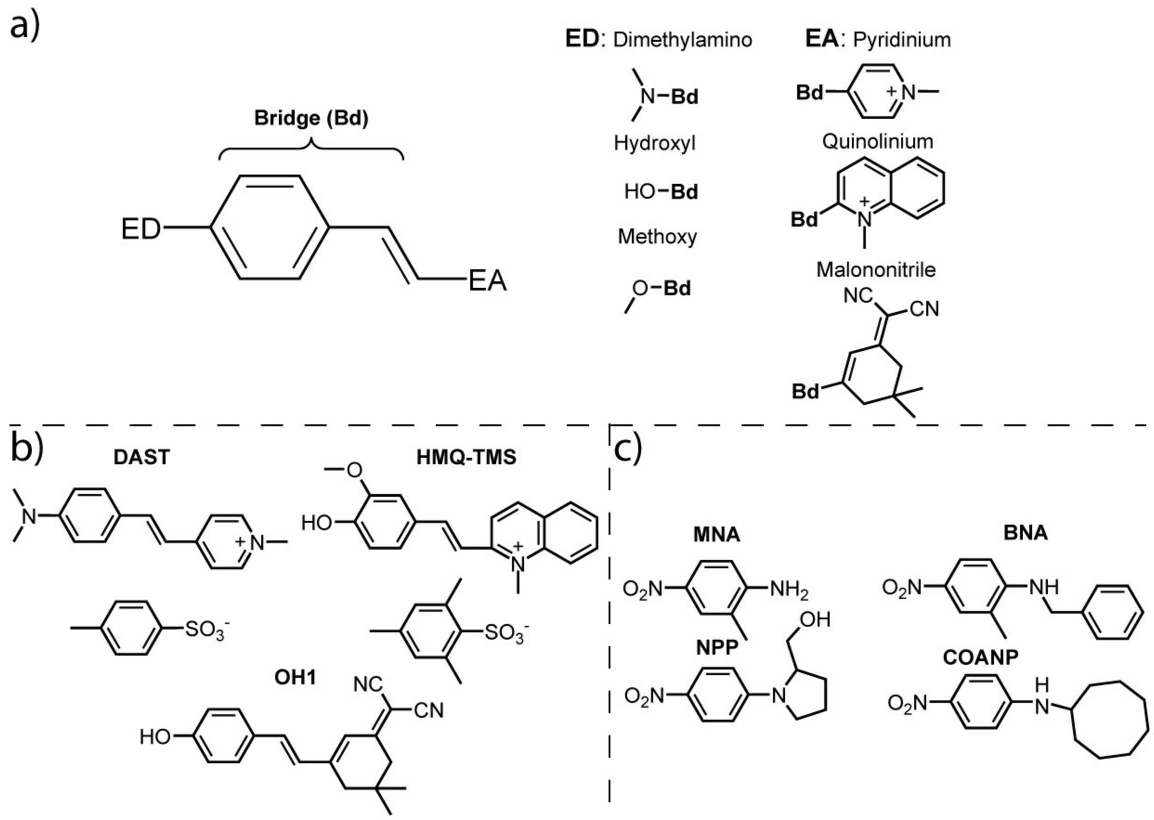

**Figure 1.1** a) Push-pull chromophores design strategy, b) push-pull molecules with known THz generating properties, c) push-pull aniline type molecules.

As depicted in **Figure 1b**, HMQ-TMS and DAST are organic salts, while OH1 is a neutral molecule. Organic salts have been employed in the design of new THz generation molecules due to their increased melting points and improved crystallization behavior compared to their neutral counterparts. A high melting point helps to prevent crystal degradation upon irradiation. Improved crystallization behavior facilitates the growth of large single crystals that can generate high-field THz radiation. As shown in **Figure 1c,** neutral aniline-type molecules have also been employed for THz generation applications (MNA, BNA, etc.). Despite their reduced conjugation length, these chromophores have shown excellent optical properties and low maximum absorption wavelengths that reduce photo damage and increase THz generation output. To date, BNA has received special attention for THz generation applications due to its ease of crystallization and broadband generated spectra.[26]

### 1.2.2 Strategies to obtain non-centrosymmetric organic crystals

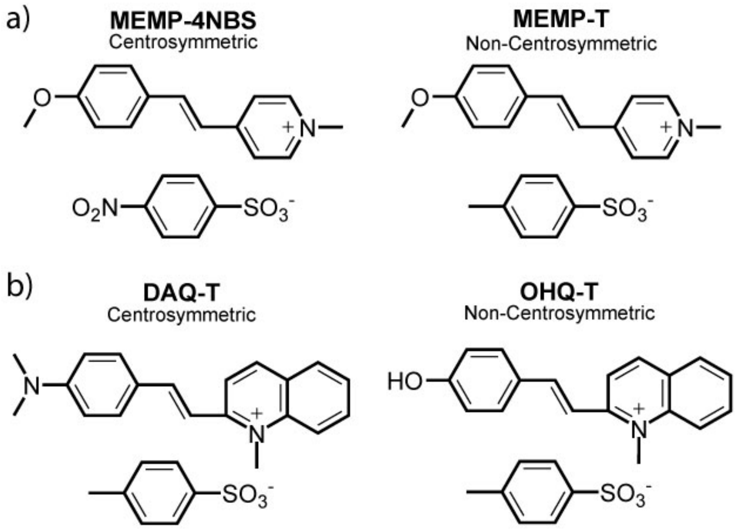

**Figure 1.2** Non-centrosymmetric engineering strategies. a) Anion exchange example in MEMP-4NBS and MEMP-T, b) Hydrogen bond networking example in DAQ-T and OHQ-T.

Due to the large magnitude of the molecular dipole moment in push-pull chromophores, there is a strong tendency of these molecules to pack in a centrosymmetric fashion. This centrosymmetric alignment of molecules within a crystal causes the macroscopic second-order NLO response to cancel to zero. A proven approach to obtain non-centrosymmetric molecular packing is to synthesize organic salts that pair a highly conjugated cation with different anions. Unique anion structures promote different intermolecular interactions with the cation and therefore can lead to non-centrosymmetry within the crystal.[27] This situation is observed in **Figure 1.2a** with the molecular cation MEMP ((E)-4-(4-methoxystyryl)-1-methylpyridin-1-ium) showing centrosymmetric packing when paired with a 4NBS (4-nitrobenzenesulfonate) anion and non-centrosymmetric alignment when combined with a T (4-methylbenzenesulfonate) anion. Another conventional approach to promote head-to-tail conformations is to use hydrogen bond donors and acceptors on opposite sides of the chromophores. This strategy is illustrated in **Figure 1.2b** by comparing the centrosymmetric compound DAQ-T (2-(4-(N,N-dimethylamino)styryl)-1-methylquinolinium 4-

methylbenzenesulfonate),[28] featuring a dimethylamino ED group and a quinolinium accepting group, with non-centrosymmetric OHQ-T (2-(2-(4-Hydroxyphenyl)vinyl)-1-methylquinolinium 4-methylbenzenesulfonate),[29] possessing a hydroxyl group in place of the dimethylamino moiety (see diagrams of donor and acceptor groups in **Figure 1.1a**). Unfortunately, this exchange of electron donor groups from DAQ to OHQ decreases β, and therefore reduces its efficiency for potential NLO applications.

### 1.2.3 Hyperpolarizability DFT calculations

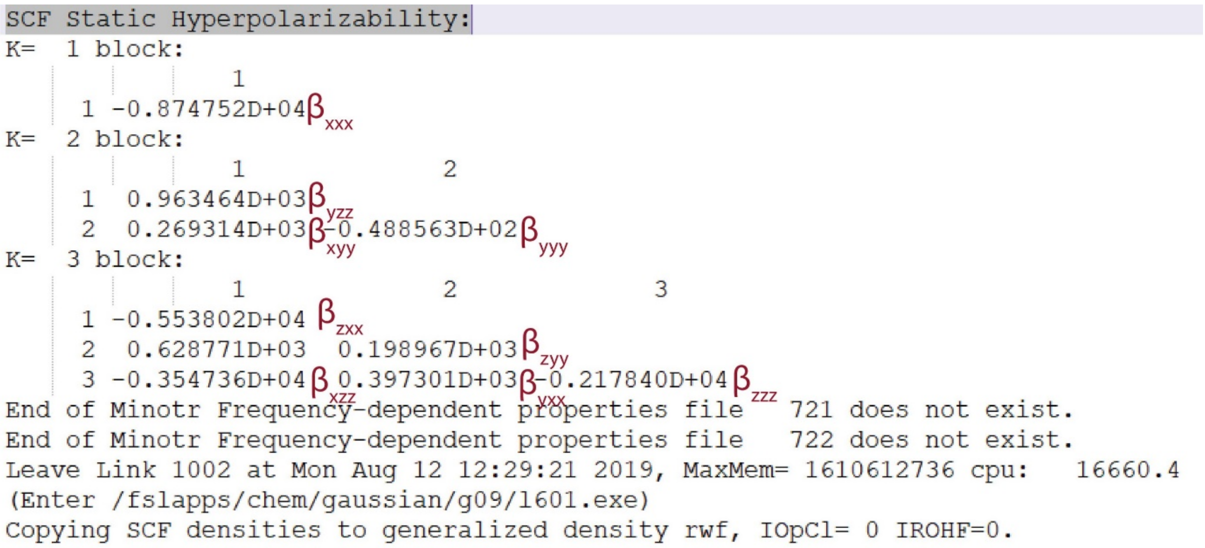

```
SCF Static Hyperpolarizability:
K=  1 block:
                  1
    1 -0.874752D+04
K=  2 block:
                  1             2
    1  0.963464D+03
    2  0.269314D+03 -0.488563D+02
K=  3 block:
                  1             2             3
    1 -0.553802D+04
    2  0.628771D+03  0.198967D+03
    3 -0.354736D+04  0.397301D+03 -0.217840D+04
End of Minotr Frequency-dependent properties file   721 does not exist.
End of Minotr Frequency-dependent properties file   722 does not exist.
Leave Link 1002 at Mon Aug 12 12:29:21 2019, MaxMem= 1610612736 cpu:   16660.4
(Enter /fslapps/chem/gaussian/g09/l601.exe)
Copying SCF densities to generalized density rwf, IOpCl= 0 IROHF=0.
```

**Figure 1.3** Gaussian calculation output example. The different components of the hyperpolarizability are marked in red.

As mentioned above, β is a guiding parameter in designing push-pull chromophores. In order to hasten the discovery process, estimates of β can be obtained using Density Functional Theory (DFT) and then comparisons can be made with state-of-the-art THz generating molecules. These quantum chemical calculations are mostly performed using finite field setups to account for non-perfectly planar molecules.[30] Reliable results can be obtained by performing geometry optimization calculations and then, once the conformational energy of the molecule is minimized, frequency calculations are performed to obtain the different components of β. This two-step process can be easily implemented using the Gaussian package.[31] **Figure 1.3** shows an example of a Gaussian output file, where the different components of the hyperpolarizability are indicated with red text. These components are then utilized to obtain $\beta_{tot}$ according to equations 1.1 and 1.2:

$$\beta_i = \sum_j \left(\beta_{ijj} + \beta_{jij} + \beta_{jji}\right) \qquad \textbf{Eq. 1.1}$$

$$\beta_{tot} = \sqrt{\beta_x^2 + \beta_y^2 + \beta_z^2} \qquad \textbf{Eq. 1.2}$$

### 1.2.4 Synthesis of push-pull chromophores

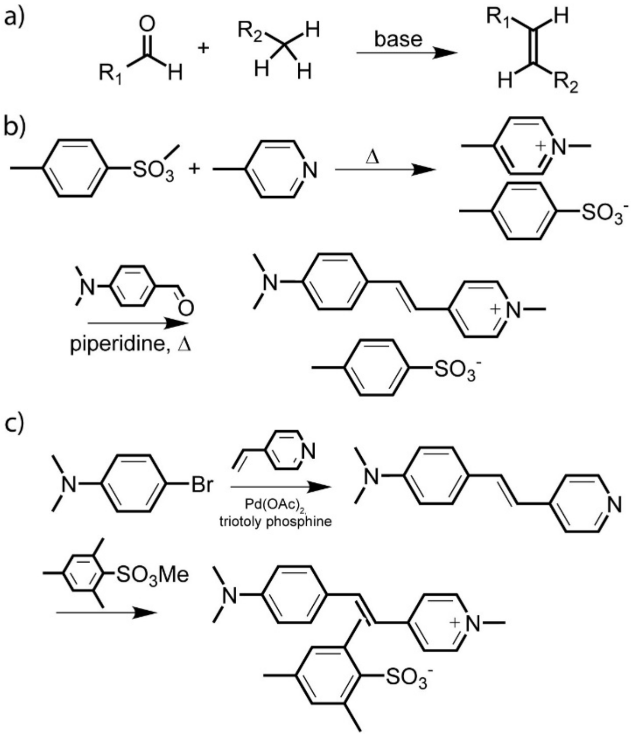

**Figure 1.4** Synthetic pathways and reactions to produce push-pull chromophores. a) condensation reaction between an aldehyde and an activated methyl, b) Synthesis of DAST, c) Sonogashira and Heck cross-coupling reactions with Pd catalysts, d) synthesis of DSTMS using a Heck reaction.

Due to the extended π systems present in organic THz generating molecules, condensation reactions are usually employed in the synthetic process. As shown in **Figure 1.4a**, a typical condensation reaction for making push-pull chromophores combines an aldehyde with an activated methyl containing-molecule to generate a carbon-carbon double bond in the presence of a weak base.[32] **Figure 1.4b** shows the reaction pathway for the synthesis of DAST, where a dimethylamino group is utilized as an electron donor. The strong electron-accepting pyridinium group is formed by reaction of 4-methylpyridine with methyl toluenesulfonate, followed by condensation with 4-dimethylaminobenzaldehyde in the presence of piperidine as base.[23] HMQ-TMS and OH1 (See Figure 1b) are synthesized similarly, with hydroxyl donating groups, and quinolinium and malononitrile EA groups, respectively. An important practical advantage of this type of reaction is the possibility of implementing simple and fast crystallization procedures for purification purposes.

Other condensation reactions rely on palladium catalysts to create push-pull chromophores. **Figure 1.4c** shows the synthesis of DSTMS (4-N,N-dimethylamino-4'-N'-methyl-stilbazolium 2,4,6-trimethylbenzenesulfonate), a DAST analog, using a Heck condensation reaction.

## 1.3 Crystalline materials

Crystalline materials consist of highly ordered, repeating arrangements of atoms. As depicted in **Figure 1.5a** for a simple 2-dimensional lattice, identical points in the crystal are known as lattice points. Neighboring lattice points can be connected to form a block-like shape. Somewhat like bricks in a wall, these small repeating units in a crystal are known as unit cells. As seen in **Figure 1.5b,** the unit cell is defined by three vectors (**a**, **b**, and **c**) related to each other by three angles ($\alpha$, $\beta$, and $\gamma$) in a right-handed coordinate system. Unit cells can be classified into seven crystal systems according to the dimensions of the constituting vectors and angles, as detailed in **Table 1.1**.

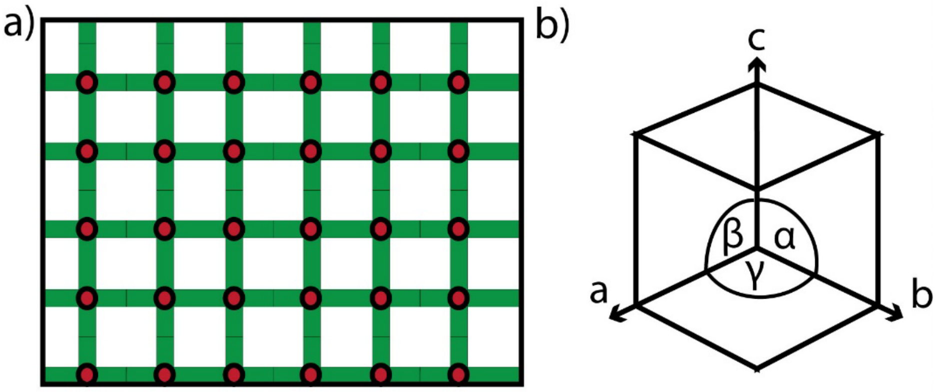

**Figure 1.5** a) Lattice points (red circles) in a regular arrangement b) Unit cell representation with axes a, b, c and angles $\alpha$, $\beta$, $\gamma$.

There are also four possible arrangements of lattice points within a unit cell, known as lattice centerings. The feasible lattice centerings are:

- Primitive (P): Lattice points are located only in the corners of the unit cell.

- Body Centered (I): Lattice points are located at corners and in the geometrical center of the unit cell.
- Face Centered (F): Lattice points are located at corners and at the center of each face of the unit cell.
- Centered (C): Lattice points are located at corners and at the center of just one set of unit cell faces.

By combining the seven crystal systems with the four possible lattice centerings, fourteen unique crystal lattices can be obtained. These are called Bravais lattices. As observed in **Table 1.1**, the different centerings are not present in every crystal system because not all result in unique lattices.

**Table 1.1** Crystal systems and unique centerings.

| Crystal system | Dimensions | Centering |
|---|---|---|
| **Triclinic** | $a \neq b \neq c$<br>$\alpha \neq \beta \neq \gamma$ | P |
| **Monoclinic** | $a \neq b \neq c$<br>$\beta \neq \alpha = \gamma = 90°$ | P, C |
| **Orthorhombic** | $a \neq b \neq c$<br>$\alpha = \beta = \gamma = 90°$ | P, I, F, C |
| **Tetragonal** | $\mathbf{a} = \mathbf{b} = \mathbf{c}$<br>$\alpha = \beta = \gamma = 90°$ | P, I |
| **Trigonal** | $\mathbf{a} = \mathbf{b} = \mathbf{c}$<br>$\alpha = \beta = \gamma \neq 90°$ | P |
| **Hexagonal** | $a = b \neq c$<br>$\alpha = \beta = 90°, \gamma = 120°$ | P |
| **Cubic** | $\mathbf{a} = \mathbf{b} = \mathbf{c}$<br>$\alpha = \beta = \gamma = 90°$ | P, F, I |

The unit cell is often considered to be the smallest repeating unit that can form crystalline materials. However, this is only if simple translations are considered. A smaller building block can be identified if all symmetry operations are considered (**Table 1.2**); the "asymmetric unit" is the smallest portion of a crystal that can generate the whole 3D crystalline array by performing all point and translational symmetry operations valid for that crystal. The asymmetric unit is generally found inside the unit cell, and for organic molecules, the asymmetric unit usually corresponds to a single molecule or a fraction of it if the molecule possesses internal symmetry.

**Table 1.2** Point and translational symmetry operations valid for crystalline materials.

| **Symmetry operation** | **Description** |
|---|---|
| **Point operations** | |
| n-fold rotation | 360°/n rotation, n is an integer |
| Mirror reflection | reflection with respect to a plane |
| Inversions | change every *x*, *y*, *z* coordinate to -*x*, -*y*, -*z* |
| Improper rotations | rotation and then inversion |
| **Translational operations** | |
| Screw axis | 360°/n rotation followed by m/n translation along the rotation axis. Denoted as $n_m$ |
| Glide planes | reflection across a mirror plane followed by a translation |

### 1.3.1 X-ray diffraction principles

The diffraction phenomenon originates from scattered waves. If the size and spacing of the scatterers is similar to the wavelength of the waves, then each scatterer becomes a point source of secondary spherical waves. When the waves overlap, destructive or constructive interference can be produced, as seen in **Figure 1.6a**. If the scatterers are arranged in a regular array, then a pattern of constructive and destructive interference will be observed at specific angles. This resulting pattern is known as diffraction.

In atoms, electron clouds act as scatterers due to their interaction with the oscillating electric field of electromagnetic radiation. Crystals will diffract X-rays because the size and spacing of atoms in a crystal is in the same order of magnitude as X-ray wavelengths, which is in order of Angstroms (Å, $10^{-10}$ m).

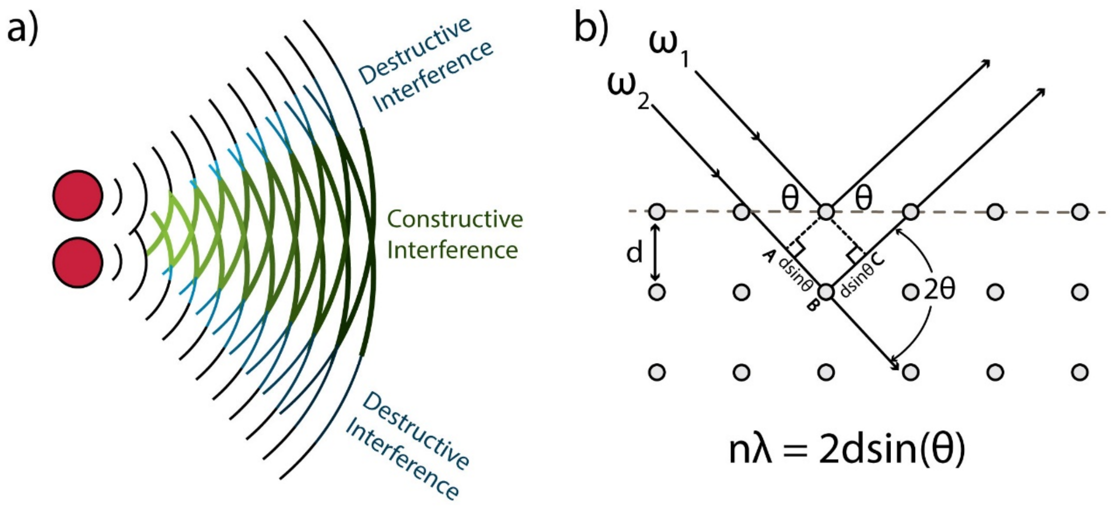

**Figure 1.6** a) Destructive and constructive interference from point sources of spherical waves, b) Bragg's Law scheme (top) and equation (bottom). Incident waves ($\omega_1$ and $\omega_2$) scattered from different planes will travel different distances before and after scattering, corresponding to segments AB + BC in the figure. If this path difference ($2d\sin\theta$) equals an integer multiple of the wavelength ($n\lambda$), constructive interference occurs.

The angles at which constructive interference will occur for a particular crystal were first deduced by William Henry Bragg and William Lawrence Bragg in 1913.[33] The Braggs treated diffraction as if it were a reflection from parallel planes of atoms separated by a distance *d*. As seen in **Figure 1.6b,** the reflection of X-rays is assumed to be coherent, with the angle of incidence and reflection being the same. The scattering from different planes will be in phase only if the difference in path length for consecutive waves (see $\omega_1$ and $\omega_2$ in **Figure 1.6b**) is an integer multiple of the wavelength. Using simple geometry, this difference in path length can be seen to equal $2d\sin(\theta)$. This gives rise to the simple equation given in Figure 2b known as the Bragg equation, which relates the diffraction angle ($\theta$) to crystal structure ($d$).

Because each point of diffracted light can be mathematically related to the *d*-spacing of a single set of planes within a crystal, it is useful to identify that point by this set of planes (often termed "reflection", though this is physically inaccurate as explained below). A convenient way to consistently define these planes is by using Miller indices. In this method, three indices, (h k l), are calculated by taking the reciprocal of the plane interception with the **a**, **b**, and **c** axes of the unit cell, respectively. **Figure 1.7** shows the (100) and (200) Miller planes marked in red. For the **a**-axis, the (100) planes intercept at 1 while the (200) planes intercept at ½, giving rise to the reciprocal values of 1 and 2 given as the first Miller index (h). The displayed planes do not intercept the **b** and **c** axes, therefore these intercept values are assigned as infinite, with the reciprocal being zero. Thus, the second (k) and third (l) Miller indices are zero.

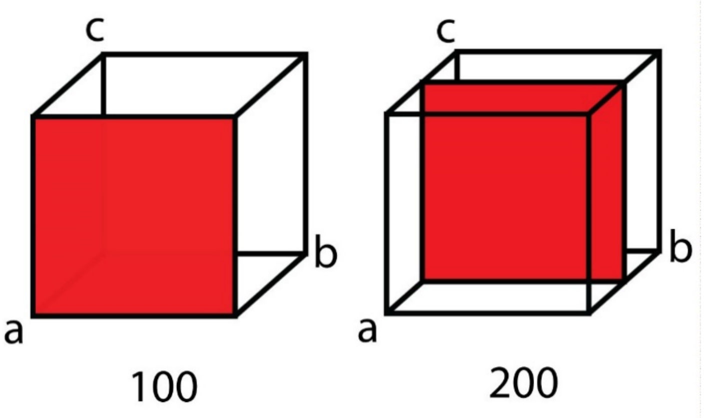

**Figure 1.7** Representations of the (100) and (200) Miller planes.

While useful, the Bragg equation stems from an oversimplified view of diffraction as reflection. In reality, the scattering from every atom contributes to the observed intensity of each reflection. The atomic scattering factor represents the extent of radiation scattered by a single atom. A common mathematical expression of this factor is shown in Eq. 1.3,

$$f = f_0 \exp\left[-\frac{Bsin^2\theta}{\lambda^2}\right] \qquad \textbf{Eq. 1.3}$$

where $f_0$ is the scattering factor at scattering angle 0°, $B$ is a thermal motion factor, $\theta$ is the scattering angle, and λ corresponds to the wavelength of the incident radiation. By virtue of their differing positions, the waves scattered by each atom will have a phase shift. The phase shift for each atom at position *x, y, z* contributing to a certain reflection (*h, k, l*) can be written relative to the origin of the unit cell as follows:

$$\Phi = 2\pi i(hx + ky + lz) \qquad \textbf{Eq. 1.4}$$

The observed diffracted intensity for a particular reflection (h, k, l) is then the vector sum of the scattered waves from all atoms in the unit cell. This vector sum is called the structure factor, $\mathbf{F}_{hkl}$:

$$F_{hkl} = \sum_{j=1}^{m} f_j \exp[2\pi i(hx_j + ky_j + lz_j)]$$ **Eq. 1.5**

Equation 1.5 has the form of a Fourier transform. Indeed, a more accurate way to view X-ray diffraction by crystals is that the diffraction pattern represents the Fourier transform of the electron density in the crystal. Equation 1.5 also implies that if the intensity (amplitude) and phase of each diffracted wave were measured, a simple inverse Fourier transform could change the diffraction pattern into a map of the electron density. There are two problems with this. First, the sum should technically be an infinite sum, but no dataset can be infinite. This invariably results in termination ripples in the electron density map. Second, and more problematically, only the intensity is measured experimentally; there is no way to measure the phase of the diffracted wave. Without the phase, the inverse Fourier transform has little meaning. This is known as the phase problem of crystallography.[34]

The phase problem must be overcome in order to use diffraction data to determine a map of the electron density. To do that, different methods have been developed to assign initial phases. In the Patterson approach, phases are assumed to be zero, and measured intensities alone are used as coefficients in the Fourier synthesis to yield interatomic vectors that can be translated into a structure solution.[35] A different strategy known as direct methods uses subtle relationships between the intensities of related reflections to assign initial phase values and obtain a so-called direct structure solution.[36] In the dual space method, phases are assigned to the measured data (randomly or with Patterson or direct methods), then Fourier transforms are performed iteratively between real and reciprocal space (hence "dual space"). During these iterations, phases in reciprocal (diffraction) space are revised to eliminate physically meaningless negative electron densities in the real space map. Finally, atom identities and connectivity are assigned using already existing chemical information.[37]

### 1.3.2 From single crystal to chemical structure

This section outlines the experimental procedures used to obtain a crystal structure for the organic compounds presented in this dissertation. In general, the process consisted of the following steps: (1) crystal growth and screening, (2) data collection and reduction, (3) structure solution and refinement. Each of these steps will be briefly explained.

#### *1.3.2.1 Crystal growth and screening*

Organic crystals are usually grown by three simple methods: a) slow evaporation, b) slow cooling, and c) vapor diffusion. For slow evaporation, a saturated solution of the compound is prepared, and the solvent evaporated over several days. Large single crystals are ideally formed at the bottom of the solution container. For slow cooling, a solution is prepared at high temperature and slowly cooled down to yield single crystals. Finally, for vapor diffusion, a solvent with low solubility for the compound is slowly diffused into a concentrated solution and single crystals are formed. In the experiments outlined in this dissertation, the slow evaporation method was generally used due to the large and high-quality crystals needed for THz generation.

Once crystals are obtained, they must be evaluated to determine their appropriateness for an X-ray diffraction experiment. Crystals are first screened visually using a microscope to ensure that they have a promising size, shape, and clarity. Sizes should range between 20 to 500 μm. Crystal shapes should be block-like because the stacking of unit cells should result into crystals with sharp edges. Crystals in the right size range should generally be transparent with no visible cracks. Viewing their interaction with polarized light also provides a useful means of determining clarity and whether a crystal comprises a single domain; single crystals will grow dim or change colors uniformly as the direction of polarization is changed.

After crystals have been visually screened and determined to be promising, they are 'harvested' by removing them from their native solvent and placing them in paratone oil on a microscope slide. A promising candidate is selected and, if necessary, cut to a more appropriate size or isotropic shape using a scalpel. The final test of crystal quality is to view its diffraction. The candidate crystal is mounted in a polyimide loop with apertures of 75 and 150 μm for small and large crystals, respectively. It is then centered in the X-ray beam using a video camera. Quick exposures to X-ray radiation revealing a small portion of the diffraction pattern enables the nature of the crystal to be evaluated. **Figure 1.8** shows diffraction patterns for a single crystal, a crystal with multiple domains (often termed "twinned"), and a polycrystalline sample.

Crystal screening with various candidates continues until a single crystal is identified and mounted on the instrument.

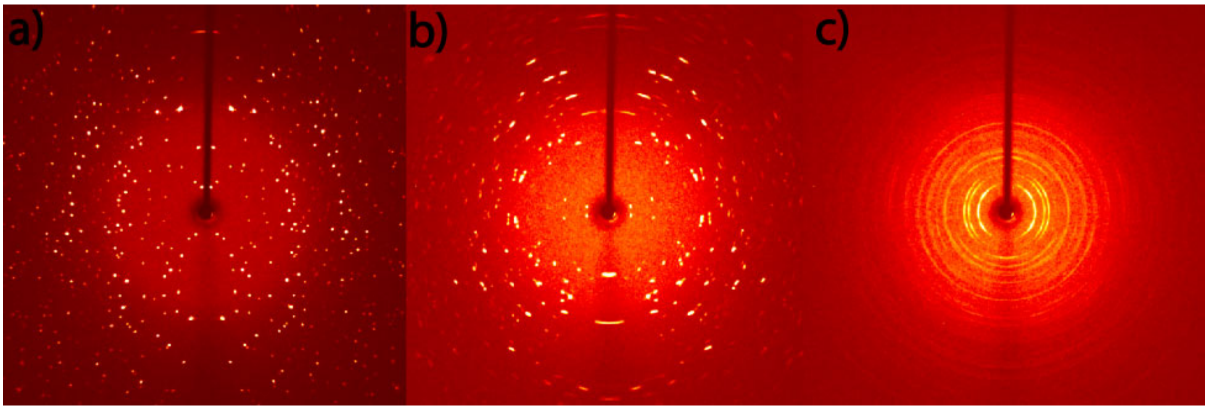

**Figure 1.8** Diffraction pattern for a) single crystal, b) crystal with multiple domains, and c) polycrystalline sample.

The instrument used to collect X-ray diffraction data for this dissertation consisted of a MACH3 kappa goniometer, an FR-591 Bruker-Nonius rotating anode X-ray generator, and a Bruker ApexII CCD detector. The kappa goniometer consists of four axes: three axes control crystal movement (phi, omega, and chi) and one axis allows detector movement (2theta). During typical data collections, the crystal is rotated by 1° along one axis per image (generally either phi or omega). Dozens or hundreds of images are collected per scan, and dozens of scans are collected for most samples (i.e. thousands of images per data collection).

In any X-ray generator, X-rays are produced when electrons accelerated by a voltage potential strike a metal plate (the anode), knocking out core electrons and releasing photons with wavelengths in the order of 0.2 to 2.0 Å as higher energy electrons relax into the resulting holes. To maximize the efficiency of this process, a vacuumed chamber is employed as a protecting envelope. Our FR-591 generator also employed a rotating platform for the metal target to reduce overheating and access higher currents to produce more photons, making a brighter X-ray source. Elements often used as the metal target for X-ray generation in academic research are Cu, Mo, and Ag with characteristic radiation wavelengths of 1.54, 0.71 and 0.56 Å, respectively. In this particular case, Cu was employed as the generating anode.

To detect the diffracted X-rays from a crystalline sample, our instrument employed a Bruker ApexII charged coupled device (CCD). These detectors convert photons to electrons using a phosphor material as intermediate.

#### *1.3.2.2 Data collection and reduction*

Once a single crystal has been identified and mounted on the instrument, it is beneficial to collect a small preliminary subset of data in order to determine the unit cell dimensions and Bravais lattice of the sample. Knowledge of the unit cell enables the locations of all possible reflections to be predicted. Knowledge of the Bravais lattice symmetry provides information about which portion of the diffraction data are unique and should therefore be collected. To determine the unit cell dimensions and probable Bravais lattice symmetry, a small amount of diffraction data is collected (roughly 60 images) via two or three short omega scans. After approximately 100 unique reflections are obtained, the unit cell dimensions of the crystal can be determined along with the orientation of the unit cell on the instrument. With the unit cell dimensions and Bravais lattice symmetry, a data collection strategy is calculated. This strategy coordinates the motion of all four axes such that the intensity of each unique reflection is measured at least once. This is referred to as completeness of the dataset. Additionally, each unique reflection should be measured not just once but several times and then averaged to obtain a more accurate measure of the intensity. This is known as multiplicity of observation, and in general the average multiplicity should be between 4-8.

Because diffraction data must be truncated at some point, the International Union of Crystallography has determined standards for obtaining good quality diffraction data. For small molecules such as the organic molecules in this dissertation, data should extend at least to angles related to d-spacings of 0.84 Å.[38] If diffraction data at these angles is recorded, then the electron density map obtained via the inverse Fourier transform will be able to clearly resolve entities with 0.84 Å spacing. This means that all atoms (including H atoms) will appear as distinct points of electron density. With this resolution, bonds between atoms can be clearly appreciated and a complete structural characterization is possible.

Once the full dataset of unique reflections is collected, the location and intensity of the reflections in each image are recorded in a process known as data reduction. First, each reflection is located and assigned appropriate Miller indices based on the chosen unit cell, and the measured intensity is integrated and recorded along with an estimated standard deviation. This was achieved using the program SAINT.[39] Second, the measured intensities are scaled, or corrected for crystal size and absorption effects. Scaling was performed using the SADABS[40] and TWINABS[41] software for normal and twinned samples, respectively. The Bruker Apex3 software suite employed throughout data collection, processing, and refinement incorporated these (and other) programs.

### *1.3.2.3 Structure solution and refinement.*

All structures were solved using dual-space methods in SHELXT.[37] Because initial structure solutions are based on flawed/imperfect phase assignments, all initial structural models should then also be refined. During refinement, the diffraction pattern of the structural model is calculated and compared with the observed diffraction pattern. Atom identities, positions, ellipsoids, and disorders in the model are then adjusted so that the model's diffraction pattern and the observed diffraction pattern are more closely aligned. This is generally accomplished through a least-squares refinement protocol, wherein the difference between the observed $(F_O^2)$ and calculated $(F_C^2)$ structure factors squared are minimized according to equation 1.6:

$$\Delta = \left|F_O^2 - \mathrm{F}_C^2\right| \qquad \textbf{Eq. 1.6}$$

$$R = \frac{\sum_{hkl}\left||F_O| - |F_c|\right|}{\sum_{hkl}|F_O|} \qquad \textbf{Eq. 1.7}$$

This minimization was accomplished for all structures in this dissertation through a full-matrix least-squares refinement protocol in SHELXL-2014[42] using established refinement strategies.[38]

A widely used parameter to evaluate the quality of a refinement is the R value. This value is calculated using Equation 1.7, where $F_O$ and $F_C$ refer to the same observed and calculated structure factors as in Equation 1.6. For small molecule structures such as those in this dissertation, an R value of less than 5% is typically considered sufficient proof that a given model accurately reflects the true crystal structure.

Once refinement is complete, the ‘crystal structure’ can be viewed and pertinent information gleaned, such as bond distances, bond angles, connectivity, absolute structure, symmetry, and three-dimensional packing. **Figure 1.9** shows the most common method of plotting a crystal structure, which uses an ORTEP plot with 50% probability ellipsoids to plot the asymmetric unit or molecule of interest. The ellipsoids representing each atom are drawn such that they enclose the volume of space corresponding to 50% of that atom’s electron density.

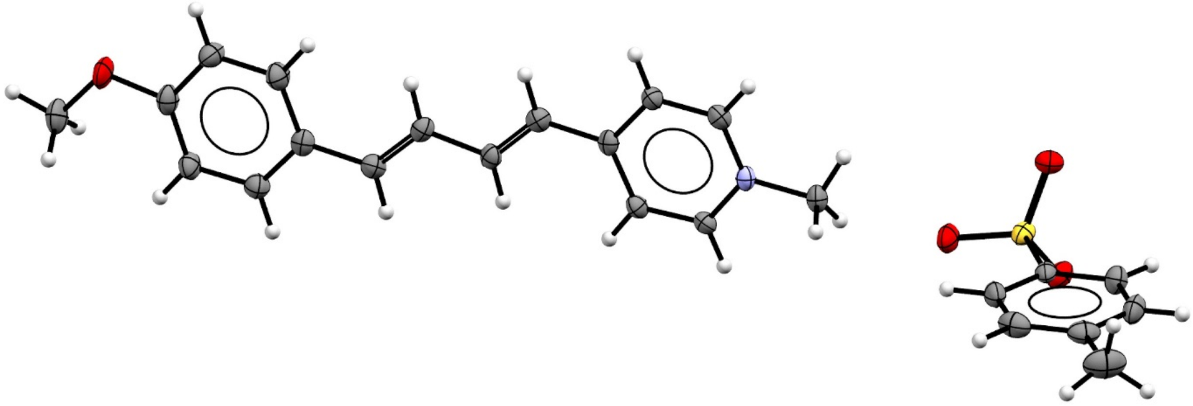

**Figure 1.9** Fully refined organic molecule

## 1.4 THz generation and detection

### 1.4.1 THz generation by optical rectification

Nonlinear optical crystals can produce THz radiation by optical rectification (OR) of ultrafast laser pulses.[43] In this section, a physical and mathematical explanation of this process will be briefly discussed. To understand optical rectification, we must consider the interaction between an applied electric field and the static polarization of any material. If the symmetry of a crystal is low enough to induce internal dipole moment directionality, then the polarization promoted by the applied electric field will not vanish when the field is reversed. This will produce a build-up of net polarization, if the electric field changes sinusoidally. This phenomenon is illustrated in **Figure 1.10**, where an applied electric field (shown in black) is directed to a non-centro (top) and a centrosymmetric crystal (bottom). An increasing polarization is generated in the non-centrosymmetric crystal, compared with zero net polarization for the centrosymmetric counterpart.

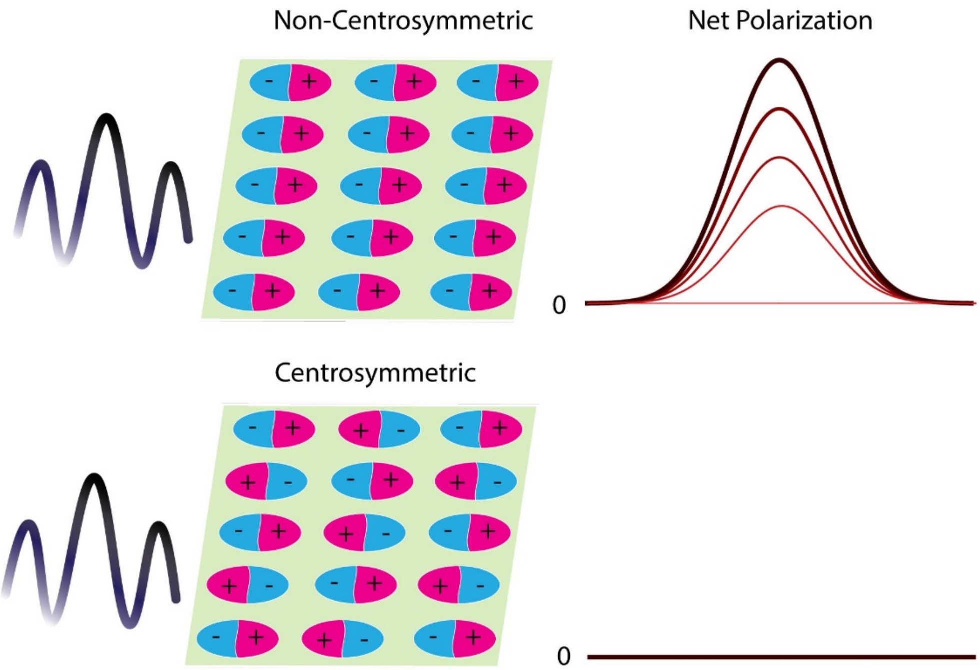

**Figure 1.10** Net polarization build up in non-centrosymmetric materials

A mathematical picture of optical rectification can be formed using the dielectric polarization density equation:

$$P(t) = \varepsilon_0\left(\chi^{(1)}E(t) + \chi^{(2)}E^2(t) + \chi^{(3)}E^3(t) + \ldots\right) \qquad \textbf{Eq. 1.8}$$

where $\varepsilon_0$ represents the vacuum permittivity, $\chi$ the electric susceptibility and *E*(*t*) the electric field. If we assume that *E*(*t*) is formed by two frequency components and considering the oscillating form of *E*(*t*), we have:

$$E(t) = \frac{1}{2}E_1 e^{-i\omega_1 t} + \frac{1}{2}E_2 e^{-i\omega_2 t} \qquad \textbf{Eq. 1.9}$$

where the $\omega$ terms represent the frequency of the electric field. Typical crystalline fields are larger compared to the electric field strengths produced with optical lasers. Therefore, an expansion of the polarization depending on nonlinear terms is appropriate. The quadratic term in equation 1.8 is the lowest that can represent a nonlinear contribution to the total polarization. This term is also known as the second-order nonlinear polarizability $P^{NL}$.

$$P^{NL} = \varepsilon_0 \chi^{(2)} E^2(t) \qquad \textbf{Eq. 1.10}$$

The $\chi^{(2)}$ term in equation 1.10 is different from 0 only in non-centrosymmetric crystals. Therefore, considering up to second order, the $P^{NL}$ will have a non-zero value only in non-centrosymmetric materials. Combining equations 1.9 and 1.10, the following expression is obtained:

$$P^{NL} = \frac{\varepsilon_0}{4}\chi^{(2)}\left[{E_1}^2 e^{-i2\omega_1 t} + {E_2}^2 e^{-i2\omega_2 t} + 2E_1E_2e^{-i(\omega_1+\omega_2)t} + 2E_1E_2e^{-i(\omega_1-\omega_2)t} + |E_1|^2 + |E_2|^2\right] \qquad \textbf{Eq. 1.11}$$

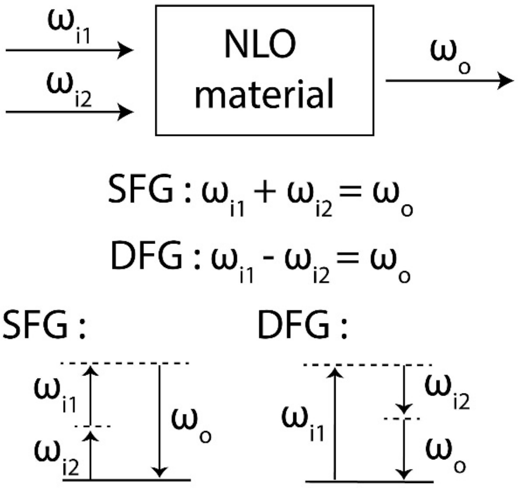

**Figure 1.11** Sum (SFG) and Difference (DFG) Frequency generation in a nonlinear optical material (top). Virtual levels for SFG and DFG processes (bottom).

Analyzing equation 1.11, oscillating sum and difference frequency terms are observed. These terms are responsible due to the interaction between frequencies in nonlinear materials, that are responsible for creating new frequencies. As shown in **Figure 1.11**, the sum-frequency term, $e^{-i(\omega_1+\omega_2)t}$, is related to sum-frequency generation (SFG)[44] where two incoming photons of light are combined in the NLO crystal to produce a third photon with a frequency corresponding to the sum of them. The difference term, $e^{-i(\omega_1-\omega_2)t}$, is utilized in difference-frequency generation (DFG),[45] where two photons with different energies are combined to produce a third photon with a frequency corresponding to the difference between the two incoming photons. In order to obtain SFG or DFG responses, two sources of radiation are normally needed. However, if the spectral bandwidth of an ultrafast laser pulse is broad enough to enable subtraction between its frequency components, then output frequencies with much lower energy compared to the input pulse can be obtained. This interaction is the foundation of OR and it has been exploited to obtain THz radiation from infrared (IR) light.

### 1.4.2 Parameters that affect optical rectification

Optical, crystal and laser parameters affect the THz output of optical rectification. Here, the most important considerations for organic crystals and near-infrared ultrafast laser sources will be analyzed.

#### *1.4.2.1 Phase matching*

When two frequencies interact in the same material, they need to be in phase with each other in order to obtain constructive interference. However, for THz and IR light, the refractive indices may be very different within the THz generating crystal. This produces a phase mismatch that will lead to destructive interference that suppresses the THz output.[46] As shown in **Figure 1.12**, the length of the crystal sample where the phase matching is acceptable is called the coherence length ($l_c$). Equation 1.12 shows that the THz refractive index ($n_T$) and optical pump group index ($n_g$) should be close to each other in order to obtain a large value of $l_c$.[24] As the difference term in the denominator gets larger, $l_c$ will be smaller and therefore thinner crystals will be needed to avoid phase mismatch. A small $l_c$ value will also reduce the THz output due to fewer molecular dipoles contributing to the generation process.

$$l_c(\omega,\lambda) = \frac{\pi c}{\omega\left|n_T(\omega) - n_g(\lambda)\right|}$$ **Eq. 1.12**

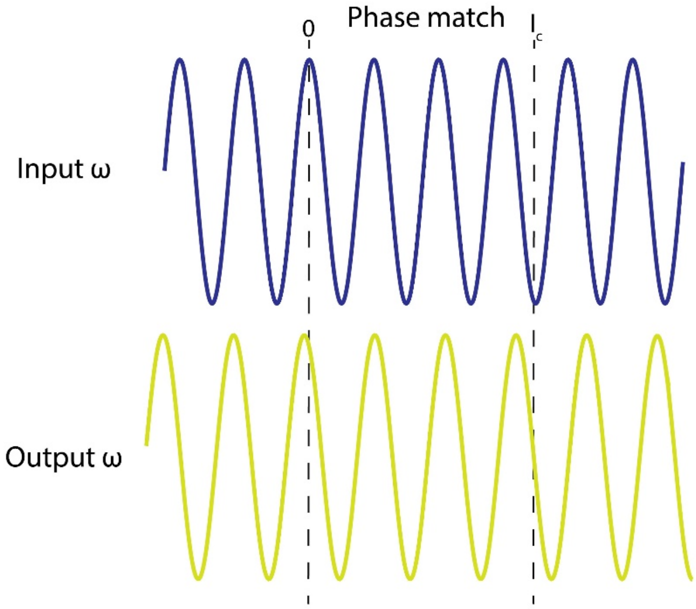

**Figure 1.12** Phase matching in the coherence length ($l_c$) of a crystal

Using the coherence length values ($l_c(\omega,\lambda)$), the THz generation length can be calculated according to equation 1.13:[24]

$$l_{gen}(\omega,\lambda,l) = \left(\frac{\exp(-2\alpha_0(\lambda)l)+\exp(-\alpha_T(\omega)l)-2\exp\left(-\left[\alpha_0(\lambda)+\frac{\alpha_T(\omega)}{2}\right]l\right)cos\left(\frac{\pi l}{l_c(\omega,\lambda)}\right)}{\left(\frac{\alpha_T(\omega)}{2}-\alpha_0(\lambda)\right)^2+\left(\frac{\pi}{l_c(\omega,\lambda)}\right)^2}\right)^{\mathbf{1/2}} \qquad \textbf{Eq. 1.13}$$

where $\alpha_0$ and $\alpha_T$ are the absorption coefficients of the generating crystal at IR pumping wavelengths and THz generating generated frequencies, respectively. Additionally, the $l$ parameter refers to the thickness of the crystal. With the generation length, it is then possible to obtain a simulated generation spectrum using equation 1.14:[24]

$$|E_{THz}(\omega)| = \left|\frac{\mu_0\chi^{(2)}(\omega,\lambda)\omega I(\omega)}{n_0(\lambda)\left[\frac{c}{\omega}\left(\frac{\alpha_T(\omega)}{2}+\alpha_0(\lambda)\right)+i\left(n_T(\omega)+n_g(\lambda)\right)\right]}\right| l_{gen}(\omega,\lambda,l) \qquad \textbf{Eq. 1.14}$$

where $\mu_0$ is the vacuum permittivity, $\chi^{(2)}$ is the scond order nonlinear susceptibility, $I(\omega)$ is the Fourier transform of the IR pumping laser intensity. $n_0(\lambda)$ and $n_T(\omega)$ are the refractive indices of the crystal in the IR and THz frequencies, respectively. The $n_g(\lambda)$ parameter refers to the group index in the IR region. The $\alpha_T(\omega)$ and $\alpha_0(\lambda)$ terms are the same as in equation 1.13.

### *1.4.2.2 Radiation absorption*

An important consideration in THz generation by optical rectification is the extent of absorption of the input and output radiations by the generating crystal. Several organic crystals have been reported with low absorption of near-infrared light typically employed in THz generation experiments (800 to 1600 nm). For instance, HMQ-TMS features about 80% transmission from 450 to 2000 nm.[47] However, two-photon absorption becomes important when the power of the incoming NIR light is increased. This phenomenon takes place when two photons of the same energy are combined to produce a new photon with two times the energy and half the wavelength. Therefore, if a generating crystal strongly absorbs radiation at 400 nm and it is pumped with 800 nm light, then the THz generation output will be reduced and the crystal will be damaged over time.

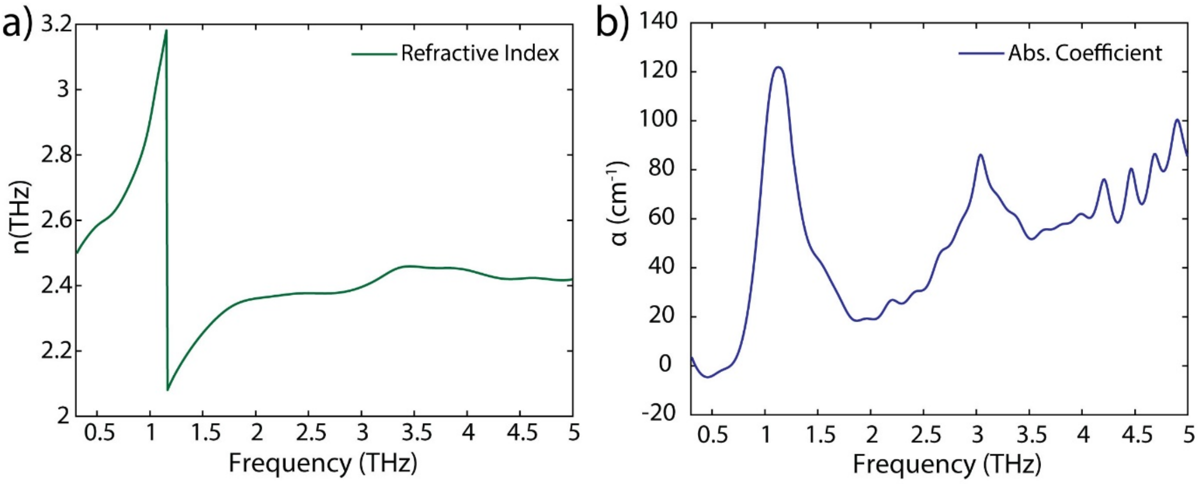

**Figure 1.13** a) Refractive index and b) absorption coefficient for DAST.

Another factor to consider is the absorption of THz radiation by the generating molecular crystal. This a common effect due to vibrations in organic molecules that show resonance in the THz region. **Figure 1.13** shows the refractive index and absorption coefficient of a DAST crystal, where a strong phonon mode absorption is appreciated at ~1.1 THz. Other crystals such as HMQ-TMS and OH1 show similar phonon mode absorptions at 1.6 and 3 THz.[43, 48]

### *1.4.2.3 Pulse duration*

The pulse duration of the pumping femtosecond laser pulse determines the bandwidth of the generated THz spectrum. **Figure 1.14a** shows THz generation traces for a perfectly matched crystal at 50, 100 and 150 fs laser pulse durations. Narrower spectra along with central frequencies shifted to lower frequencies are observed for longer pulse durations. This same effect is illustrated in the THz generation spectrum of DAST, as shown in **Figure 1.14b.**

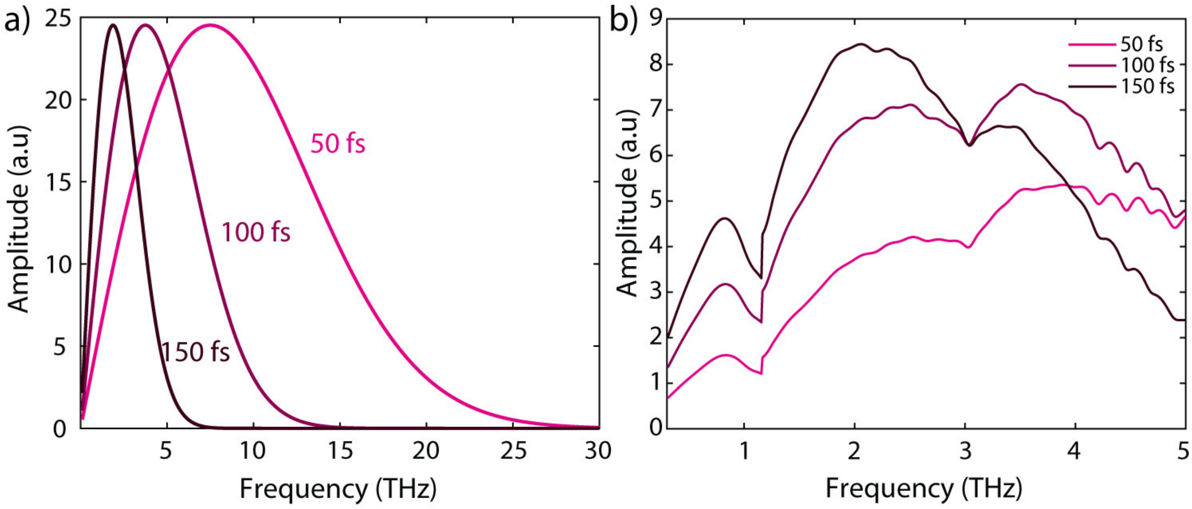

**Figure 1.14** THz generated spectra for a) perfectly matched crystal and b) DAST crystal at 50, 100, 150 fs pulse durations.

**Figure 1.15c** shows THz generation simulated spectra for the organic crystal DAST obtained using equations 1.12 to 1.14 and the refractive index and absorption in the THz regions shown in **Figure 1.13. Figure 1.15a** shows the calculated coherence length for the organic crystal DAST. The coherence length shows similar values from 1.1 to 5 THz where most of the spectral content is obtained, as seen in **Figure 1.15c**. The generation length displayed in **Figure 1.15b** essentially shows what thickness of 100, 150 and 200 μm DAST crystals contributes to THz generation. Using the coherence and generation length, a complete generation spectrum can be modeled (shown in **Figure 1.15c**). All crystal thicknesses produce spectra without much frequency content at 1.1 THz due to an internal absorption in DAST. The spectrum modeled based on a 100 μm DAST crystal offers the broadest spectrum with spectral amplitude extending up to 5 THz.

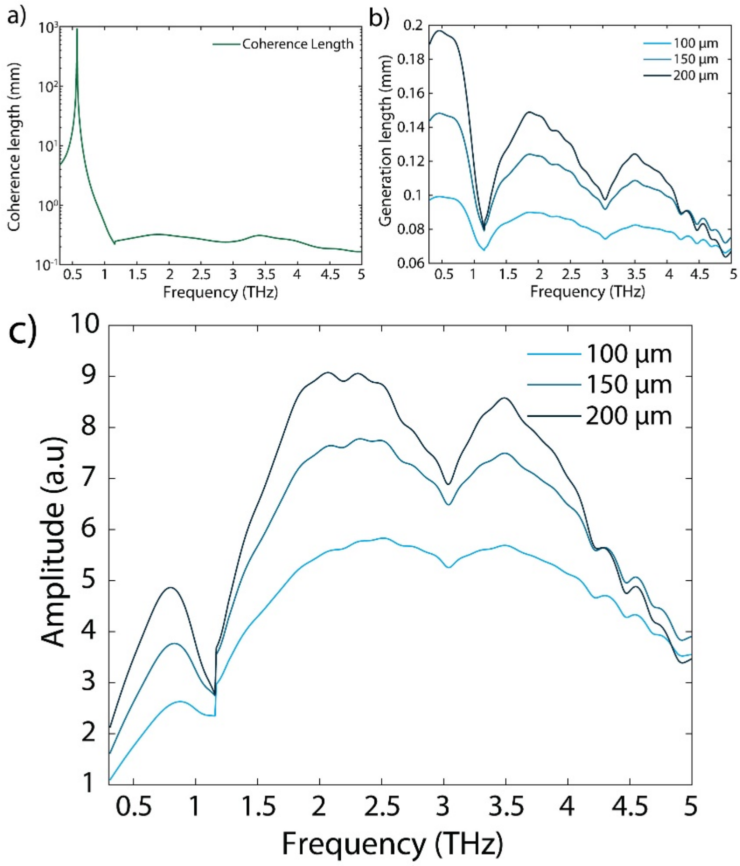

**Figure 1.15** a) Coherence length, b) generation length, and c) simulated THz generation spectrum for DAST.

### 1.4.3 Electro-optic sampling detection and THz generation setup

Once THz frequencies are generated, the produced electric field can be measured using techniques such as down mixing, photoconductive detection and electro-optical sampling. Due to its wide applicability, electro-optical sampling (EOS) will be exclusively addressed in this section. In this technique, the same NLO crystals used for THz generation by OR could also be employed for THz detection purposes by relying on the Pockels effect. The Pockels or electro-optic effect is produced when a crystalline material becomes birefringent in the presence of an external electric field (in this case, the THz electric field). By tracking the change in polarization of an ultrafast probe pulse (as a function of relative THz-probe delay), we can map out the THz electric-field waveform in time. This measurement of probe-polarization rotation is accomplished using the combination of a λ/4 wave plate oriented at 45 degrees, a Wollaston polarizer that splits vertical and horizontal probe polarization components, which are measured with balanced photodiodes. The difference signal between the two photodiodes is proportional to the THz electric field.

To better visualize OR THz generation and EOS detection, a typical THz generation setup is depicted in Figure 1.16. Infrared laser pulses (represented in blue) are directed towards a THz generating crystal and the resulting THz light (shown in green) is directed to a parabolic mirror, and then focused to a Gallium Phosphide (GaP) electro-optic detection crystal. A Teflon filter is placed behind the generating crystal to filter any residual IR and visible light. As mentioned above, an 800-nm probe pulse (displayed in orange) is utilized to record the THz electric field in the GaP crystal using the EOS method.

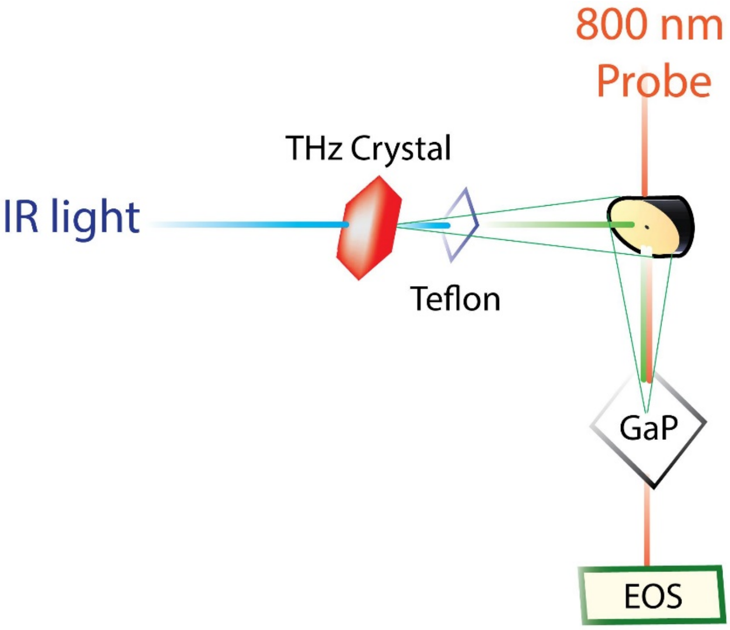

**Figure 1.16** Simplified THz generation setup using optical rectification as THz generation method and electro-optic sampling as detection technique.

## 1.5 Summary

Organic molecules for THz generation are designed using a push-pull approach to increase the molecular hyperpolarizability. This parameter can be obtained using DFT calculations and then several compounds can be ranked to synthesize the most promising ones. Synthesis methods usually involve carbon-carbon double bond formations, and therefore condensation reactions are employed. After synthesis, the required non-centrosymmetric molecular packing in the crystalline state is assessed with X-ray diffraction. Non-centrosymmetric crystals with good to optimal molecular ordering are tested for THz generation using Optical Rectification of ultrafast infrared laser pulses. Important optical parameters such as coherence length, THz absorption and refractive indices are also evaluated to fully characterize novel THz generating crystals.

In section 1.2 we reviewed the push-pull design approach and the most common synthetic pathways to obtain organic molecules with high hyperpolarizability. In section 1.3, the basic principles of single crystal X-ray diffraction were analyzed focused on organic molecules. Additionally, we outlined a typical procedure to obtain a fully refined crystal structure starting from small single crystals. In section 1.4, the foundation principles of THz generation by optical rectification were summarized. The parameters affecting the THz output from organic crystals were exemplified using the state-of-the-art DAST crystal.

## 1.6 References

[1] M. Tonouchi, *Nature photonics* **2007**, 1, 97.
[2] X. C. Zhang, A. Shkurinov, Y. Zhang, *Nature Photonics* **2017**, 11, 16.
[3] K. W. Kim, H. Kim, J. Park, J. K. Han, J.-H. Son, *IEEE Transactions on Terahertz Science and Technology* **2012**, 2, 99.
[4] K. Ajito, J.-Y. Kim, Y. Ueno, H.-J. Song, K. Ueda, W. Limwikrant, K. Yamamoto, K. Moribe, *Journal of The Electrochemical Society* **2014**, 161, B171.
[5] A. Dobroiu, Y. Sasaki, T. Shibuya, C. Otani, K. Kawase, *Proceedings of the IEEE* **2007**, 95, 1566.
[6] Z. Zheng, C. Zhao, S. Lu, Y. Chen, Y. Li, H. Zhang, S. Wen, *Optics Express* **2012**, 20, 23201.
[7] J. Qin, Y. Ying, L. Xie, *Applied Spectroscopy Reviews* **2013**, 48, 439.
[8] H. Tong, S. Pei, L. Jiang, Y. Zhu, X. Lin, 2016.
[9] P. Tewari, N. Bajwa, R. S. Singh, M. O. Culjat, W. S. Grundgest, Z. D. Taylor, C. P. Kealey, D. B. Bennett, K. S. Barnett, A. Stojadinovic, *Journal of biomedical optics* **2012**, 17, 040503.
[10] S. J. Oh, Y.-M. Huh, J.-S. Suh, J. Choi, S. Haam, J.-H. Son, *Journal of Infrared, Millimeter, and Terahertz Waves* **2012**, 33, 74.
[11] B. Born, S. J. Kim, S. Ebbinghaus, M. Gruebele, M. Havenith, *Faraday discussions* **2009**, 141, 161.
[12] B. M. Fischer, M. Walther, P. U. Jepsen, *Physics in Medicine & Biology* **2002**, 47, 3807.
[13] S. Yamauchi, *American Journal of Analytical Chemistry* **2013**, 4, 756.
[14] X. C. Li, J. M. Zhao, L. H. Liu, J. Y. Tan, *Applied Optics* **2015**, 54, 3886.
[15] J.-s. Li, X.-j. Li, *Chemical Physics Letters* **2009**, 476, 92.
[16] S. Matsuura, M. Tani, K. Sakai, *Applied Physics Letters* **1997**, 70, 559.
[17] X. Xie, J. Xu, J. Dai, X. C. Zhang, *Applied physics letters* **2007**, 90, 141104.
[18] M. C. Hoffmann, K.-L. Yeh, J. Hebling, K. A. Nelson, *Optics express* **2007**, 15, 11706.
[19] M. Shalaby, C. P. Hauri, *Nature Communications* **2015**, 6, 5976.
[20] J. Zyss, J. L. Oudar, *Physical Review A* **1982**, 26, 2028.
[21] H. Chen, Q. Ma, Y. Zhou, Z. Yang, M. Jazbinsek, Y. Bian, N. Ye, D. Wang, H. Cao, W. He, *Crystal Growth & Design* **2015**, 15, 5560.

[22] S. H. Lee, J. Lu, S. J. Lee, J. H. Han, C. U. Jeong, S. C. Lee, X. Li, M. Jazbinšek, W. Yoon, H. Yun, B. J. Kang, F. Rotermund, K. A. Nelson, O. P. Kwon, *Advanced Materials* **2017**, 29, 1701748; G. A. Valdivia-Berroeta, E. W. Jackson, K. C. Kenney, A. X. Wayment, I. C. Tangen, C. B. Bahr, S. J. Smith, D. J. Michaelis, J. A. Johnson, *Advanced Functional Materials* **2019**, 1904786; Z. Yang, S. Aravazhi, A. Schneider, P. Seiler, M. Jazbinsek, P. Günter, *Advanced Functional Materials* **2005**, 15, 1072.

[23] F. Pan, M. S. Wong, C. Bosshard, P. Günter, *Advanced Materials* **1996**, 8, 592.

[24] F. D. J. Brunner, O. P. Kwon, S.-J. Kwon, M. Jazbinšek, A. Schneider, P. Günter, *Optics express* **2008**, 16, 16496.

[25] J. Lu, H. Y. Hwang, X. Li, S.-H. Lee, O. P. Kwon, K. A. Nelson, *Optics express* **2015**, 23, 22723.

[26] M. Shalaby, C. Vicario, K. Thirupugalmani, S. Brahadeeswaran, C. P. Hauri, *Optics letters* **2016**, 41, 1777.

[27] H. Umezawa, K. Tsuji, S. Okada, H. Oikawa, H. Matsuda, H. Nakanishi, *Optical Materials* **2003**, 21, 75.

[28] T. Kobkeatthawin, T. Suwunwong, S. Chantrapromma, H. K. Fun, *Acta Crystallographica Section E: Structure Reports Online* **2009**, 65, o76.

[29] S.-H. Lee, M. Jazbinsek, C. P. Hauri, O. P. Kwon, *CrystEngComm* **2016**, 18, 7180.

[30] S.-J. Kwon, O. P. Kwon, J.-I. Seo, M. Jazbinsek, L. Mutter, V. Gramlich, Y.-S. Lee, H. Yun, P. Günter, *The Journal of Physical Chemistry C* **2008**, 112, 7846.

[31] M. J. Frisch, G. W. Trucks, H. B. Schlegel, G. E. Scuseria, M. A. Robb, J. R. Cheeseman, G. Scalmani, V. Barone, G. A. Petersson, H. Nakatsuji, *Gaussian Inc., Wallingford, CT* **2016**.

[32] B. Ruiz, Z. Yang, V. Gramlich, M. Jazbinsek, P. Günter, *Journal of Materials Chemistry* **2006**, 16, 2839.

[33] W. H. Bragg, W. L. Bragg, *Proceedings of the Royal Society of London. Series A, Containing Papers of a Mathematical and Physical Character* **1913**, 88, 428.

[34] R. W. Harrison, *JOSA a* **1993**, 10, 1046.

[35] A. L. Patterson, *Zeitschrift für Kristallographie-Crystalline Materials* **1935**, 90, 517.

[36] M. M. Woolfson, *Reports on Progress in Physics* **1971**, 34, 369.

[37] G. M. Sheldrick, *Acta Crystallographica Section A: Foundations and Advances* **2015**, 71, 3.

[38] P. Müller, *Crystallography Reviews* **2009**, 15, 57.

[39] G. M. Sheldrick, *Siemens Area Detector Integration. Siemens Analytical X-ray Instruments Inc., Madison, Wisconsin, USA* **1995**.

[40] G. M. Sheldrick, **1996**.

[41] G. M. Sheldrick, *University of Göttingen, Germany* **2009**, 20.

[42] G. M. Sheldrick, *Acta Crystallographica Section C: Structural Chemistry* **2015**, 71, 3.

[43] F. D. J. Brunner, S.-H. Lee, O. P. Kwon, T. Feurer, *Optical Materials Express* **2014**, 4, 1586.

[44] P. Günter, *Nonlinear optical effects and materials*, Springer, **2012**.

[45] K. Miyamoto, S. Ohno, M. Fujiwara, H. Minamide, H. Hashimoto, H. Ito, *Optics express* **2009**, 17, 14832.

[46] A. N. Bugay, S. V. Sazonov, *Bulletin of the Russian Academy of Sciences: Physics* **2016**, 80, 774.

[47] J.-H. Jeong, B.-J. Kang, J.-S. Kim, M. Jazbinsek, S.-H. Lee, S.-C. Lee, I.-H. Baek, H. Yun, J. Kim, Y. S. Lee, J.-H. Lee, J.-H. Kim, F. Rotermund, O.-P. Kwon, *Scientific reports* **2013**, 3.

[48] X. Zhang, X. Jiang, Y. Li, Z. Lin, G. Zhang, Y. Wu, *CrystEngComm* **2015**, 17, 1050.

[49] S. W. Huang, J. Yang, J. Lim, H. Zhou, M. Yu, D. L. Kwong, C. W. Wong, *Scientific reports* **2015**, 5, 13355.

[50] E. Castro-Camus, J. Lloyd-Hughes, M. B. Johnston, M. D. Fraser, H. H. Tan, C. Jagadish, *Applied Physics Letters* **2005**, 86, 254102.

[51] Q. Wu, X. C. Zhang, *Applied Physics Letters* **1995**, 67, 3523.

[52] A. Kumada, K. Hidaka, *IEEE transactions on power delivery* **2013**, 28, 1306.

# Chapter 2 Alkynyl Pyridinium Crystals for Terahertz Generation

## 2.1 Overview

To increase the molecular hyperpolarizability of the state-of-the-art DAST crystal, the bridging double bond was substituted by a triple bond to originate the molecular cation 4DEP. To obtain the molecular packing needed for large nonlinear optical susceptibility and efficient THz generation, we tested three anions that result in non-centrosymmetric crystals: 4-methylbenzenesulfonate (T), 3-nitrobenzenesulfonate (3NBS), and napthalene-2-sulfonate (N2S). After synthesis and crystallization, we characterized the crystal structure via XRD analysis and predicted the relative THz generation efficiency for ideal crystals. 4DEP-N2S shows a roughly 30% larger relative second-order nonlinear optical susceptibility compared to HMQ-TMS and DAST and, therefore, shows promise as a new advanced THz generation crystal. However, it was difficult to grow large, high-quality crystals, which may limit the applicability of this new cation for high-field THz generation. The following work was published in Advanced Optical Materials, 6(21), 1800383.

## 2.2 Introduction

Terahertz (THz) radiation lies on the electromagnetic spectrum between microwave and infrared light. With only two decades of use, THz spectroscopy is a fast growing field of study and has a host of applications including medical and material imaging,[1] drug and food analysis,[2] material detection,[3] as well as linear and nonlinear spectroscopy of materials.[4] THz generation via optical rectification[5] is performed using an ultrafast laser pulse in a nonlinear optical crystal. Common nonlinear crystals used for either THz generation or electro-optic detection include inorganic crystals such as ZnTe,[6] GaP,[7] and LiNbO3.[8] However, complicated experimental setups and low THz conversion efficiencies limit the usefulness of inorganic crystals. Developments utilizing organic crystals for optical rectification allow relatively simple setups, high electric-field strengths[9] (up to GV m-1), and ultra-broad THz spectra (up to 200 THz).[10] Organic crystals currently being used include DAST ((4-(4-

(dimethylamino)styryl)-1-methylpyridinium 4-methylbenzenesulfonate)),[11] DSTMS (4-N,N-dimethylamino-4′-N′-methyl-stilbazolium 2,4,6-trimethylbenzenesulfonate),[12] OH1 (2-(3-(4-hydroxystyryl)-5,5-dimethylcyclohex-2-enylidene)malononitrile),[13] and HMQ-TMS ((2-(4-hydroxy-3-methoxystyryl)-1-methylquinolinium 2,4,6-trimethylbenzenesulfonate)).[14]

Each of the above organic THz generation crystals utilize conjugated organic molecules in which electron donating and accepting groups are separated by a series of π-bonds. The strength and positions of the electron donating and withdrawing groups, as well as the length and planarity of the π-system influence the molecular hyperpolarizability, β. Electron donor-π-acceptor compounds have been widely used in organic nonlinear crystals.[15, 16] Two particularly common THz generation crystals, DAST and HMQ-TMS, provide a series of comparisons which prove instructive in designing new THz generation crystals. The DAS cation (in DAST) shown in **Figure 2.1a**, uses a dimethylamino (-N(Me2)) group at the para position and an alkenyl bridge connects to a pyridinium group at the 4-position. The HMQ cation (in HMQ-TMS) shown in **Figure 2.1b**, utilizes hydroxy (-OH) and methoxy (-OMe) electron donating groups at the meta and para positions. An alkenyl bridge connects these to a quinolinium accepting group at the 2-position. The increased separation between donor and acceptor groups in DAS vs HMQ leads to a larger β in DAS.[17] Even though atomic arrangements in the crystalline material are paramount for THz generation, gas-phase calculations of potential THz generators can provide guidance for optimizing the molecular β prior to any time consuming synthetic efforts. Gas phase ab initio geometry optimization conducted in our laboratory (see Section 2, 3) shows that DAS is significantly more planar than HMQ (see **Figure 2.1**); HMQ has an inter-ring torsion angle of 27° whereas DAS is practically flat. A simple calculation shows that β increases by 9 percent when HMQ is forced into a planar geometry. The optimal planar structure and functional groups lead DAS to have a marginally higher β, with a βtotal of $157\times10^{-30}$ esu compared to $143\times10^{-30}$ esu for HMQ.

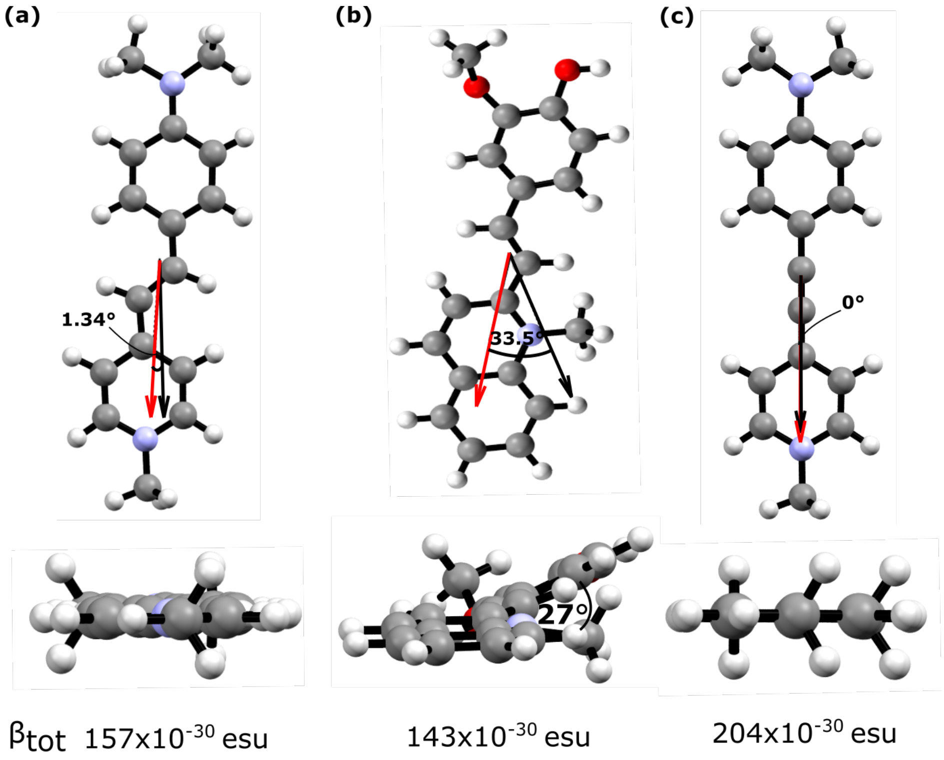

**Figure 2.1** Hyperpolarizability (red) and dipole moment (black) and torsion angles between aromatic rings (bottom) for a) DAS, b) HMQ and c) 4DEP cations.

Gas phase hyperpolarizability calculations give useful guidance because the macroscopic nonlinear susceptibility, $\chi(2)$, is proportional to β, but $\chi(2)$ is also highly dependent on crystal structure. For the m and 2 symmetry point groups common to many organic THz generation crystals,[15] the 1D chromophore approximation proposes that $\chi(2) = \mathrm{N\ Fijk}\ \beta \cos3(\theta\mathrm{p})$,[18] where N is the number density of unit cells, Fijk is the local field factor, and θp is the angle between the main molecular charge-transfer axis and the polar axis of the crystal. Optimal chromophore orientation in the crystal is generally expressed via the order parameter, $\cos3(\theta\mathrm{p})$,[18] which is a measure of the alignment of the vector representation of β with respect to the crystal axes. An order parameter of 1 indicates the optimal combination of molecular βx, βy, and βz. As stated above, DAST has a superior molecular β, but the HMQ-TMS crystal packs optimally resulting in an order parameter of 1.0,[14] compared to the DAST order parameter of only 0.83,[19] resulting in the two crystals having a similar overall $\chi^{(2)}$.

In designing new THz generation crystals, we attempted to combine the best attributes of both HMQ-TMS and DAST. In this report, we outline gas-phase DFT calculations to identify structures with optimal geometry and β (Section 2). An alkynyl bridge generally reduces torsion and increases electron density, both of which act to increase β.[20, 21] Based on these observations, we identified the 4-((4-(dimethylamino)phenyl)ethynyl)-1-methylpyridin-1-ium (4DEP) cation (shown in **Figure 2.1c**) which has a larger calculated β than DAS and HMQ cations. In the present article, we discuss the synthesis of the 4DEP cation and combine the cation with different anions to optimize molecular packing. We provide quantitative predictions for comparing the novel THz crystals to each other, HMQ-TMS, and DAST. Additionally, we report characterization of the crystals for THz generation.

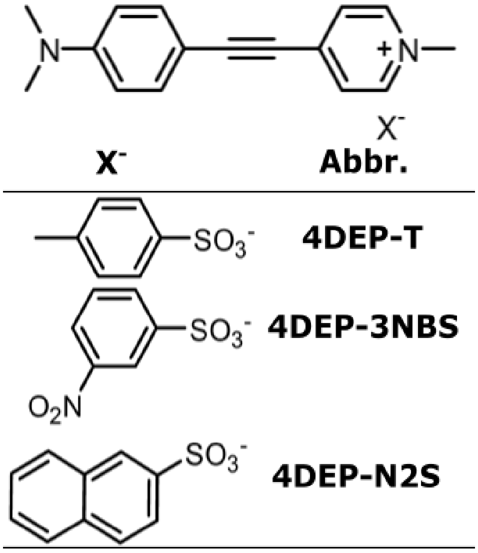

**Figure 2.2** Molecular structures of the potential THz emitters.

## 2.3 Results and Discussion.

### 2.3.1 Molecular design, synthesis and X-ray crystal structures analysis.

As a starting point to screen potential cations relative to the DAS and HMQ cations, we calculated the hyperpolarizability of several cations in a gas phase optimized geometry and identified the 4DEP cation as a promising candidate structure. 4DEP has an optimal planar geometry and a hyperpolarizability of 204×10-30 esu, which is 30% and 43% larger than the DAS and HMQ gas phase cations, respectively (see **Table 2.2**).

The 4DEP cation precursor was synthesized using the Sonogashira cross coupling reaction, paired with three different anions, namely T, 3NBS, and N2S (see **Figure 2.2** and Supporting Information), and then crystallized by slow evaporation in methanol. The N2S and 3NBS anions reduced the ease of crystal growth relative the T anion, however 4DEP-N2S and 4DEP-3NBS crystals could be grown in water-containing methanol, which is advantageous compared to dry methanol growing technique needed for 4DEP-T, due to the potential formation of a centric hydrated polymorphism.[20]

In order to calculate the expected magnitude of the macroscopic nonlinear optical susceptibility, the molecular conformations of 4DEP-T, 4DEP-3NBS and 4DEP-N2S were obtained from X-ray diffraction experiments (see **Table 2.4** for details on X-ray analysis). The crystal structures are shown in **Figures 2.3-2.5** below. The dominant intermolecular interactions for 4DEP-T, 4DEP-3NBS, and 4DEP-N2S are Coulombic forces between the 4DEP cations and sulfonate anions. Furthermore, weak hydrogen bonds between CH aromatic groups from the cation and sulfonyl oxygens in the anion are observed with C---O distances of 3.31 Å for 4DEP-T (**Figure 2.3a**) and 4DEP-3NBS (**Figure 2.4a**) and 3.12 Å for 4DEP-N2S (**Figure 2.5a**).

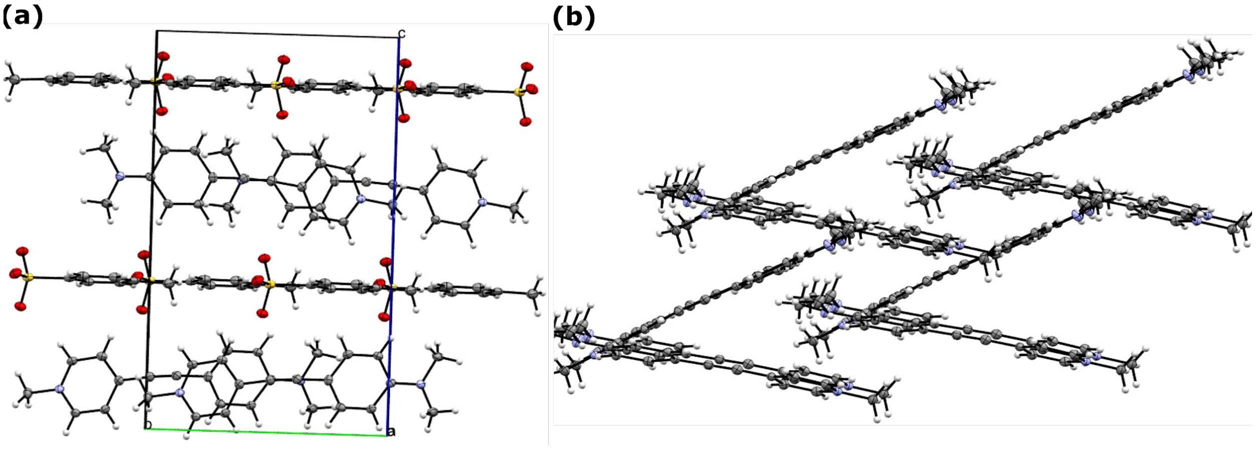

**Figure 2.3** Molecular conformation and crystal packing for 4DEP-T. a) View from b-c plane, showing the anion and cation layers. b) View from a-b plane, displaying the angle between cations.

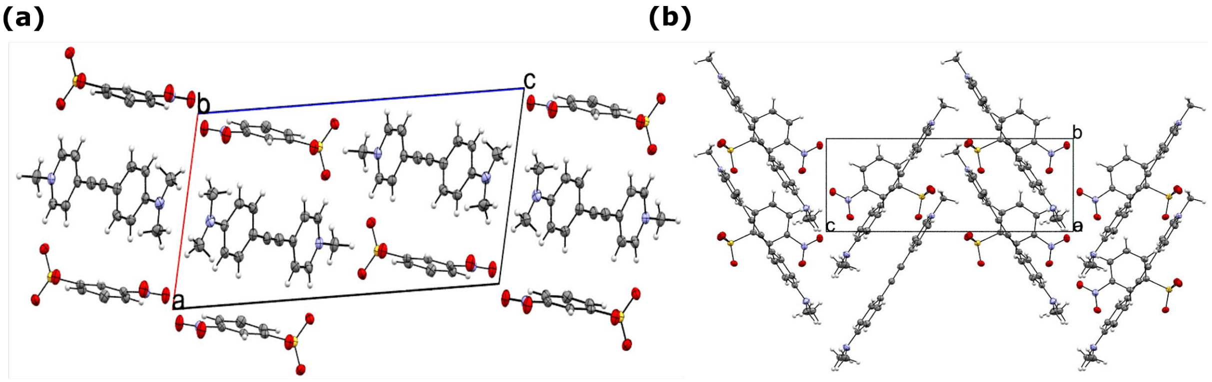

**Figure 2.4** Molecular conformation and crystal packing for 4DEP-3NBS. a) View from a-c plane showing the intercalated anion and cation layers. b) Angle between cation molecules.

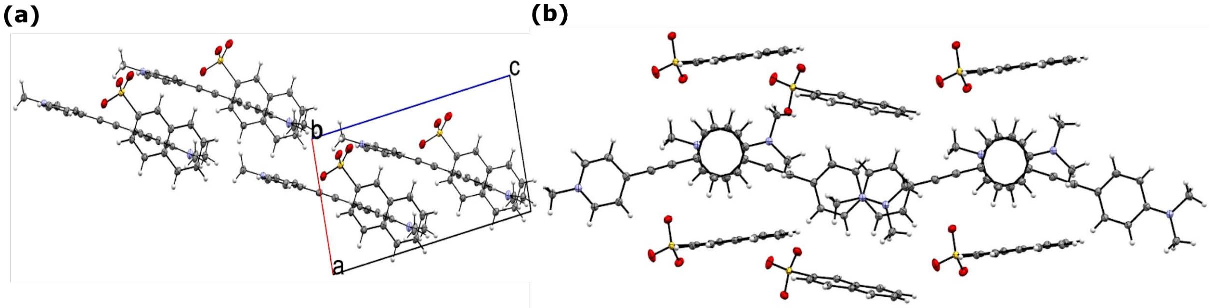

**Figure 2.5** Molecular conformation and crystal packing for 4DEP-N2S. a) Perpendicular arrangement between anions and cation molecules and b) view from a-c plane showing the angle between cation molecules

We expect 4DEP-N2S to be the most promising compound for THz generation based upon the head-to-tail cation conformation observed in the crystal arrangement (**Figure 2.5b**), but a more quantitative comparison can be made utilizing the order parameter ($\cos^3(\theta_p)$) together with computed hyperpolarizabilities. The calculated $\theta_p$ angles for the different molecules studied are shown in **Figure 2.6.** Using this information, the values for the order parameters are 0.03, 0.59 and 0.91 for 4DEP-T, 4DEP-3NBS and 4DEP-N2S, respectively. This behavior agrees with what have been observed for DAS cation, which spans order parameter values from 0.34 to 1.0 depending on the accompanying anion.[1]

The significant increase in the order parameter from 4DEP-T to 4DEP-N2S could be explained because of the stronger T shaped pi-pi interactions promoted by the naphthalene sulfonate anion compared to the benzene anion. However, these T-shaped interactions are present in all of the crystal structures studied herein and they have been already identified in crystal structures with benzene sulfonate anions.[2] Therefore, we propose that strong head-to-tail interactions between the N2S anions helps force the head-to-tail arrangement in the cation layer. This molecular packing leading to optimal order parameters has also been observed for DSNS (4-(4-(dimethylamino)styryl)-1-methylpyridinium naphtalene-2-suflonate) that shares the same N2S anion.[3]

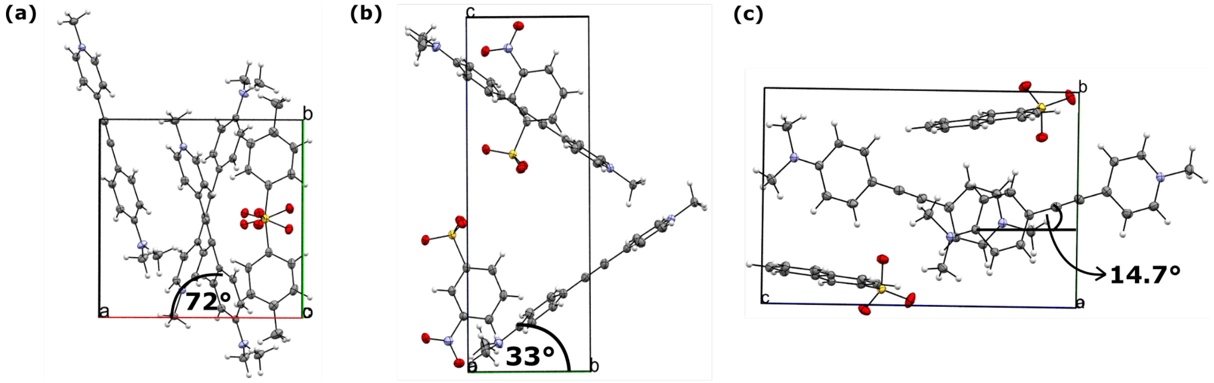

**Figure 2.6** Angle between the different cations and the main crystallographic axis ($\theta_p$) for a) 4DEP-T, b) 4DEP-3NBS and c) 4DEP-N2S.

The XRD measurements provided experimental cation atomic positions with which we could refine our calculations of the molecular hyperpolarizabilities (reported in **Table 2.1** and **Table 2.3**). We recognize the utility of the preliminary gas-phase calculations from **Table 2.2**; despite small changes between specific 4DEP crystals, the ordering of $\beta_{4DEP} > \beta_{DAST} > \beta_{HMQ\text{-}TMS}$ remains (see **Table 2.1**), as attributed to both the decreased inter-ring torsion and increased electron density along the alkynyl π-bridge. 4DEP-3NBS has the largest cation hyperpolarizability, followed by 4DEP-N2S and 4DEP-T.

For a quantitative comparison of the relative magnitude of the macroscopic nonlinear optical susceptibility due to the unique molecular packing, the molecular hyperpolarizabilities, and crystal structures, we compare 4DEP-T, 4DEP-3NBS, 4DEP-N2S, DAST, and HMQ-TMS using the 1D chromophore approximation, $\chi^{(2)} = N F_{ijk} \beta \cos^3(\theta_p)$. If we assume the local field factors $F_{ijk}$ are the same from crystal to crystal, we can calculate a relative $\chi^{(2)}$, as shown in the last column of **Table 2.1.** For this comparison, the relative $\chi^{(2)}$ values are normalized to HMQ-TMS. We see DAST is predicted to be 5% more efficient at THz generation, and in practice DAST has proven to be better at generating higher peak-field strengths than HMQ-TMS. By having a large molecular hyperpolarizability and very good order parameter, we can predict that 4DEP-N2S can have superior THz generation characteristics to both DAST and HMQ-TMS with a calculated relative $\chi^{(2)}$ of 1.34.

**Table 2.1** Comparison of calculated and measured crystalline properties relevant to strong THz generation. All β values are calculated, either using optimized gas phase atomic positions (GAS) or crystallographic positions (EXP). The order parameter and number density N are calculated using the X-ray structure, and the relative χ(2) values are calculated using the 1D chromophore approximation**.**

| | β (×$10^{-30}$ esu) GAS | β (×$10^{-30}$ esu) EXP | Order Parameter | $N$ (Å$^{-3}$) | Relative $\chi^{(2)}$ |
|---|---|---|---|---|---|
| HMQ-TMS | 143 | 186 | 1.00 | 0.001621 | 1.00 |
| DAST | 157 | 201 | 0.83 | 0.001906 | 1.05 |
| 4DEP-T | 204 | 214 | 0.03 | 0.001932 | 0.04 |
| 4DEP-3NBS | 204 | 247 | 0.59 | 0.001849 | 0.86 |
| 4DEP-N2S | 204 | 230 | 0.91 | 0.001926 | 1.34 |

### 2.3.2 Optical characterization and THz generation.

Samples of each 4DEP crystal were tested for THz generation. Sample thicknesses were 1.0, 0.7, and 0.7 mm for 4DEP-T, 4DEP-3NBS and 4DEP-N2S, respectively. Sets of photographs showing each crystal tested can be seen in **Figure 2.7**. The pictures on the left show crystal size whereas the photographs on the right were taken under crossed polarizers and show the crystal polar axis and the generated THz polarization. The crystals were oriented such that their largest face was normal to the pump beam and their polar axis was parallel to the polarization of the pump pulses. All THz generation tests were conducted in a dry air environment at room temperature.

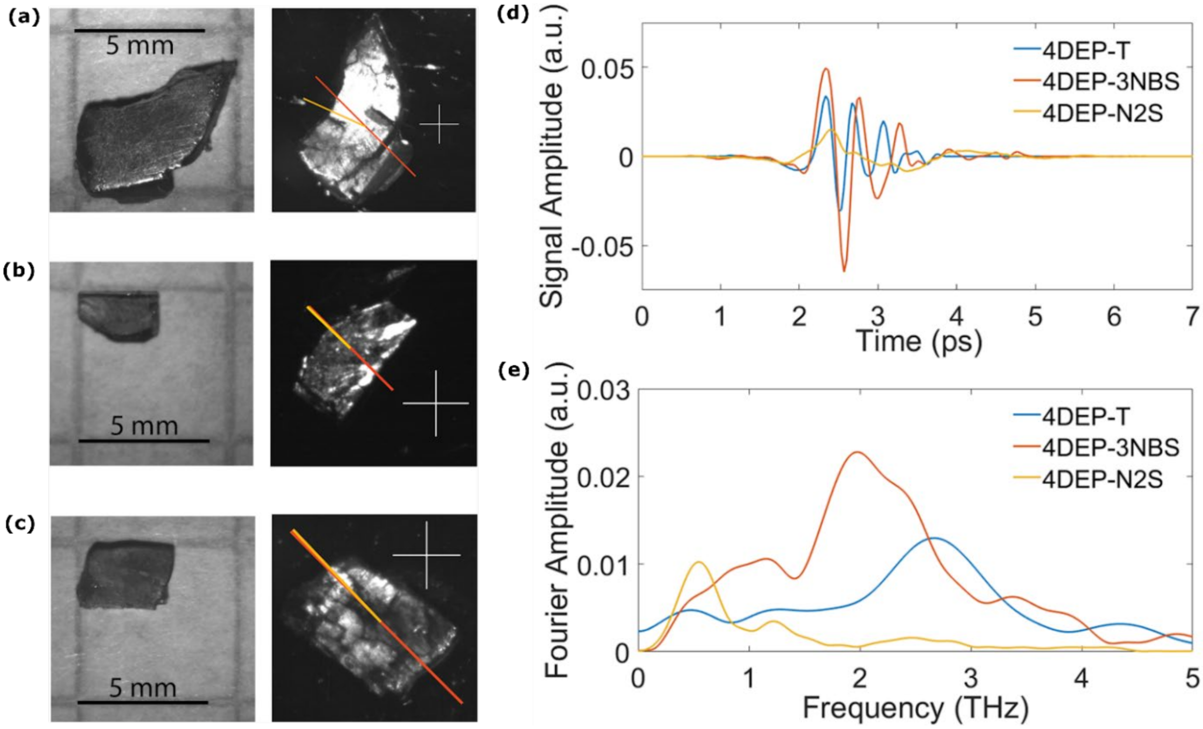

**Figure 2.7** a) Photographs of the 4DEP-T sample. The picture on the right is under crossed polarizers (white lines) and shows the main polar axis (red line) as well as the polarization of the generated THz (orange line). b) Photographs of the 4DEP-3NBS sample. c) Photographs of the 4DEP-N2S sample. d) THz temporal waveforms generated with 4DEP-T, 4DEP-3NBS, and 4DEP-N2S as detected by EO sampling and (e) Fourier transform of the temporal waveforms from d).

**Figure 2.7a-c** shows moderate sized crystals with the 4DEP-T sample having the fewest domains, largest size, and highest crystal quality. Crystal quality has a large effect on THz generation and is the main cause for the results seen in **Figure 2.7d-e**, contrary to the predicted relative $\chi^{(2)}$ values. The polarization of the generated THz radiation, as depicted in **Figure 2.7a-c**, was determined to be 20, 0.4, and 0.8 degrees relative the polarization of the incident light (which was parallel to the polar axis of the crystal) for 4DEP-T, 4DEP-3NBS, and 4DEP-N2S, respectively. The large angle between input and output light polarization in the case of 4DEP-T indicates sizable contributions from off diagonal components of $\chi^{(2)}$ for this crystal cut.

**Figure 2.7d** shows that 4DEP-T and 4DEP-3NBS generate few cycle THz pulses when pumped with 1450 nm light whereas 4DEP-N2S generates a long, single-cycle waveform. A quantitative determination of field strength was not performed due to small crystal size and the low quality of these novel crystals. The broad spectrum, especially in such thick crystals (1 mm compared to <0.5 mm) is also positive preliminary indication of good phase matching between the IR pump light and generated THz radiation. **Figure 2.7e** shows that 4DEP-T generates a nearly continuous spectrum from 0 to 5 THz exhibiting a dip in generation at 3.9 THz. The 4DEP-3NBS spectrum also covers this broad range, but exhibits modulations at 1.4, 3.1, and 4.4 THz. These modulations, along with the relatively narrow spectrum of 4DEP-N2S, are, in part, the result of multiple domains and variations in crystal thickness across the region illuminated for THz generation (see **Figure 2.7a-c**); similarly narrow spectra compared to 4DEP-N2S were observed in lower quality crystals of both other 4DEP variants. As we refine the crystal growth techniques and produce higher quality crystals, we expect a broader spectrum from 4DEP-N2S and significant improvements in THz output of all three crystals.

## 2.4 Conclusions

In conclusion, we developed a novel set of organic THz generation crystals. According to our calculations, the alkyne pyridinium cation 4DEP shows promise as a highly nonlinear optical molecule by virtue of its increased electron density and planarity. The inclusion of 3NBS or N2S anions precludes the co-crystallization of water molecules, as has been observed for 4DEP-T. Additionally, the molecular-packing order parameter shows large variations with the anion, ranging from 0.03 in 4DEP-T to 0.91 in 4DEP-N2S. Due the to the relatively high order parameter and large hyperpolarizability, we predict that 4DEP-N2S should have an improved $\chi^{(2)}$, ~30% larger than HMQ-TMS and DAST. We demonstrate that all three 4DEP crystals generate THz radiation via optical rectification. While low crystal quality currently reduces the THz output, the production of larger, higher quality crystals promises a large gain in THz generation combined with a broad generation spectrum.

## 2.5 Experimental Details

### 2.5.1 Calculations

Finite field (FF) density functional theory calculations with the B3LYP functional at 6-311++G** theory level[24] were used to calculate the optimal gas-phase geometry and static first hyperpolarizability tensor components βijk of the cations of various molecular systems. The total hyperpolarizability is readily calculated according to the following equations:

$$\beta_i = \sum_j (\beta_{ijj} + \beta_{jij} + \beta_{jji})$$ **Eq. 2.1**

$$\beta_{tot} = \sqrt{\beta_x^2 + \beta_y^2 + \beta_z^2}$$ **Eq. 2.2**

### 2.5.2 Synthesis and Crystallization

The 4DEP cation precursor was synthesized using the Sonogashira cross-coupling reaction between 4-bromopyridine and (4-dimethylaminophenyl)alkynyl precursors. The final products were obtained by adding the anion precursors in the last step as is schematically explained on **Figure 2.8**. Via this strategy, we obtained the 4DEP cation paired with 4-methylbenzenesulfonate (T), 3-nitrobenzenesulfonate (3NBS), and naphthalene-2-sulfonate (N2S) anions (**Figure 2.2**). 4DEP-T formed hydrated centric crystals when crystallized with methanol in the presence of trace water. However, non-centrosymmetric structures were obtained when dry methanol was used as the solvent under slow evaporation conditions. 4DEP-N2S and 4DEP-3NBS showed the same crystal structure in dry and water-containing methanol. The crystal conformations were obtained by means of X-Ray analysis and the details for data collection as well as the most important crystal parameters are summarized in the Supporting Information.

### 2.5.3 THz generation and optical characterization

800-nm light from an amplified Ti:sapphire laser was converted in an OPA to 1450 nm (beam diameter of ~5.5 mm, pulse duration of ~100 fs with 0.9 µJ per pulse). Crystal polar axis and pump pulse polarization were both vertical. Excess IR was removed by use of a 1-mm thick Teflon filter. Generated THz then passed through a vertical polarizer and a single off-axis parabolic mirror was used to collect and focus the THz radiation to a GaP electro-optic crystal composed a 100 µm (110) layer bonded to a 1 mm (100) layer (see **Figure 2.10**).

The THz waveforms were measured by electro-optic sampling with ~100 fs 800-nm light pulses.[25] The probe pulse traveled along a delay stage such that the relative timing of the pump and probe pulses could be varied and temporal waveforms obtained. The polarization of the generated waves was determined by removing the polarizer after the crystal and measuring generation before and after rotating the GaP detection crystal by 90 degrees. All other experimental factors remained constant.

Wavelength dependence was determined by changing output wavelength of the OPA and keeping all other experimental factors constant. A Cary 5e spectrophotometer was used to characterize the UV-vis-IR transmission of each molecular system. Samples were dissolved in methanol and percent transmission was measured as a function of wavelength for each molecule, (see **Figure2.9a**).

THz transmission data was collected via THz time-domain spectroscopy. THz radiation was generated in DSTMS and detected via electro-optic sampling in GaP. Samples were oriented such that the incident THz was polarized along the polar axis of the crystal, (see **Figure 2.9b**).

## 2.6 General and Supporting Information

### 2.6.1 Calculation Details

Due to the existence of local energy minima, the final geometry of a gas-phase cation structure optimization can depend upon the initial geometry. Hyperpolarizabilities calculated based on the various optimized gas phase geometries clustered around three values, each associated with a particular geometry. We report the lowest magnitude clustering for 4DEP, DAS, and HMQ, but note that ratios between cation-hyperpolarizabilities in the three ranges were very similar.

**Table 2.2** Zero-frequency first hyperpolarizability tensor components, $\beta_{ijk}$ ($\times 10^{-30}$ esu), of the cations at B3LYP/6-311++G** level using a gas phase optimized geometry.

| | **4DEP** | **DAS** | **HMQ** |
|---|---|---|---|
| $\beta_{xxx}$ | 0.000 | 0.000 | -0.558 |
| $\beta_{xxy}$ | 0.223 | -0.009 | -0.041 |
| $\beta_{xyy}$ | 0.000 | 0.000 | -0.432 |
| $\beta_{yyy}$ | 0.106 | 0.021 | -1.04 |
| $\beta_{xxz}$ | -0.132 | -0.017 | -0.848 |
| $\beta_{xyz}$ | 0.000 | 0.000 | -0.499 |

**Table 2.2** Continued

| | **4DEP** | **DAS** | **HMQ** |
|---|---|---|---|
| $\beta_{yyz}$ | -4.58 | -4.48 | -0.562 |
| $\beta_{xzz}$ | 0.000 | 0.000 | 3.35 |
| $\beta_{yzz}$ | 0.219 | 6.68 | 19.1 |
| $\beta_{zzz}$ | 209 | 161 | -141 |
| $\beta_{x}$ | 0.000 | 0.000 | 2.36 |
| $\beta_{y}$ | 0.548 | 6.65 | 18.1 |
| $\beta_{z}$ | 204 | 157 | -142 |
| $\boldsymbol{\beta_{tot}}$ | **204** | **157** | **143** |

**Table 2.3** Zero-frequency first hyperpolarizability tensor components, $\beta_{ijk}$ (×$10^{-30}$ esu), of the cation of the indicated molecule at B3LYP/6-311++G** level using experimental molecular geometries determined by X-ray crystallography.

| | **4DEP-T** | **4DEP-N2S** | **4DEP-3NBS** | **DAST** | **HMQ-TMS** |
|---|---|---|---|---|---|
| $\beta_{xxx}$ | -7.47 | -19.2 | 0.049 | -169 | 0.170 |
| $\beta_{xxy}$ | -22.2 | -11.3 | -3.29 | -61.8 | 0.320 |
| $\beta_{xyy}$ | -63.4 | -5.11 | -2.87 | -22.8 | 0.595 |
| $\beta_{yyy}$ | -182 | -0.874 | 148 | 8.30 | 0.307 |
| $\beta_{xxz}$ | 1.96 | -37.5 | 1.98 | 6.87 | 21.1 |
| $\beta_{xyz}$ | 4.85 | -23.0 | 2.40 | 3.41 | -0.95 |
| $\beta_{yyz}$ | 11.4 | -10.3 | -96.1 | 1.53 | 0.726 |
| $\beta_{xzz}$ | 0.975 | -75.4 | -1.94 | 3.41 | 58.1 |
| $\beta_{yzz}$ | 2.75 | -46.5 | 62.0 | 1.12 | -3.50 |

**Table 2.3** Continued

| | 4DEP-T | 4DEP-N2S | 4DEP-3NBS | DAST | HMQ-TMS |
|---|---|---|---|---|---|
| $\beta_y$ | -202 | -58. | 207 | -68.9 | -2.87 |
| $\beta_{zzz}$ | -0.813 | -151 | -40.7 | -0.96 | 152 |
| $\beta_x$ | -69.9 | -100. | -4.77 | -188 | 66.9 |
| $\beta_z$ | 12.6 | -199 | -135 | 7.44 | 174 |
| $\boldsymbol{\beta_{tot}}$ | **214** | **230** | **247** | **201** | **186** |

### 2.6.2 Synthesis

The 4DEP cation precursor was synthesized by means of the Sonogashira cross-coupling reaction[1] and the different anions were added by a methylation reaction at high temperature (**Figure 2.8**). Firstly, N,N-dimethyl-4-((trimethylsilyl)ethynyl)aniline (**2**) was synthesized from 4-bromo-N,N-dimethylaniline (**1**) and the TMS group removed according to the method previously reported by Leonard et al.[2] Subsequently, the unprotected alkyne molecule was reacted with 4-bromopyridine (**3**) according to the method of Umezawa *et al*[3] to yield N,N-dimethyl-4-(pyridin-4-ylethynyl)aniline. The final pyridin-1-ium products (**4**) were obtained by high temperature methylation reactions in toluene. Overall reaction yields from 59 to 62% were obtained.

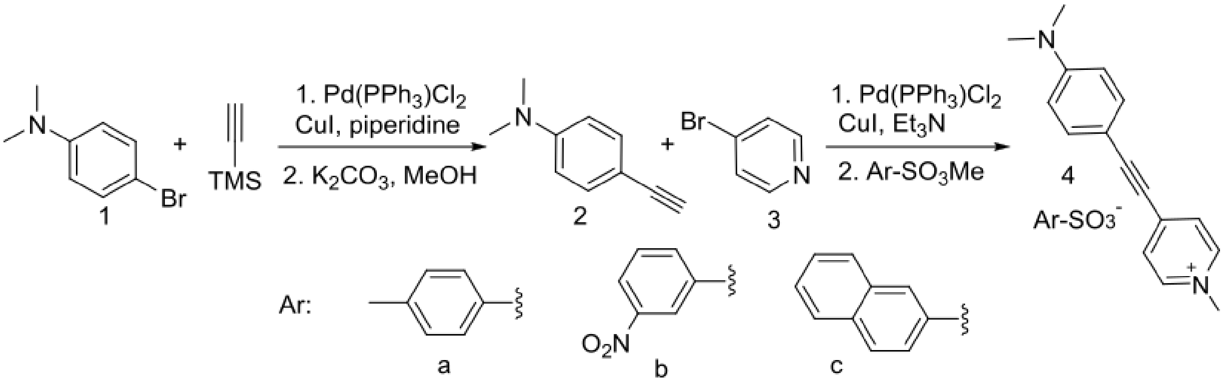

**Figure 2.8** Organic Synthesis scheme for 4DEP-T (4a), 4DEP-3NBS (4b) and 4DEP-N2S (4c).

NMR data was collected with an INOVA 500 MHz Spectrometer. All of the shifts were reported relative to tetramethylsilane. *4-((4-(dimethylamino)phenyl)ethynyl)-1-methylpyridin-*

*1-ium 4-methylbenzenesulfonate (4DEP-T)* ***(5a)****:* Yield: 59% $^1$H-NMR (500 MHz, $CD_3OD$): δ= 8.71 (d, J: 6.7 Hz, 2H), 7.95 (d, J: 6.7 Hz, 2H), 7.73 (d, J: 8.1 Hz, 2H), 7.54 (d, J: 9 Hz, 2H), 7.25 (d, J: 8 Hz, 2H), 6.81 (d, J: 9Hz, 2H), 4.32 (s, 3H), 3.10 (s, 6H), 2.39 (s, 3H).

*4-((4-(dimethylamino)phenyl)ethynyl)-1-methylpyridin-1-ium 3-nitrobenzenesulfonate (4DEP-3NBS)* ***(5b)****:* Yield: 60% , $^1$H-NMR ( 500 MHz, $CD_3OD$): δ= 8.69 (d, J: 6.7 Hz, 2H), 8.61 (s, 1H), 8.30 (dd, $J_1$: 1.3 Hz, $J_2$: 8.2 Hz, 1H), 8.18 (d, J: 7.7 Hz, 1H), 7.92 (d, J: 6.7 Hz, 2H), 7.69 (t, J: 8 Hz, 1H ), 7.50 (d, J: 9 Hz, 2H), 6.78 (d, J: 9 Hz, 2H), 4.31 (s, 3H), 3.07 (s, 6H).

*4-((4-(dimethylamino)phenyl)ethynyl)-1-methylpyridin-1-ium naphthalene-2-sulfonate (4DEP-N2S)* ***(5c)***: Yield: 62% $^1$H-NMR (500 MHz, $CD_3OD$): δ= 8.66 (d, 2H), 8.33 (s, 1H), 7.95-7.87 (m, 6H), 7.576-7.52 (m, 2H), 7.50 (d, 2H), 6.77 (d, 2H), 4.28 (s, 3H), 3.07 (s, 6H).

### 2.6.3 X-rays diffraction experiments.

The procedure for obtaining X-ray data for 4DEP-3NBS and 4DEP-N2S was the same: A dark red crystal was harvested under oil in ambient conditions and placed at the tip of a polyimide loop. The crystal was mounted in a stream of cold $N_2$ and centered in the X-ray beam using a video camera. Low-temperature (100 K) X-ray diffraction data comprising $\varphi$- and $\omega$-scans were then collected using a MACH3 kappa goniometer coupled to a Bruker Apex II CCD detector with a Bruker-Nonius FR591 rotating anode X-ray source producing Cu $K_\alpha$ radiation ($\lambda$ = 1.54178 Å). The Bruker APEX3 suite was used to process the data; reflection intensities were integrated through the program SAINT, and appropriate absorption corrections were applied to the intensities via a multi-scan method using the program SADABS.

**Table 2.4** X-ray crystallographic data.

| **Compound** | **4DEP-T[3]** | **4DEP-N2S** | **4DEP-3NBS** |
|---|---|---|---|
| Formula | $C_{23}H_{24}N_2O_3S$ | $C_{26}H_{24}N_2O_3S$ | $C_{22}H_{21}N_3O_5S$ |
| Formula weight | 408.5 | 444.53 | 439.48 |
| Crystal System | Monoclinic | Monoclinic | Monoclinic |
| Space Group | *Cc* | *Pc* | $P2_1$ |
| Point Group | *m* | *m* | *2* |
| $a$ (Å) | 11.195(6) | 7.8508(7) | 9.1815(13) |
| $b$ (Å) | 10.424(5) | 9.6312(8) | 6.5155(9) |
| $c$ (Å) | 18.10(2) | 14.3303(13) | 17.774(2) |
| α (˚) | 90 | 90 | 90 |
| β (˚) | 101.39(6) | 93.548(4) | 102.384(4) |
| γ (˚) | 90 | 90 | 90 |
| V (Å$^3$) | 2070.6 | 1081.47(16) | 1038.5(2) |
| Z | 4 | 2 | 2 |
| Dx (Mg/m$^3$) | 1.310 | 1.365 | 1.405 |
| No. of total reflections | 2656 | 24569 | 26978 |
| No. of unique reflections | 2318 | 3966 | 3777 |
| R | 0.047 | 0.0252 | 0.0365 |
| wR2 | 0.056 | 0.0647 | 0.1058 |

The structure was solved using dual-space methods in SHELXT[4] and refined against $F^2$ on all data by full-matrix least squares with SHELXL-2014[5] using established refinement strategies.[6] All non-hydrogen atoms were refined anisotropically. The positions of all hydrogen atoms were calculated geometrically and refined using a riding model. The positions of the remaining hydrogen atoms were taken from the difference Fourier synthesis and subsequently refined semi-freely with the help of appropriate distance restraints. The isotropic displacement parameters of all hydrogen atoms were constrained to be 1.2 times the $U_{eq}$ value (1.5 for methyl hydrogens) of the atom to which they are bound. Details of the crystal structures are listed in **Table 2.4**, as well as crystal data for 4DEP-T, as it was previously reported.[3]

### 2.6.4 Optical characterization

Samples were dissolved in methanol and percent transmission was measured as a function of wavelength for each molecule, (see **Figure 2.9a**). The minimum transmission for 4DEP-3NBS and 4DEP-N2S and 4DEP-T occur at 448, 448, and 446 nm, respectively. All three show similar transmission features with full transmission above 600 nm.

THz transmission data was collected via THz time-domain spectroscopy. THz radiation was generated in DSTMS and detected via electro-optic sampling in GaP, as described in the experimental details. Samples were oriented such that the incident THz was polarized along the polar axis of the crystal. The results of our THz transmission measurements can be seen in **Figure 2.9b**. We note that although grain boundaries and crystal impurities decrease transmission and the samples were not free of crystal defects, both 4DEP-T and 4DEP-3NBS show high transmission from 0.25 to 2 THz. 4DEP-T transmits well along all frequencies above 1 THz and is especially transparent below 1 THz.

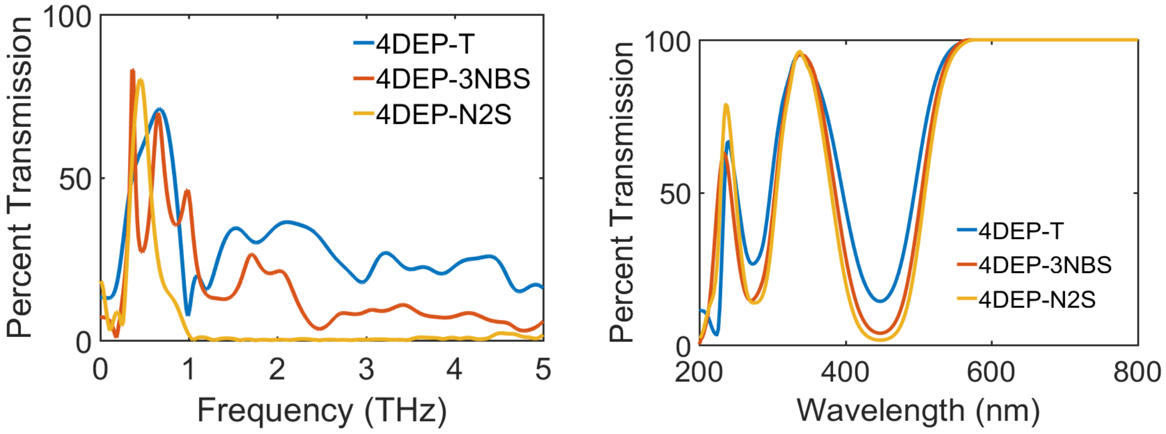

(a) (b)

**Figure 2.9** (a) UV-vis-IR and (b) THz transmission spectra of 4DEP-N2S, 3NBS and T.

### 2.6.5 THz generation.

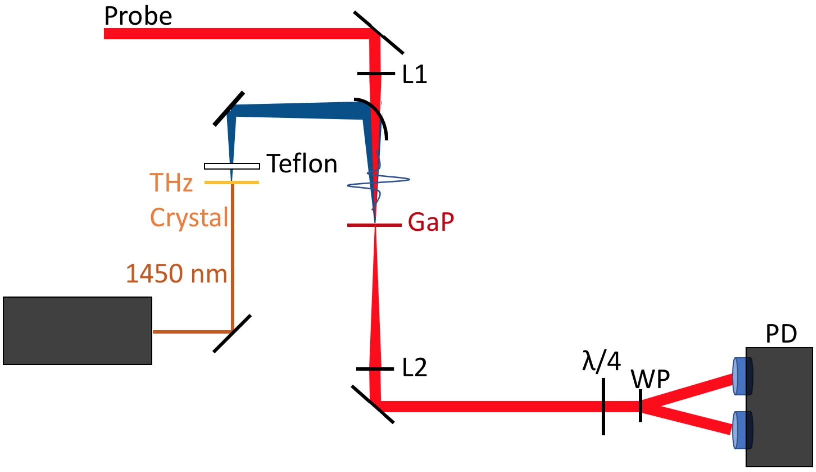

**Figure 2.10** Experimental setup for THz generation. 1450-nm light from the optical parametric amplifier generates THz in the THz Crystal through optical rectification. Excess IR light is removed using a Teflon filter. THz light is then focused onto GaP using an off axis parabolic mirror. The 800-nm probe beam is also focused (L1) onto the GaP, where the THz electric field profile is imprinted on the probe pulse, the beam is re-collimated (L2), and directed to a λ/4 waveplate and Wollaston Prism (WP). The intensities of the split beams are monitored with balanced photodiodes (PD).

We furthermore characterized the dependence of THz field strength on pump wavelength. **Figure 2.11** shows that THz field strength generally increases with increasing wavelength. This pattern is likely due to better phase matching between IR and THz light at longer IR wavelengths. Velocity matching at long IR wavelengths results in peaks in conversion efficiency for benchmark crystals such as HMQ-TMS and DAST. An additional benefit of mid IR pumping is the decreased photodegradation from multiphoton absorption. In this regard, 4DEP cation contains an alkyne bridge which is generally less photostable than an alkene bridge. Regular tests of 4DEP-T over the course of a month and a half show no significant degradation (see **Figure 2.12**).

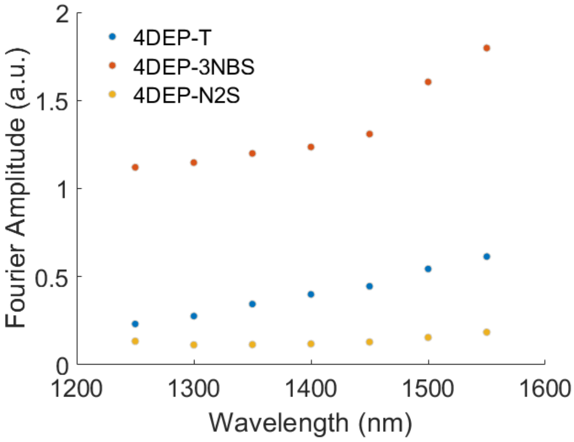

**Figure 2.11** Integrated Fourier amplitude of 4DEP-T, 4DEP-3NBS, and 4DEP-N2S pumped at various wavelengths, corrected for OPA output power.

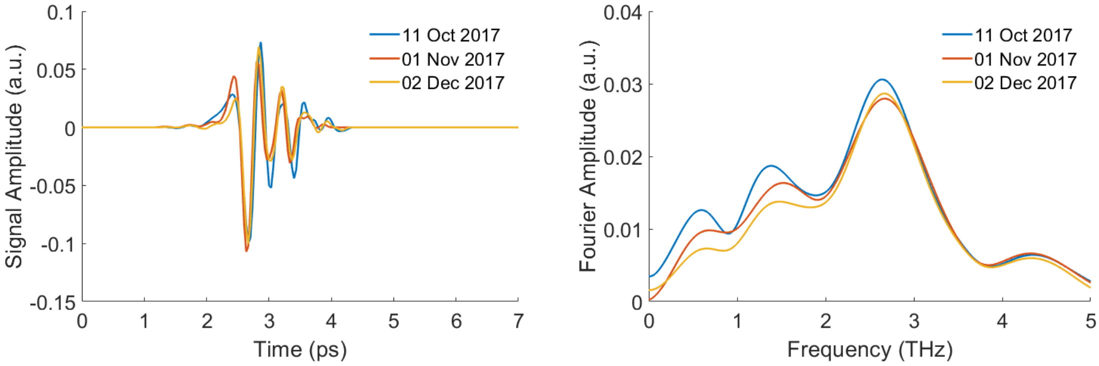

**Figure 2.12** Temporal waveforms and corresponding Fourier transforms generated by 4DEP-T. The sample crystal was exposed regularly over the course of a month and a half and stored at room temperature and ambient humidity.

## 2.7 References

[1] K. Ajito, J.-Y. Kim, Y. Ueno, H.-J. Song, K. Ueda, W. Limwikrant, K. Yamamoto, K. Moribe, *Journal of The Electrochemical Society* **2014**, 161, B171; K. Ajito, Y. Ueno, *IEEE Transactions on Terahertz Science and Technology* **2011**, 1, 293.

[2] K. W. Kim, H. Kim, J. Park, J. K. Han, J.-H. Son, *IEEE Transactions on Terahertz Science and Technology* **2012**, 2, 99; K. Ajito, *IEEE Transactions on Terahertz Science and Technology* **2015**, 5, 1140.

[3] L. Xie, Y. Yao, Y. Ying, *Applied Spectroscopy Reviews* **2014**, 49, 448; A. Dobroiu, Y. Sasaki, T. Shibuya, C. Otani, K. Kawase, *Proceedings of the IEEE* **2007**, 95, 1566.

[4] Z. Zheng, C. Zhao, S. Lu, Y. Chen, Y. Li, H. Zhang, S. Wen, *Optics Express* **2012**, 20, 23201; S. Chen, C. Zhao, Y. Li, H. Huang, S. Lu, H. Zhang, S. Wen, *Optical Materials Express* **2014**, 4, 587.

[5] T. Kampfrath, K. Tanaka, K. A. Nelson, *Nature Photonics* **2013**, 7, 680.

[6] T. Hattori, K. Takeuchi, *Optics express* **2007**, 15, 8076.

[7] T. Tanabe, K. Suto, J.-i. Nishizawa, K. Saito, T. Kimura, *Applied physics letters* **2003**, 83, 237.

[8] Y. S. Lee, T. Meade, V. Perlin, H. Winful, T. B. Norris, A. Galvanauskas, *Applied Physics Letters* **2000**, 76, 2505.

[9] M. Shalaby, C. P. Hauri, *Nature Communications* **2015**, 6, ncomms6976.

[10] I. Katayama, R. Akai, M. Bito, H. Shimosato, K. Miyamoto, H. Ito, M. Ashida, *Applied Physics Letters* **2010**, 97, 021105.

[11] P. Y. Han, M. Tani, F. Pan, X. C. Zhang, *Optics Letters* **2000**, 25, 675.

[12] Z. Yang, L. Mutter, M. Stillhart, B. Ruiz, S. Aravazhi, M. Jazbinsek, A. Schneider, V. Gramlich, P. Guenter, *Advanced Functional Materials* **2007**, 17, 2018.

[13] F. D. J. Brunner, O. P. Kwon, S.-J. Kwon, M. Jazbinšek, A. Schneider, P. Günter, *Optics express* **2008**, 16, 16496.

[14] J.-H. Jeong, B.-J. Kang, J.-S. Kim, M. Jazbinsek, S.-H. Lee, S.-C. Lee, I.-H. Baek, H. Yun, J. Kim, Y. S. Lee, *Scientific reports* **2013**, 3.

[15] S.-H. Lee, M. Jazbinsek, C. P. Hauri, O. P. Kwon, *CrystEngComm* **2016**, 18, 7180.

[16] O. P. Kwon, B. Ruiz, A. Choubey, L. Mutter, A. Schneider, M. Jazbinsek, V. Gramlich, P. Günter, *Chemistry of materials* **2006**, 18, 4049.

[17] P. N. Prasad, D. J. Williams, *Introduction to nonlinear optical effects in molecules and polymers*, Wiley, **1991**.

[18] J. Zyss, J. L. Oudar, *Physical Review A* **1982**, 26, 2028.

[19] J. Yin, L. Li, Z. Yang, M. Jazbinsek, X. Tao, P. Günter, H. Yang, *Dyes and Pigments* **2012**, 94, 120.

[20] H. Umezawa, S. Okada, H. Oikawa, H. Matsuda, H. Nakanishi, *Bulletin of the Chemical Society of Japan* **2005**, 78, 344.

[21] H. Umezawa, S. Okada, H. Oikawa, H. Matsuda, H. Nakanishi, *Journal of physical organic chemistry* **2005**, 18, 468.

[22] Z. Yang, M. Jazbinsek, B. Ruiz, S. Aravazhi, V. Gramlich, P. Günter, *Chemistry of materials* **2007**, 19, 3512; Z. Yang, S. Aravazhi, A. Schneider, P. Seiler, M. Jazbinsek, P. Günter, *Advanced Functional Materials* **2005**, 15, 1072; J. Ogawa, S. Okada, Z. Glavcheva, H. Nakanishi, *Journal of Crystal Growth* **2008**, 310, 836; R. J. Vijay, N. Melikechi, T. Thomas, R. Gunaseelan, M. A. Arockiaraj, P. Sagayaraj, *Journal of Crystal Growth* **2012**, 338, 170.

[23] B. Ruiz, Z. Yang, V. Gramlich, M. Jazbinsek, P. Günter, *Journal of Materials Chemistry* **2006**, 16, 2839.

[24] J. P. Perdew, *Physical Review B* **1986**, 33, 8822.

[25] Q. Wu, X. C. Zhang, *Applied Physics Letters* **1997**, 70, 1784.

# Chapter 3 Terahertz generation and optical characteristics of P-BI

## 3.1 Overview

We present the structural and THz generation characteristics of the molecular salt crystal (E)-2-(4-(dimethylamino)styryl)-1,1,3-trimethyl-1H-benzo[e]indol-3-ium iodide (P-BI) using optical rectification with IR pump wavelengths. In previous work, P-BI demonstrated more efficient second-harmonic generation compared to DAST, but no THz generation properties were reported. In our measurements, P-BI shows a peak-to-peak field ~6 times greater than inorganic crystal GaP, and a broader THz spectrum. Data was obtained from 0 to 6 THz showing a significant dip in generation at 1.8 THz, similar to what has been observed with the THz generation crystal DAST at 1 THz. We characterized the power dependence of P-BI at different IR wavelengths, with optimal THz generation at the 1550-nm pump wavelength. In order to model THz generation as a function of P-BI crystal thickness, we measured the THz complex refractive index and the IR group index; modeling shows that imperfect phase matching leads to spectral narrowing centered at ~2.5 THz as the crystal thickness is increased. P-BI could provide a useful alternative to inorganic THz generation crystals such a GaP. The following work was published in Optics Letters, 44(17), 4279.

## 3.2 Introduction

Terahertz spectroscopy has emerged as a promising field with an increasing number of applications in medical imaging,[1] transportation security,[2] and spectroscopy[3]. To generate terahertz radiation, several methods have been used including photoconductive antennas,[4] laser-induced plasma generation[5] of THz, and molecular nonlinear optical (NLO) crystals that generate THz via optical rectification (OR)[6] and difference frequency generation (DFG).[7] In OR THz generation, an ultrafast laser pulse is directed to a NLO crystal and THz pulses are produced with the THz bandwidth related to the pump laser pulse bandwidth and the NLO crystal characteristics. A number of inorganic crystals such as $LiNbO_3$,[8] ZnTe,[9] and GaP[10] have been used for OR THz generation. ZnTe and GaP are likely the most broadly used crystals for electro-optic sampling. However, low conversion efficiencies, limited spectral bandwidths, or sophisticated tilted-pulse front setups as in the case of $LiNbO_3$, have limited the broad applicability of inorganic materials for THz generation. On the other hand, several organic molecular crystals like DAST[6] and OH1[11] have been developed for THz generation and detection due to better conversion efficiencies with relatively simple optical setups.

Fundamental material characteristics of molecular crystals for THz generation are non-centrosymmetric molecular packing,[12] high molecular hyperpolarizability,[13] and a low dielectric constant[14] that allows easier fulfillment of phase-matching conditions. In addition to these three essential characteristics, high-power THz generation requires the production of high-quality crystals of reasonable sizes, and this has been challenging. To design organic materials that form large crystals while displaying the necessary material characteristics, both neutral and ionic molecules have been developed. An important advantage of organic salts over neutral compounds is their potential to pair various anions with the same THz-generating cation. This versatility can impact material characteristics, such as crystal growth ability,[15] the magnitude of the second-order susceptibility,[16] and the THz spectral profile.[17]

In the design of molecular salt crystals, aromatic systems are often chosen for both the anion and cation to promote pi-pi interactions that can lead to good molecular arrangements as well as naturally optimized cleaving planes.[18] However, in some cases, relatively large crystals have been grown with much simpler anions such as iodide and $PF_6^-$.[19, 20] One compound designed to feature these small anions is ((E)-2-(4-(dimethylamino)styryl)-1,1,3-trimethyl-1H-benzo[e]indol-3-ium iodide) P-BI, which combines a benzo[e]indol-3-ium cation with an iodide anion. In a previous study, P-BI-1, a polymorph of P-BI grown in methanol, was tested for second harmonic generation efficiency and showed promising results.[19] However, to the best of our knowledge, THz generation and optical characterization assays have not been performed for this NLO crystal. Here we characterize the structural, optical, and THz properties of P-BI-1 crystal (it will be referred to as P-BI for the rest of this manuscript), which displays stronger THz generation than the common inorganic THz generation crystal GaP.

## 3.3 Results and discussions

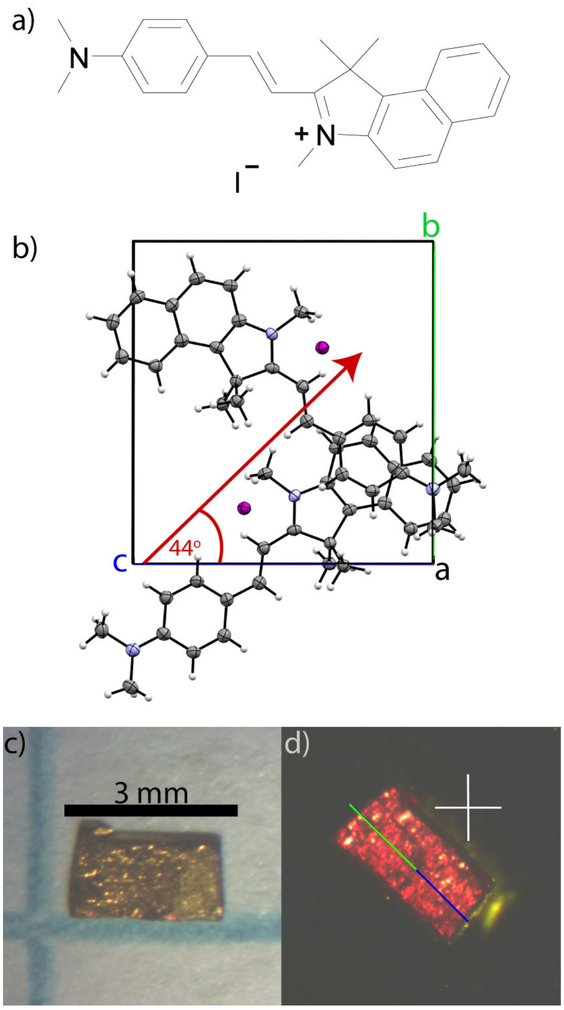

**Figure 3.1** Molecular (a) and crystal structure (b) of P-BI. (c) Photograph of a P-BI crystal. (d) Photograph between crossed polarizers (polarizer directions shown by white lines). The green line indicates the polar axis, which is parallel to the THz generation axis shown by the dark blue line.

P-BI was synthesized by condensation of 1,1,2,3-tetramethyl-1H-benzo[e]indol-3-ium iodide with 4-dimethylamino benzaldehyde in presence of piperidine as catalyst. The final product was recovered as the iodide salt after filtration and washing several times with toluene for further purification. In order to obtain crystals for THz generation, the compound was crystallized by slow evaporation in methanol. The molecular structure of P-BI features a dimethylamino electron-donating group and a benzoindolium accepting group (see **Figure 3.1a**). P-BI exhibits a purple color in solution, accompanied by a longer wavelength of maximum absorption of 550 nm, which can limit opportunities for pumping at shorter wavelengths.

A previously reported crystal structure of P-BI (CCDC: 1063291) was collected at room temperature, but the structure is incomplete; two alkene hydrogen atoms are missing.[19] Therefore, we collected X-ray diffraction (XRD) data for P-BI at 100 K to further refine the structure. As shown in **Figure 3.1b**, the final, optimized model (CCDC: 1864169) includes the two previously missing alkene hydrogens. Analysis of the refined crystal structure shows an angle of 44° between the polar (b) axis of the crystal and the charge transfer axis of the molecule. XRD measurements show that P-BI crystals grow predominantly in the a-b direction, influencing our ability to control the thickness and surface area of a (001) crystal independently. Large crystals (up to 1 cm2) were obtained after two weeks, and subsequently cut and polished down to <0.5 mm thickness. **Figure 3.1c** and **d** show photographs of a representative P-BI crystal. The main (001) face has dimensions of about 2.5 mm x 1.5 mm with a thickness of 338 μm. **Figure 3.1d** was recorded under a crossed polarizer and shows that the polar axis of the crystal (blue) and the generation axis (green) are essentially collinear.

THz generation using a P-BI crystal was measured by electro-optic (EO) sampling. In order to pump the P-BI crystal, 800-nm light from a 1 kHz Ti:sapphire laser was transformed in an optical parametric amplifier to 1250-1550 nm pulses with pulse duration ~100 fs. The beam radius was ~3.8 mm with 0.7 μJ energy per pulse giving a maximum fluence of ~1.5 mJ/cm2. Because the P-BI crystal (2.5 x 1.5 x 0.338 mm) was smaller than the pump beam size, it was mounted on an aperture that allowed a portion of the pump light to pass through the crystal for THz generation. The P-BI crystal was oriented such that the (001) face was normal to the pump beam with the polar axis parallel to the polarization of the IR pump pulses. The generated THz was polarized parallel to the crystal polar axis. A 1 mm Teflon filter removed unwanted IR and visible light. The THz beam naturally diverged to fill a 2-inch diameter, 2-inch effective focal length off-axis parabolic mirror, and the THz was directed and focused to a 100 μm (110) GaP bonded to a 1 mm (001) collinearly with 800-nm probe pulses for EO detection. Due to THz absorption in the Teflon, the active GaP thickness, and the ~100 fs probe pulse duration, the detection bandwidth is restricted to less than 6 THz.

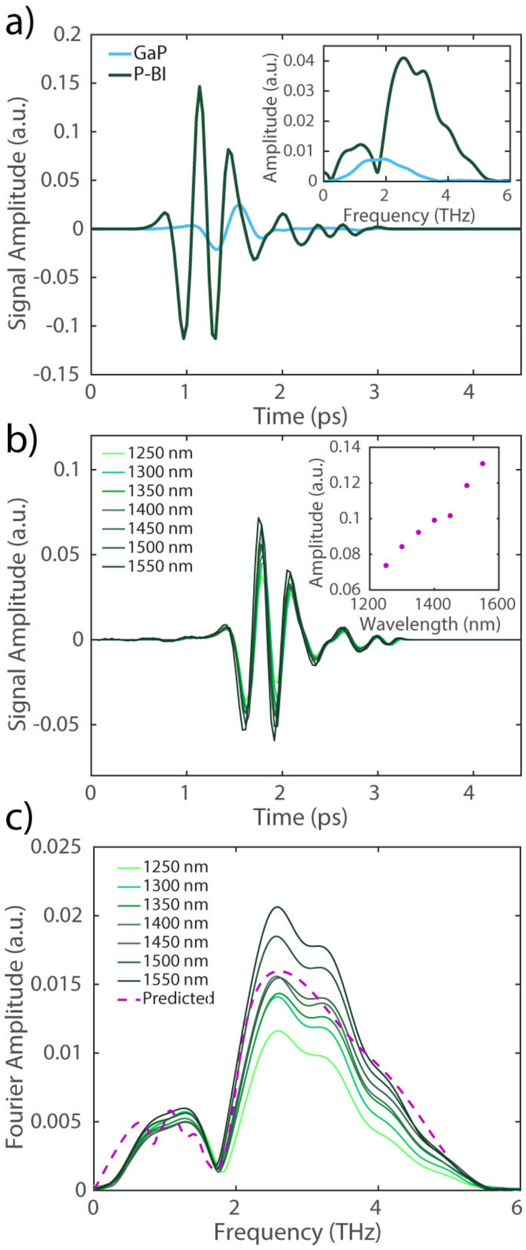

**Figure 3.2** (a) THz waveform of P-BI compared to GaP and HMQ-TMS at 1450 nm pump. The inset shows the corresponding spectra. (b) THz waveform of P-BI pumped at different wavelengths. The inset shows the peak-to-peak signal as a function of pump wavelength. (c) Corresponding spectra compared to the modeled spectrum.

In **Figure 3.2a**, we compare the ~2 cycle THz electric fields produced from P-BI (dark green trace) to a THz pulse from a 300 μm (110) GaP crystal (light blue trace) and a 340 μm HMQ-TMS crystal (purple trace). For an accurate comparison, the GaP and HMQ-TMS crystals[21] were placed on the same aperture as the smaller P-BI crystal and pumped with the same 1.5 mJ/cm2 fluence 1450 nm light.

**Figure 3.2a** shows an approximately 6× times greater peak-to-peak electric field strength from P-BI compared to GaP at 1450 nm, as well as a broader spectrum (see the inset to **Figure 3.2a**). The peak electric field is about half HMQ-TMS, but P-BI shows a smoother spectrum above 2 THz and similar amplitude from 3 to 5.5 THz. **Figure 3.2b** shows the generated THz electric field for pump wavelengths ranging from 1250 nm to 1550 nm with fixed pump-pulse fluence of 0.43 mJ/cm2, and **Figure 3.2c** shows the corresponding Fourier transforms, with broad spectra extending out to ~5.5 THz and a noticeable dip due to a phonon-absorption at 1.8 THz; this is similar to DAST [8] and DSTMS [24], which both show strong absorptions at ~1 THz. The inset to **Figure 3.2b** shows the peak-to-peak THz signal as a function of pump wavelength, showing an increase in THz output with longer wavelengths. The spectra in **Figure 3.2c** show that this increase mainly comes in the 2-5 THz range, due to improved THz-pump phase matching at longer wavelengths. With THz and optical characterization that we describe below, we can calculate the predicted spectrum given by the dashed purple line in **Figure 3.2c**, which shows fairly good agreement with the measured spectra.

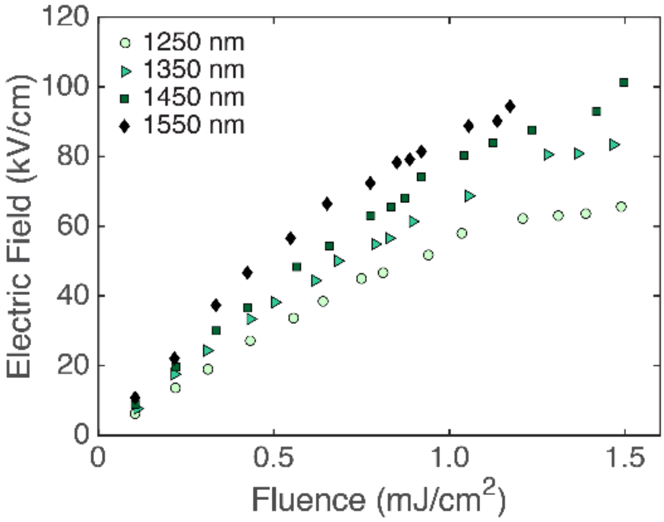

**Figure 3.3** THz peak-to-peak signal strength of P-BI as a function of pump fluence at various wavelengths

**Figure 3.3** shows the generated THz peak-to-peak field as a function of pump pulse energy at select pump wavelengths. We again see the direct relationship between increasing field strength and pump wavelength. At low powers, we see the typical linear field-strength dependence on pump energy leading to saturation at the highest pump energies. The data also indicate that short pump wavelengths saturate more quickly than longer wavelengths of equal power.

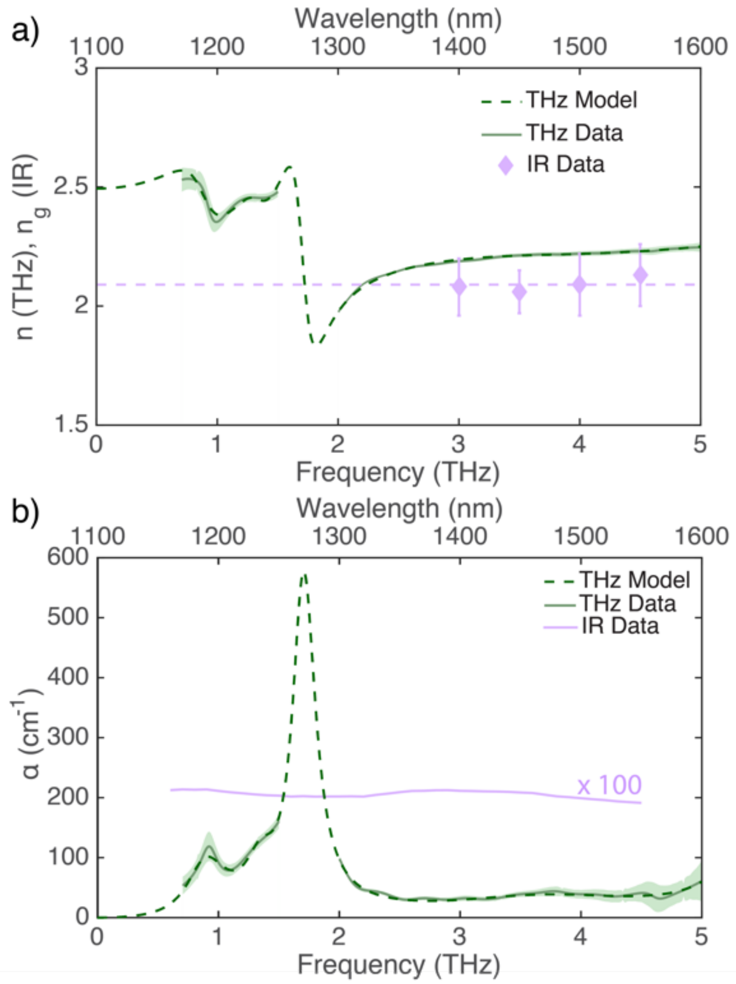

**Figure 3.4** a) The measured (green solid line with light green shading indicating standard error) and fitted (dark dashed line) values for the THz refractive index. The IR group refractive index for P-BI is displayed with pink diamonds and error bars and the dashed line shows the average value. b) The measured (solid) and fitted (dashed) values for THz absorption coefficient. The IR absorption coefficient is amplified by

To better understand the THz generation characteristics, we characterized the relevant THz and optical properties. THz time-domain spectroscopy (THz-TDS) was used to determine the crystal thickness and extract the complex refractive index using the method employed by Dorney et. al [25]. The P-BI crystal under consideration was 338 ± 2 µm thick (as determined from the THz-TDS) with refractive index near 2.2 and absorption features at 0.85, 1.35, 1.69, 3.75, and 5.452THz, as shown in **Figure 3.4**. The absorption at 1.73 THz was so strong that it made it difficult to determine the refractive index and absorption coefficient from ~1.5-2 THz. Therefore, the extracted refractive index data was fit to a Lorentz oscillator model with five oscillators for subsequent modeling to better interpolate in this region [14]. The THz refractive index and absorption coefficient with standard error bars indicated by light-green shading, and

Lorentz oscillator fit results are shown in **Figure 3.4a**. The feature in the THz refractive index at 1.69 THz is the most significant with an oscillator strength more than three times larger than the next strongest resonance, as well as a relatively narrow line width. This resonance creates the main absorption evident in the generated spectrum in **Figure 3.2**.

The infrared group index was determined in a simple auto-correlation scheme.[24] The group index was recorded for IR wavelengths ranging from 1400 to 1550 nm. **Figure 3.4a** displays the average value (light pink dashed line) and the pink diamonds with error bars show a slight increase moving to longer wavelengths. This small increase in group index improves phase-matching and helps explain the observed increase of THz generation efficiency with longer wavelengths. The modeled generation spectrum in **Figure 3.2c** is calculated using the average value of the measured group index.

IR absorption in the P-BI crystal was also measured, with the IR polarization parallel to the P-BI polar axis; the pink solid line at the bottom of **Figure 3.4b** shows the IR absorption coefficient. Across the range of tested wavelengths, IR absorption is much lower than THz absorption with an average value of less than 2.5 cm-1. With the THz complex refractive index and the IR group index, we can model and predict THz spectra, generation length, and coherence length for crystals of varying thickness. (See equations 5, 6, and 7 in Ref. 13).

**Figure 3.5a** shows the calculated coherence length for P-BI as a function THz frequency for 3 group index values. We see that the coherence length varies significantly with frequency and reaches a maximum near 2.3 THz. This leads to the maximum in the THz generation spectrum seen in **Figure 3.2c**. The generation length displayed in **Figure 3.5b** essentially shows what thickness of the 338 μm crystal contributes to THz generation. Using the coherence and generation length, we can also model the complete generation spectrum (shown above in **Figure 3.2c** and in **Figure 3.5c**). All crystal thicknesses produce spectra without much frequency content at 1.7 THz due to the internal absorption. The spectrum modeled based on the a 200 μm P-BI crystal offers the broadest spectrum with spectral amplitude extending past 5 THz.

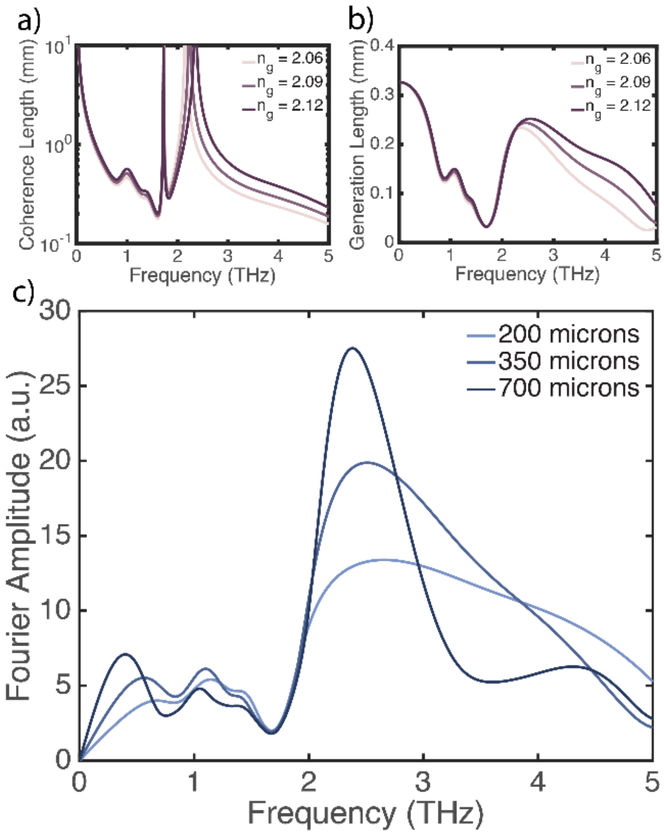

**Figure 3.5** (a) Frequency-dependent P-BI THz generation coherence length calculated for different IR group index values. (b) Frequency-dependent THz generation length for a 338 μm thick crystal. (c) Predicted THz spectra for 1450 nm pump and three P-BI crystal thicknesses.

We have demonstrated THz generation from a P-BI crystal, with peak-to-peak amplitude ~6 times larger than GaP at 1450 nm. We characterized the IR pump wavelength dependence of the obtained THz, finding the maximum amplitude at the longest wavelength measured (1550 nm). We characterized a complete crystal structure compared to that reported previously,[19] and we characterized the THz and optical properties of P-BI. P-BI offers good potential for phase matching as well as very low IR absorbance and low THz absorbance above 3 THz. Finally, P-BI generates a fairly broad spectrum for thin crystals, or more intense narrowband THz centered at 2.5 THz for thicker crystals.

## 3.4 References

[1] Z. D. Taylor, R. S. Singh, D. B. Bennett, P. Tewari, C. P. Kealey, N. Bajwa, M. O. Culjat, A. Stojadinovic, H. Lee, J.-P. Hubschman, E. R. Brown, W. S. Grundfest, *IEEE Trans. Terahertz Sci. Technol.* **2011**, 1, 201.

[2] J. F. Federici, B. Schulkin, F. Huang, D. Gary, R. Barat, F. Oliveira, D. Zimdars, *Semicond. Sci. Technol.* **2005**, 20, S266; A. Dobroiu, Y. Sasaki, T. Shibuya, C. Otani, K. Kawase, *Proc. IEEE* **2007**, 95, 1566.

[3] K. Ajito, *IEEE Trans. Terahertz Sci. Technol.* **2015**, 5, 1140; L. Xie, Y. Yao, Y. Ying, *Appl. Spectrosc. Rev.* **2014**, 49, 448.

[4] S. Matsuura, M. Tani, K. Sakai, *Appl. Phys. Lett.* **1997**, 70, 559.

[5] K.-Y. Kim, J. H. Glownia, A. J. Taylor, G. Rodriguez, *IEEE J. Quantum Electron.* **2012**, 48, 797.

[6] C. P. Hauri, C. Ruchert, C. Vicario, F. Ardana, *Applied Physics Letters* **2011**, 99, 161116.

[7] C. Bernerd, P. Segonds, J. Debray, T. Notake, M. Koyama, H. Minamide, H. Ito, B. Boulanger, *Opt. Lett.* **2018**, 43, 1818.

[8] K. L. Yeh, M. C. Hoffmann, J. Hebling, K. A. Nelson, *Appl. Phys. Lett.* **2007**, 90, 171121.

[9] F. Blanchard, L. Razzari, H. C. Bandulet, G. Sharma, R. Morandotti, J. C. Kieffer, T. Ozaki, M. Reid, H. F. Tiedje, H. K. Haugen, F. A. Hegmann, *Opt. Express* **2007**, 15, 13212.

[10] T. Tanabe, K. Suto, J.-i. Nishizawa, K. Saito, T. Kimura, *Appl. Phys. Lett.* **2003**, 83, 237.

[11] F. D. J. Brunner, O. P. Kwon, S.-J. Kwon, M. Jazbinšek, A. Schneider, P. Günter, *Optics Express* **2008**, 16, 16496.

[12] G. K. Kitaeva, *Laser Phys. Lett.* **2008**, 5, 559.

[13] V. Krishnakumar, R. Nagalakshmi, *Physica B: Condensed Matter* **2008**, 403, 1863.

[14] S. H. Lee, B. J. Kang, J. S. Kim, B. W. Yoo, J. H. Jeong, K. H. Lee, M. Jazbinsek, J. W. Kim, H. Yun, J. Kim, Y. S. Lee, F. Rotermund, O.-P. Kwon, *Adv. Opt. Mater.* **2015**, 3, 756.

[15] Z. Yang, L. Mutter, M. Stillhart, B. Ruiz, S. Aravazhi, M. Jazbinsek, A. Schneider, V. Gramlich, P. Günter, *Adv. Funct. Mater.* **2007**, 17, 2018.

[16] G. A. Valdivia-Berroeta, L. K. Heki, E. A. McMurray, L. A. Foote, S. H. Nazari, L. Y. Serafin, S. J. Smith, D. J. Michaelis, J. A. Johnson, *Adv. Opt. Mater.* **2018**, 1800383.

[17] S. H. Lee, B. J. Kang, B. W. Yoo, S. C. Lee, S. J. Lee, M. Jazbinsek, H. Yun, F. Rotermund, O. P. Kwon, *Adv. Funct. Mater.* **2017**, 27, 1605583.

[18] Z. Sun, X. Liu, X. Wang, L. Li, X. Shi, S. Li, C. Ji, J. Luo, M. Hong, *Crystal Growth & Design* **2012**, 12, 6181.

[19] H. Chen, Q. Ma, Y. Zhou, Z. Yang, M. Jazbinsek, Y. Bian, N. Ye, D. Wang, H. Cao, W. He, *Cryst. Growth Des.* **2015**, 15, 5560.

[20] B. J. Coe, S. P. Foxon, E. C. Harper, J. A. Harris, M. Helliwell, J. Raftery, I. Asselberghs, K. Clays, E. Franz, B. S. Brunschwig, A. G. Fitch, *Dyes Pigm.* **2009**, 82, 171.

[21] J.-H. Jeong, B.-J. Kang, J.-S. Kim, M. Jazbinsek, S.-H. Lee, S.-C. Lee, I.-H. Baek, H. Yun, J. Kim, Y. S. Lee, J.-H. Lee, J.-H. Kim, F. Rotermund, O.-P. Kwon, *Sci. Rep.* **2013**, 3.

[22] C. Vicario, B. Monoszlai, C. P. Hauri, *Physical Review Letters* **2014**, 112, 213901.

[23] T. D. Dorney, R. G. Baraniuk, D. M. Mittleman, *JOSA A* **2001**, 18, 1562.

[24] L. Mutter, F. D. Brunner, Z. Yang, M. Jazbinšek, P. Günter, *JOSA B* **2007**, 24, 2556.

# Chapter 4 Designing non-centrosymmetric molecular crystals: optimal packing may be just one carbon away

## 4.1 Overview

Molecular non-linear optical (NLO) crystals feature important advantages compared to inorganic counterparts, such as low dielectric constants, ultrafast response times, and large electro-optic coefficients. Conjugated push-pull chromophores connecting electron donating with electron accepting groups are often employed in the design of these crystals. However, the large molecular dipole moments associated with these molecules induce antiparallel or centrosymmetric conformations in the solid state, resulting in NLO inactivity. In this chapter, we combine the cation-anion hydrogen bond interactions of a hydroxy piperidino electron donor group with increased Van der Waals volume effects induced by an ethyl modification of the electron accepting moiety to produce non-centrosymmetric packing in the organic salt EHPSI-4NBS. Converting a methyl into an ethyl group was sufficient to completely change the packing symmetry in the molecular crystal and switch on NLO activity. We attribute this behavior to the increased size of the ethyl group, which serves to push apart the Van der Waals contacts of the cation that lead to centrosymmetric packing in the methyl derivative (HPSI-4NBS). To test the applicability of EHPSI-4NBS as a NLO material, THz generation experiments were performed at 1200 nm pump wavelength. Spectral amplitude similar to state-of-the-art DAST crystal was observed with improved generation profile from 0 to 3.8 THz. The following work was published in Advanced Functional Materials, 30(3), 1904786.

## 4.2 Introduction

Non-centrosymmetric molecular crystals are highly desirable for non-linear optical (NLO) applications[1] such as THz[2] and second harmonic generation.[3] Organic NLO materials often feature a low dielectric constant,[4] an ultrafast electro-optical response time,[5] and large molecular hyperpolarizability.[6, 7] The first hyperpolarizability (β) is an important molecular characteristic that is directly related to the magnitude of the second order nonlinear susceptibility ($\chi2$).[8] In order to optimize β, push-pull π-conjugated molecules with large dipole moments are utilized in the design of organic NLO materials.[9, 10] **Figure 4.1** shows a general strategy to design these chromophores using different electron donor (ED) and acceptor (EA) groups connected by a styryl bridge. Unfortunately, the large magnitude of the molecular dipole moment increases the tendency of the chromophores to pack in a centrosymmetric fashion.[11, 12] This centrosymmetric alignment of molecules within a crystal causes the macroscopic second order NLO response to cancel to zero.

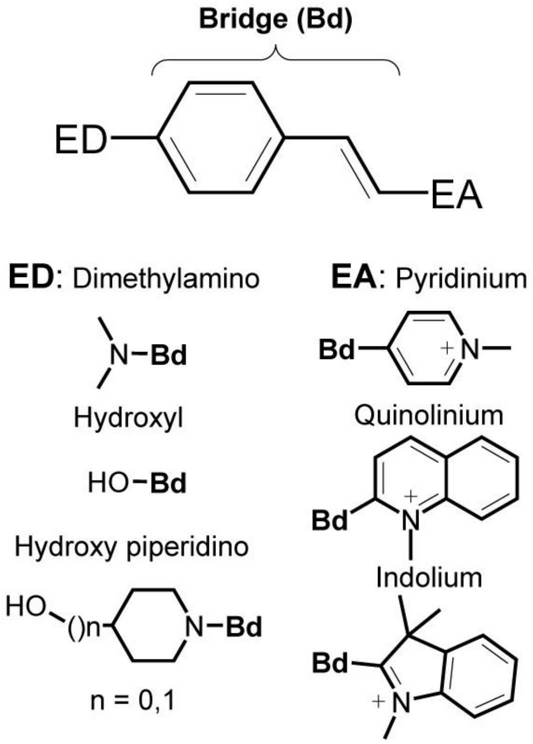

**Figure 4.1** Push pull chromophores with different electron donating (ED) and accepting (EA) groups.

A proven approach to obtain non-centrosymmetric molecular packing is to synthesize organic salts that pair a highly conjugated cation with different anions. Unique anion structures promote different intermolecular interactions with the cation and therefore can lead to non-centrosymmetry within the crystal.[7, 13] This situation is observed with the widely used cation DAS ((E)-4-(4-(dimethylamino)styryl)-1-methylpyridin-1-ium), which features centro- and non-centrosymmetric crystal arrangements depending on the accompanying anion.[14] In our previous work, we observed the same tendency to form both centro- and non-centrosymmetric crystals with alkynyl-based pyridinium cations.[10] However, other favorable cations have not crystallized in a non-centrosymmetric fashion, even when several different anions were tested.[15]

Another conventional approach to promote head-to-tail conformations is to use hydrogen bond donors and acceptors on opposite sides of the chromophores.[11, 16] This strategy is illustrated by comparing the centrosymmetric compound DAQ-T[17] (2-(4-(N,N-dimethylamino)styryl)-1-methylquinolinium 4-methylbenzenesulfonate), featuring a dimethylamino electron donating group and a quinolinium accepting group, with non-centrosymmetric OHQ-T[11] (2-(2-(4-Hydroxyphenyl)vinyl)-1-methylquinolinium 4-methylbenzenesulfonate), possessing a hydroxyl group in in place of the dimethylamino moiety in DAQ-T(see diagrams of donor and acceptor groups in **Figure 4.1**). Unfortunately, this electron donor group exchange from the DAQ to the OHQ cations decreases β, and therefore reduces its efficiency for NLO potential applications.

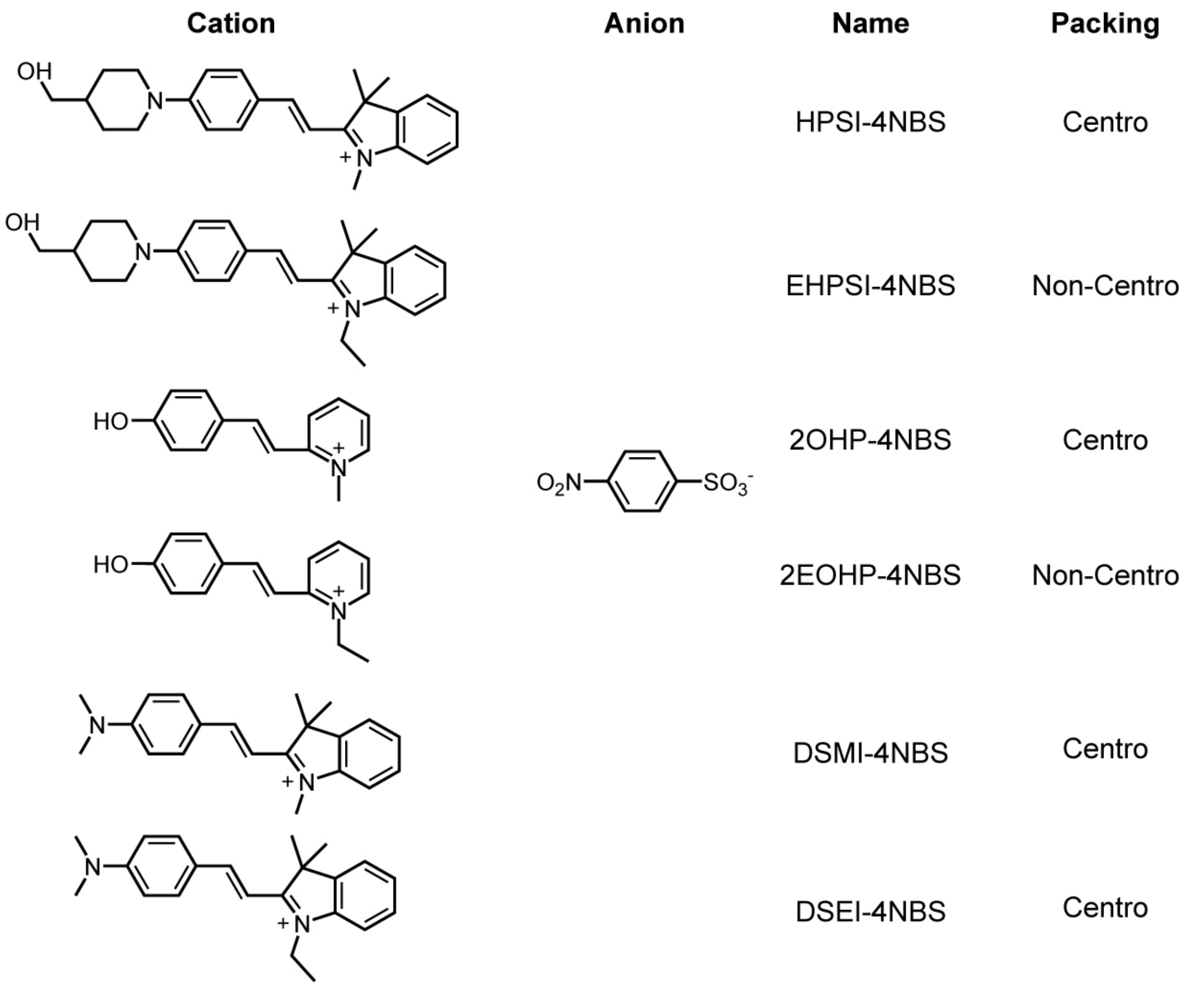

**Figure 4.2** Molecular structures of molecular cations combined with 4NBS anion. HPSI and EHPSI feature a hydroxy piperidino donating group, DSMI and DSEI contain a dimethylamino moiety, OHP and EOHP feature a hydroxyl group. Methyl and ethyl substitutions were introduced to evaluate their impact on centrosymmetric (Centro) versus non-centrosymmetric (Non-Centro) molecular packing.

To overcome the drop in hyperpolarizability associated with changing an amino donating group to a hydrogen bonding one, Lee et al. introduced hydroxy piperidino groups able to induce non-centrosymmetric arrangements without significantly affecting the molecular hyperpolarizability.[18] These alcohol-containing groups enable hydrogen-bonding interactions between the cation and the sulfonate anion. So far, the same research group has reported two new non-centrosymmetric NLO crystals using this approach.[19] However, to the best of our knowledge, no alternate strategies have been reported addressing the situation when the hydroxy piperidino groups fail to produce acentric molecular conformations.

In this chapter, we introduce an alternative approach to induce non-centrosymmetric packing based on slightly increasing the Van der Walls volumes of molecular cations. In order to achieve this, a methyl to ethyl substitution was performed on the quaternary nitrogen of an indol-1-ium cation. To favor hydrogen bond networking, the hydroxy piperidino group piperidin-4-ylmethanol was utilized as an electron donating group. **Figure 4.2** shows the compounds designed using this strategy: Methyl substituted HPSI-4NBS ((E)-2-(4-(4-(hydroxymethyl)piperidin-1-yl)styryl)-1,3,3-trimethyl-3H-indol-1-ium 4-nitrobenzenesulfonate) and ethyl substituted EHPSI-4NBS ((E)-1-ethyl-2-(4-(4-(hydroxymethyl)piperidin-1-yl)styryl)-3,3-dimethyl-3H-indol-1-ium 4-nitrobenzenesulfonate). Both compounds feature a piperidin-4-ylmethanol electron donating group and an indol-1-ium acceptor group. The indol-1-ium acceptor group differs from the commonly used quinolinium[11, 20] and pyridinium[21] moieties present in HMQ-TMS and DAST respectively (**Figure 4.1**).

Unlike previously reported molecules with the piperidin-4-ylmethanol electron donating group, HPSI-4NBS crystallizes in a centrosymmetric space group.[18, 19] However, we demonstrate in this work that when we introduce an ethyl group in the indol-1-ium nitrogen, then EHPSI packs in a non-centrosymmetric space group with perfect alignment for NLO applications. To further analyze the role of the ethyl substitution as a non-centrosymmetry promoter, cations with dimethylamino and hydroxyl electron donating groups were also studied and their molecular structures are shown in **Figure 4.2**. The dimethylamino methyl substituted DSMI-4NBS ((E)-2-(4-(dimethylamino)styryl)-1,3,3-trimethyl-3H-indol-1-ium 4-nitrobenzenesulfonate 4-nitrobenzenesulfonate) and ethyl substituted DSEI 4NBS ((E)-2-(4-(dimethylamino)styryl)-1-ethyl-3,3-dimethyl-3H-indol-1-ium 4-nitrobenzenesulfonate) both exhibit centrosymmetric packing. On the other hand, the ethyl substituted hydroxyl pyridinium chromophore 2EOHP-4NBS ((E)-1-ethyl-2-(4-hydroxystyryl)pyridin-1-ium) shows non-centrosymmetric packing compared with the centric conformation observed in the methyl substituted 2OHP-4NBS ((E)-2-(4-hydroxystyryl)-1-methylpyridin-1-ium 4-nitrobenzenesulfonate). These findings highlight the synergistic effect between the ethyl-methyl substitution and the hydrogen bond donor nature of the piperidin-4-ylmethanol and hydroxyl groups in EHPSI-4NBS and 2EOHP-4NBS, respectively. We propose that the ethyl-methyl substitution at the quaternary nitrogen of the organic salts in conjunction with hydrogen bond donor groups can be used as part of a multi-component approach to generating non-centrosymmetric molecular packing.

To assess the applicability of EHPSI-4NBS as a NLO material, we tested THz generation by optical rectification of ultrafast infrared pulses passed through the molecular crystal. These THz generation data were compared with data measured from DAST and gallium phosphide (GaP) crystals.

## 4.3 Results and discussion

### 4.3.1 Chromophores design and crystal structure analysis.

In order to evaluate the potential of the indolium ring as an acceptor group for NLO applications, DSMI-4NBS was synthesized and crystallized. The dimethylamino electron-donating group was chosen initially for the new chromophore due to its favorable electron-donating capabilities and ease of synthesis. However, this compound crystallizes in the P21/c centrosymmetric group. Therefore, in order to induce non-centrosymmetry, the piperidin-4-ylmethanol group was employed in lieu of the dimethylamino group (**Figure 4.2**). The resulting compound, HPSI-4NBS, was crystallized and X-ray diffraction data were collected. Surprisingly, the molecule crystallizes in a centrosymmetric arrangement (**Figure 4.3a**). In analyzing the crystal structure of HPSI-4NBS, we observed strong hydrogen bonding interactions between the OH group in the piperidin-4-ylmethanol moiety of the cation with the sulfonyl group of the anion (**Figure 4.3a**). This interaction has also been observed in other hydroxy piperidino salts,[18, 19] so we hypothesized that short-distance Van der Waals contacts are also adding to the overall packing in the crystal to help produce the antiparallel conformation of the cations. In order to increase the packing space between molecules in the crystals and thus hopefully obtain an acentric arrangement, we designed EHPSI-4NBS. This molecule features an ethyl group attached to the indol-1-ium nitrogen instead of the methyl group in HPSI-4NBS (**Figure 4.2**), which we believed would push the two molecules farther apart and reduce dipole-dipole interactions.[18, 22] Indeed, X-ray diffraction analysis of EHPSI-4NBS shows non-centrosymmetric packing with perfect alignment for NLO applications. **Figure 4.3** compares the molecular packing of HPSI-4NBS and EHPSI-4NBS. Arrows were drawn from the electron donating to the electron accepting groups to help differentiate between the centro- and non-centrosymmetric arrangements.

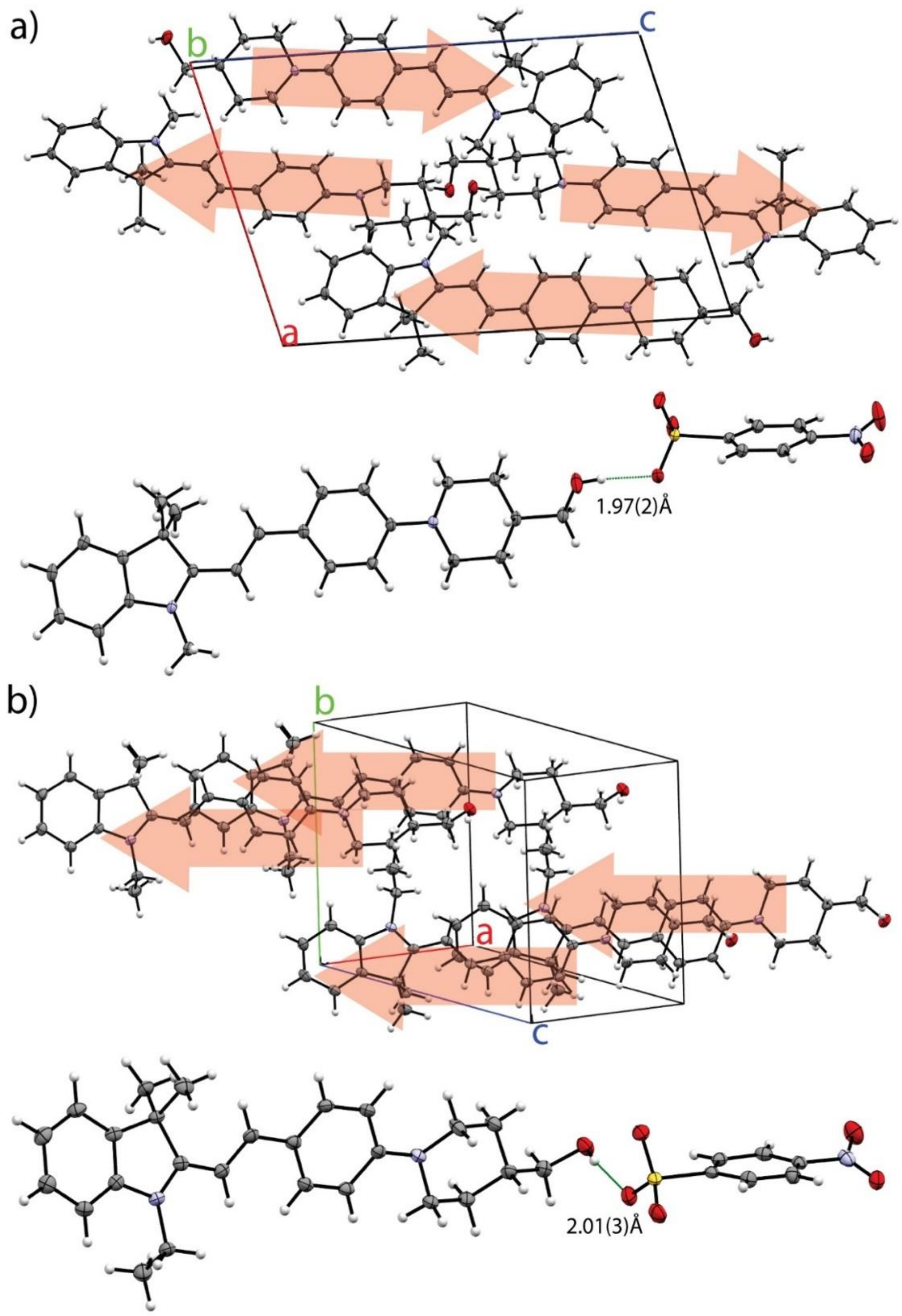

**Figure 4.3** a) Crystal structure and sulfonate-hydroxy hydrogen bond distances of a) centrosymmetric HPSI-4NBS, and b) acentric EHPSI-4NBS. Arrows indicate the antiparallel (centrosymmetric) and parallel (non-centrosymmetric) conformations of HPSI-4NBS and EHPSI-4NBS, respectively.

As observed in **Figure 4.3**, similar hydrogen bond distances are present in HPSI-4NBS and EHPSI-4NBS (1.97 and 2.01 Å, respectively). To further analyze the effect of the hydrogen bond networking induced by the piperidin-4-ylmethanol group, Hirshfeld surfaces[23] were generated for HPSI-4NBS and EHPSI-4NBS. In order to trace these surfaces, di and de are defined as the minimum distance between the surface and an atom inside and outside the surface, respectively.

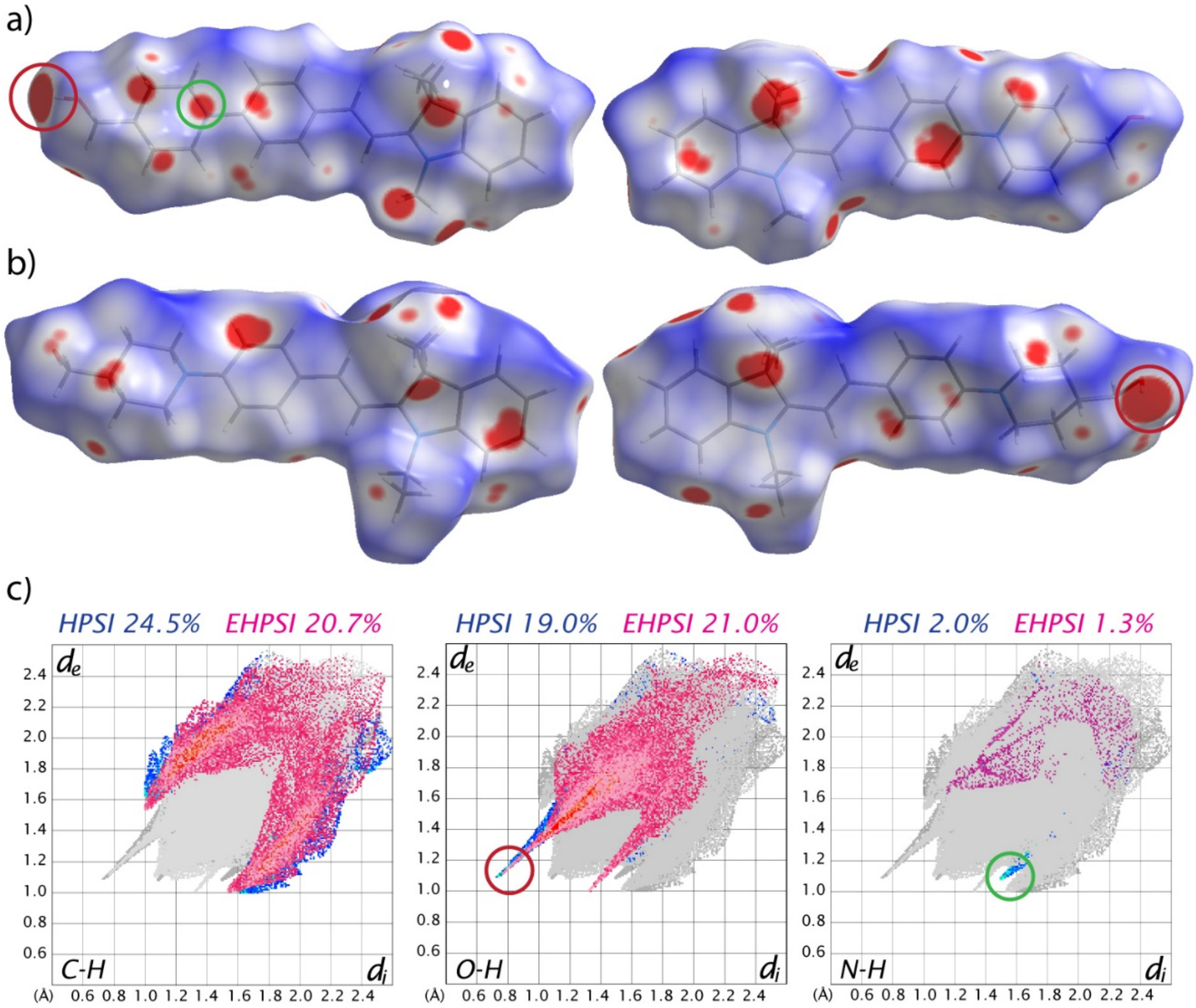

**Figure 4.4** Hirshfeld surfaces and fingerprint plots for HPSI and EHPSI, a) HPSI Hirshfeld surface, b) EPHSI Hirshfeld surface, and c) fingerprint plots for C-H, O-H, and N-H intermolecular interactions. Red and blue spots in the surfaces indicate close and distant contacts, respectively.

The surfaces shown in **Figure 4.4** were obtained with respect to $d_{norm}$ to correct the interactions by the atomic Van der Waals volumes. As displayed in **Figure 4.4a** and b, HPSI shows a higher number of close contacts compared to EHPSI, especially in the face region of the surface. **Figure 4.4c** shows the fingerprint plot of O-H intermolecular interactions for HPSI and EHPSI cations. Similar results are observed, being the anion sulfonate - cation hydroxyl the strongest interaction found as it is indicated by the largest red spot in **Figures 4.4a** and b (marked in red). The O-H fingerprint plot shown in **Figure 4.4c** support this observation by displaying closest contacts values at ~1.1 Å in de and 0.75 Å in di (marked in red). Additionally, the ethylated chromophore features overall longer interaction distances compared with the methylated counterpart. This same trend is appreciated in the fingerprint plots corresponding to C-H intermolecular interactions, where both cations feature similar coverage but EHPSI extends its interactions to longer distances. An unprecedented strong interaction in the piperidin-4-ylmethanol nitrogen is observed in the HPSI cation, as shown in in **Figure 4.4a**.[18] This same interaction is appreciated in the N-H fingerprint plot in **Figure 4.4c** and it is indicated by a local minimum at 1.1 Å in de and 1.5 Å in di (marked in green).

To confirm that the overall longer distances observed in EHPSI Hirshfeld analysis compared with HPSI are due to the addition of one more carbon in the quaternary cation nitrogen moiety, important cation-cation interaction distances are characterized in **Figure 4.5**. A distinguishable shift in cation packing is observed for EHPSI-4NBS with respect to HPSI-4NBS. This is confirmed by the significant increase in centroid-centroid cation distances, denoted by dashed green lines, from 4.79 Å in HPSI to 7.60 Å in EHPSI. A closer inspection to **Figure 4.5b** reveals the inducing role of the ethyl group in the shifted conformation of EHPSI-4NBS. Even with the shifted molecular packing in EHPSI-4NBS, the methyl indolium to bridging benzene ring distances are slightly increased from 3.45 to 3.81 Å in EHPSI with respect to HPSI. Face to edge interactions with anions were also analyzed to evaluate a possible impact on the induced non-centrosymmetric molecular packing. **Figure 4.10** in the Supporting Information shows the generated Hirshfeld surfaces and fingerprint plots for the 4NBS anions paired with both cations. Significant differences were not found in the obtained results, and therefore we propose that the main cause of the drastic change on molecular packing is directly related to the increased Van der Waals volume of the ethyl group. This induces the shifted arrangement shown in **Figure 4.5b** and reduces the dipole-dipole interactions as it was found in the Hirshfeld analysis. To confirm the impact of the ethyl shifting effect on molecular packing, we obtained crystal structures of 2OHP-4NBS and 2EOHP-4NBS. As shown in the middle of **Figure 4.2**, these chromophores feature a hydroxyl electron donating group and methyl and ethyl groups in the pyridinium quaternary nitrogen, respectively. Despite the different orientation of the ethyl group in 2EOHP-4NBS compared with EHPSI-4NBS, as observed in **Figure 4.5c** and d, the same shifting effect is observed with the ethyl substitution. As illustrated in **Figure 4.11-4.12**, Hirshfeld analysis of 2EOHP-4NBS shows overall longer interaction distances compared with 2OHP-4NBS similar to what was observed in EHPSI-4NBS and HPSI-4NBS.

In order to explore the applicability of the ethyl-methyl substitution as a NLO molecular crystals design strategy to non-hydrogen bonding electron donating groups, DSEI-4NBS (**Figure 4.1**), was synthesized and crystallized. XRD analysis shows a centrosymmetric space group for this chromophore (See **Figure 4.9** in the Supporting Information). Therefore, we propose that the ethyl-methyl substitution does not introduce, in this case, a high enough shifting effect to result in non-centrosymmetric arrangements. However, the synergistic behavior between the hydrogen bond donor groups and the ethyl substitution in EHPSI and 2EOHP is able to induce acentric packing.

### 4.3.2 Linear and nonlinear optical properties

To evaluate the impact of the ethyl-methyl substitution on $\chi(2)$,[8] molecular hyperpolarizability ($\beta$) values, order parameters and number densities were calculated and compared for HPSI-4NBS and EHPSI-4NBS. To estimate $\beta$, DFT calculations were carried out using the obtained X-ray coordinates as a starting point.[24] Equations 4.1 and 4.2 in the supplementary information were employed to calculate this parameter. The $\beta$exp values for HPSI and EHPSI-4NBS are 132 x 10-30 esu and 123 x 10-30 esu, respectively. The difference corresponds to a 9% drop-off for the methyl to ethyl substitution. As shown in **Figure 4.6d**, the order parameter (cos3$\sigma$p) of EHPSI-4NBS was estimated by measuring the angle between the molecular hyperpolarizability and the *a* crystallographic axis. A $\theta$p value of 2.5° and an order parameter of 1.0 were obtained for EHPSI, which represents perfect alignment for NLO applications, while centrosymmetric HPSI features an order parameter of 0. The number density values are 1.44 nm-3 for HPSI-4NBS and 1.37 nm-3 for EHPSI-4NBS, which represents a 6% decrease in density with ethyl substitution. Thus, the drastic improvement in order parameter with the ethyl substitution far outweighs the small decrease in hyperpolarizability and number density. Additionally, in previous studies from Okada et al,[25] only a small reduction in melting point, around 7%, was observed for the methyl-ethyl substitution in stilbazolium derivatives.

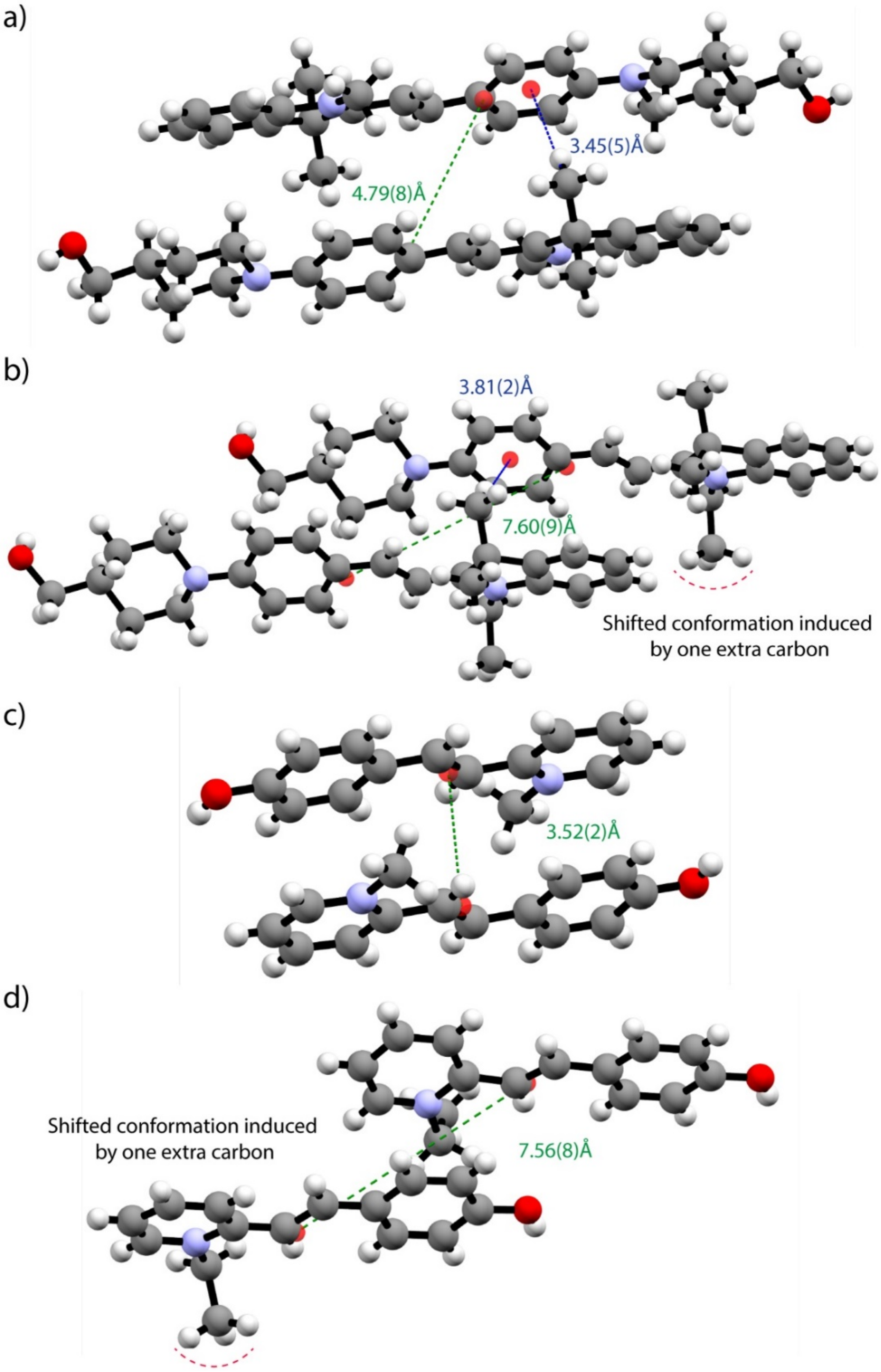

**Figure 4.5** a) HPSI-4NBS, b) EHPSI-4NBS, c) 2OHP-4NBS, and d) 2EOHP-4NBS cation-cation distances characterization. Centroid-centroid distances are displayed with dashed green lines, while methyl indolium to benzene ring distances are shown with dashed blue lines.

**Figure 4.6a** shows the UV-Vis absorption spectra in methanol solution for HPSI-4NBS and EHPSI-4NBS. Maximum absorption wavelengths were found at 552 and 549 nm for HPSI-4NBS and EHPSI-4NBS, respectively. These results are in agreement with the nonlinearity-transparency trade off rule that establishes a direct relationship between the hyperpolarizability and the wavelength of maximum absorption.[12] The maximum absorption values are well below near-infrared pumping wavelengths (800 to 1600 nm) employed in THz generation experiments. However, two photon absorption could cause crystal damage for samples pumped below 1200 nm, indicating that pumping EHPSI-4NBS with 1200 – 1600 nm wavelengths will likely be preferred for high-field THz applications.

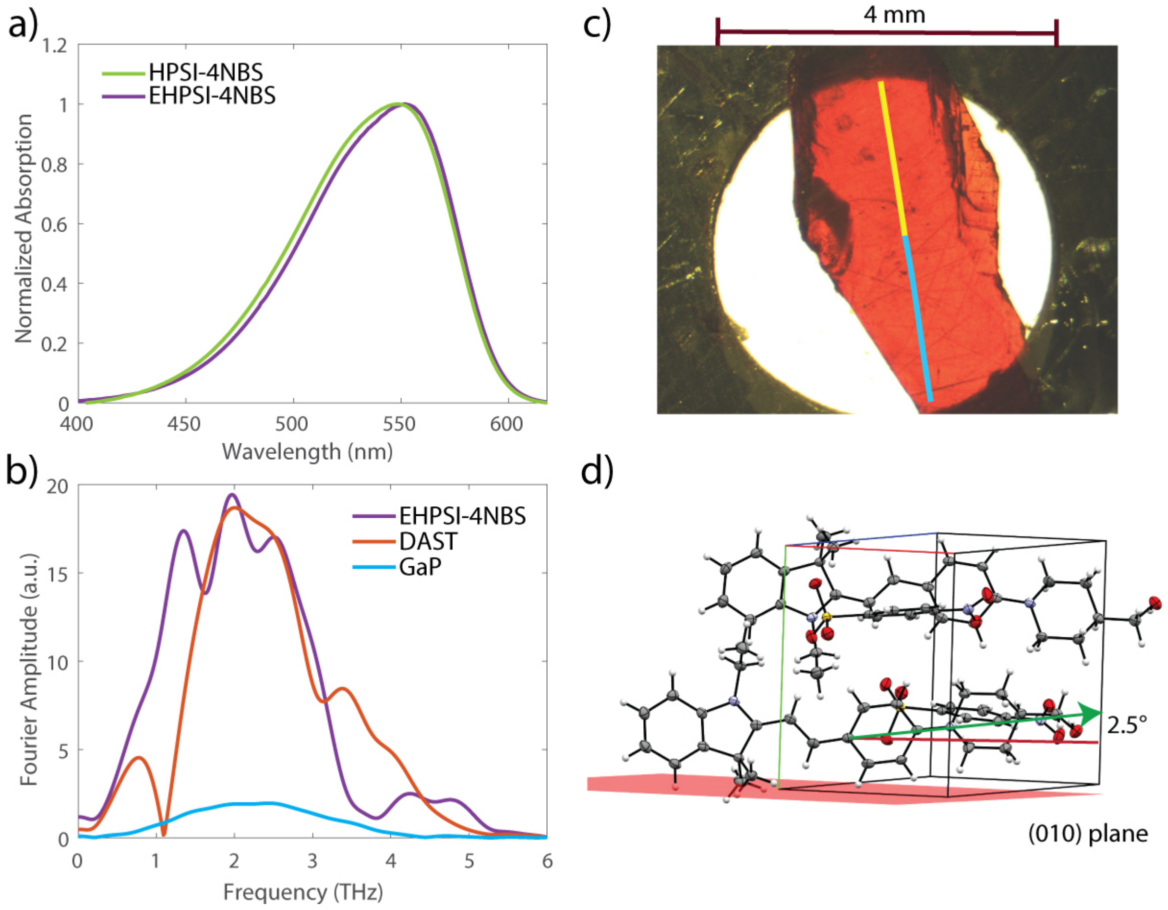

**Figure 4.6** a) UV-Vis absorption spectra for HPSI-4NBS (green) and EHPSI-4NBS (purple). b) THz generation spectrum for EHPSI-4NBS (purple), DAST (orange) and GaP (light blue). c) Image of the 380 μm thick EHPSI-4NBS crystal employed in THz generation experiments. The polar and THz generation axis are indicated by yellow and cyan lines, respectively. d) Angle between the molecular hyperpolarizability (green line) and the polar axis (red line).

To test the ability of EHPSI-4NBS as NLO material, a 5 x 2 x 0.38 mm3 crystal (**Figure 4.6c**) was mounted in a 4 mm diameter aperture and tested for THz generation. The main crystal face was determined to be (010), which is ideal for THz generation. Furthermore, the polar and generation axis in EHPSI-4NBS crystal are parallel with respect to each other. Generation comparisons were established with 340 μm thick DAST and 300 μm thick GaP crystals by illuminating the same area with 1200 nm infrared light. Additional details about the THz generation setup are provided in the methods section and the Supporting Information. **Figure 4.6b** shows the obtained spectra, broadband generation from 0 to 3.8 THz with EHPSI-4NBS is observed with a maximum spectral amplitude corresponding to ~10 times that of GaP.[26] Similar amplitude is observed when compared with DAST, however the absence of important generation dips in the 0 to 3.8 THz range makes EHPSI-4NBS a promising candidate for THz generation.

## 4.4 Conclusions

The opportunity to utilize increased Van der Waals volumes to induce optimal molecular packing has been discussed and demonstrated by modifying a methyl group to an ethyl group on a quaternary nitrogen of the indolium and pyridinium cores. In the EHPSI-4NBS and 2EOHP-4NBS systems studied, a synergistic effect between the added ethyl group and the hydroxyl groups results in perfect alignment for NLO applications, such as THz generation. Thus, when designing molecular crystals for NLO applications, it is important to remember that small variations in molecular structure can make a big difference in properties; optimal packing may be just one carbon away.

## 4.5 Experimental section

### 4.5.1 Synthesis and characterization

The synthetic pathway to obtain the organic salts is depicted in **Figure 4.7** in the Supporting Information. For HPSI and EHPSI cation precursors synthesis, 4-(4-(hydroxymethyl)piperidin-1-yl)benzaldehyde was synthesized using an aromatic substitution reaction between 4-fluoro benzaldehyde and piperidin-4-ylmethanol as was reported elsewhere.[18] To obtain DSMI and DSEI, commercially available 4-dimethylamino benzaldehyde was utilized. In the final stage of the cation precursors synthesis, the different 4-substituted benzaldehydes were condensed with 1,3,3-trimethylindolenine using methane sulfonic acid (MSA) as the catalyst.[27] Finally, the anion was added by reacting the coupled product with methyl and ethyl 4-nitrobenzenesulfonate in toluene at reflux. 2OHP-4NBS and 2EOHP-4NBS were synthesized using condensation reactions similar to other organic THz generating molecules.

Synthesis procedure details, NMR and X-ray diffraction data for the synthesized compounds is available in the Supporting Information.

### 4.5.2 Hirshfeld surface analysis.

Hirshfeld analysis was performed using the CrystalExplorer software.[23] The analyses were performed calculating a surface around a cation and an anion molecule separately, and then the interactions with the surrounding molecules were studied. Using this approach, $d_{norm}$ surfaces and di-de plots were obtained, where di represents the distance between an atom inside the surface and the closest point in the surface, and de is defined similarly but with an atom outside of the surface.

### 4.5.3 Optical characterization and THz generation experiments

For UV-Vis absorption measurements, HPSI-4NBS and EHPSI-4NBS samples were dissolved in methanol and transferred to a 1-cm path length fused-quartz cell. Absorption data was recorded from 400 to 700 nm using a Cary 5e spectrometer.

The optical rectification THz generation setup consisted of 800-nm light obtained from an amplified Ti:sapphire laser which was converted in an optical parametric amplifier to 1200 nm. The beam diameter of the IR light was ~7.6 mm with pulse duration of ~100 fs and 0.7 μJ per pulse. Crystal polar axis and pump pulse polarization were both vertical. Excess IR was removed using a 1-mm thick Teflon filter. Generated THz then passed through a vertical polarizer, and a single off-axis parabolic mirror was used to collect and focus the THz radiation to a GaP electro-optic crystal composed of a 100 μm [110] layer bonded to a 1 mm [100] layer (**Figure 4.13**). The THz waveforms were measured by electro-optic sampling with ~100 fs

800-nm light pulses.[28] The probe pulse traveled along a delay stage such that the relative timing of the pump and probe pulses could be varied and temporal waveforms obtained. The detection bandwidth, with the current setup, is restricted to less than 6 THz.

## 4.6 General and Supporting Information

### 4.6.1 Organic salts characterization

#### *4.6.1.1 Synthesis and H-NMR analysis*

The aldehyde compound **1b** was obtained using the reaction proposed by Lee et al.[1] 4-Fluorobenzaldehyde (1eq), 4-piperidinemethanol (1.5 eq), and $K_2CO_3$ (1.5 eq) were combined in dry DMF and the reaction was stirred at 70°C for 48 hours. The DMF solvent was removed by evaporation under vacuum and the residue was dried in a high vacuum oven at 80°C for 24 hours. The obtained solids were extracted with water and DCM and **1b** was purified by column chromatography (hexane/ethyl acetate (1:1)). Yield, 58%.

The compounds **3a** and **3b** were synthesized using an acidic condensation reaction between **1a,b** (1.4 eq) and **2** (1 eq) with methanesulfonic acid (MSA, 0.375 eq) as catalyst.[2] The reaction was refluxed in dry methanol for 48 hours, then the mixture was neutralized with $Na_2CO_3$ solution and the resulting solids were extracted with DCM. The crude product was concentrated in vacuo and purified by column chromatography (hexane/ethyl acetate (6:1)). Yields: **3a**, 28%; **3b**, 24%.

The final organic salt products (**4aM**, **4aE**, **4bM**, and **4bE**) were obtained by alkylation reaction of the condensed products **3a** and **3b** (1 eq) with ethyl and methyl 4-nitrobenzenesulfonate (1.5 eq). The reaction mixture was stirred in toluene at 85°C for 8h and the final products were recovered by filtration. Yield, 95%.

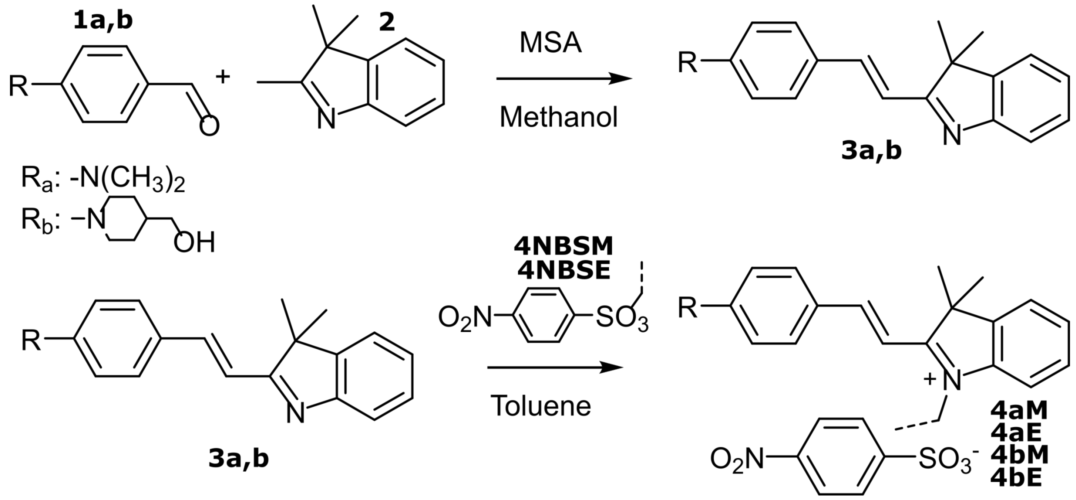

**Figure 4.7** Synthesis of DSMI-4NBS (4aM), DSEI-4NBS (4aE) HPSI-4NBS (4bM) and EHPSI-4NBS (4bE)

Pyridinium salts 2OHP-4NBS and 2EOHP-4NBS were condensed by condensation reaction in presence of piperidine as it has been reported previously for several THz generating organic salts.[3] Herein, the synthesis of 2OHP-4NBS is explained as representative for both pyridinium compounds. The anion precursor, methyl 4-nitrobenzenesulfonate (1 eq) was combined with 2-picoline (2eq) in presence of toluene at 80°C for 3 hours. The product was recovered by filtration and washed several times with toluene. The purified product obtained in this way was stirred in methanol with 4-hydroxybenzaldehyde (1 eq) in presence of piperidine catalyst (0.2 eq) at room temperature for 2 days. The final organic salt product was collected by filtration and purified by recrystallization in methanol. Yield 63%.

NMR data were collected for **3b**, DSMI-4NBS, DSEI-4NBS, HPSI-4NBS, EHPSI-4NBS, 2OHP-4NBS, and 2EOHP-4NBS using an INOVA 500 MHz Spectrometer. All of the measurements were performed in DMSO-d6 and the shifts are reported with respect to TMS.

(E)-(1-(4-(2-(3,3-dimethyl-3H-indol-2-yl)vinyl)phenyl)piperidin-4-yl)methanol (**3b**) δ: 7.649-7.584 (m, 3H), 7.451 (d, J: 7.58 Hz, 1H), 7.422 (d, J: 7.34 Hz, 1H), 7.275 (t, J: 7.5 Hz, 1H), 7.163 (t, J: 7.34 Hz, 1H), 7.009-6.942 (m, 3H), 4.488 (s, 1H), 3.858 (d, J: 12.72 Hz, 2H), 3.273 (t, J: 5.75 Hz, 2H), 2.743 (dt, J1: 1.47 Hz, J2: 10.9 Hz, 2H), 2.630-2.610 (m, 1H), 1.374 (s, 6H) 1.732 (d, J: 11.62 Hz, 2H), 1.374-1.158 (dq, J1: 4 Hz, J2: 12.71 Hz, 2H).

(E)-2-(4-(dimethylamino)styryl)-1,3,3-trimethyl-3H-indol-1-ium 4-nitrobenzenesulfonate 4-nitrobenzenesulfonate (**DSMI-4NBS**) δ: 8.305 (d, 1H, J: 15.75 Hz), 8.192 (d, 2H, J: 8.79 Hz), 8.069 (d, 2H, J: 8.54 Hz), 7.824 (d, 2H, J: 8.79 Hz), 7.768 (d, 1H, J: 7.2 Hz), 7.698 (d, 1H, J: 8.05 Hz), 7.554 (d, 1H, J: 7.81 Hz), 7.509 (t, 1H, J: 20.63 Hz), 7.467 (t, 1H, J: 7.32 Hz), 7.257 (d, 1H, J: 15.74 Hz), 6.879 (d, 2H, J: 9.03 Hz), 3.959 (s, 3H), 3.329 (s, 6H), 1.741 (s, 6H).

(E)-2-(4-(dimethylamino)styryl)-1-ethyl-3,3-dimethyl-3H-indol-1-ium 4-nitrobenzenesulfonate (**DSEI-4NBS**) δ: 8.331 (d, 1H,J: 15.5 Hz), 8.190 (d, 2H, J: 8.8 Hz), 8.093 (d, 2H, 8.5 Hz), 7.822 (d, 2H, J: 8.8Hz), 7.781 (d, 1H, 7.22 Hz), 7.719 (d, 1H, J: 8.07 Hz), 7.545 (t, 1H, J: 7.46 Hz ), 7.474 (t, 1H, J: 7.34), 7.258 (d, 1H, J: 15.65 Hz), 6.881 (d, 2H, 9.05 Hz), 4.529 (q, 2H, 7.46 Hz), 3.164 (s, 6H), 1.744 (s, 6H), 1.379 (t, 3H, J: 7.09 Hz).

(E)-1-ethyl-2-(4-(4-(hydroxymethyl)piperidin-1-yl)styryl)-3,3-dimethyl-3H-indol-1-ium 4-nitrobenzenesulfonate (**EHPSI-4NBS**) δ: 8.319-8.273 (m, 3H), 8.03 (d, J: 7.09 Hz, 2H), 7.930 (d, J: 8.80 Hz, 2H), 7.680 (d, J: 7.46 Hz, 2H), 7.640 (d, J: 7.95 Hz, 1H), 7.565 (t, J1: 7.45 Hz, J2: 7.83 Hz, 1H), 7.501 (t, J1: 7.46 Hz, J2: 7.46 Hz, 1H), 7.200 (d, J: 15.52 Hz, 1H), 7.065 (d, J: 9.05 Hz, 2H), 4.75 (s, 1H), 4.521 (q, J: 14.67 Hz, 2H), 4.230 (d, J: 13.44 Hz, 2H), 3.458 (d, J: 6.12 Hz, 2H), 3.356-3.311 (m, 6H), 3.115 (t, J1: 12.96 Hz, J2: 12.47 Hz, 2H), 1.899 (d, J: 13.45 Hz, 3H), 1.850 (s, 6H), 1.523 (t, J1: 7.22 Hz, J2: 7.33 Hz, 4H).

(E)-2-(4-(4-(hydroxymethyl)piperidin-1-yl)styryl)-1,3,3-trimethyl-3H-indol-1-ium 4-nitrobenzenesulfonate (**HPSI-4NBS**) δ: 8.302-8.269 (m, 3H), 8.031 (d, J: 8.68 Hz, 2H), 7.922 (d, J: 8.93 Hz, 2H), 7.668 (d, J: 7.46 Hz, 1H), 7.629 (d, J: 7.94 Hz, 1H), 7.568 (t, J1: 6.97 Hz, J2: 7.70 Hz, 1H), 7.507 (t, J1: 7.34 Hz, J2: 7.46 Hz, 1H), 7.231 (d, J: 15.53 Hz, 1H), 7.069 (d, J: 9.05 Hz, 1H), 4,762 (s, 1H), 4.231 (d, J: 13.33 Hz, 2H), 3.985 (s, 3H), 3.459 (d, J: 6.12 Hz, 2H), 3.357 (s, 1H), 3.109 (t, J1: 12.59 Hz, J2: 11.25 Hz, 2H) 2.021 (s, 1H), 1.890 (d, J: 13.45 Hz, 3H), 1.809 (s, 6H), 1.357-1.297 (m, 2H), 1.248 (t, J1: 7.21 Hz, J2: 7.09 Hz, 1H).

(E)-2-(4-hydroxystyryl)-1-methylpyridin-1-ium 4-nitrobenzenesulfonate (**2OHP-4NBS**) δ: 8.830 (d, J: 6.08 Hz, 1H), 8.489-8.402 (m, 2H), 8.213 (d, J: 8.86 Hz, 2H), 7.902 (d, J: 15.86 Hz, 1H), 7.856-7.793 (m, 3H), 7.733 (d, J: 8.57, 2H), 7.355 (d, J: 15.96, 1H), 6.884 (d, J: 8.57, 2H), 4.328 (s, 3H).

(E)-1-ethyl-2-(4-hydroxystyryl)pyridin-1-ium 4-nitrobenzenesulfonate (**2EOHP-4NBS**) δ: 8.856 (d, J: 6.08 Hz, 1H), 8.488-8.412 (m, 2H), 8.211 (d, 8.86 Hz, 2H), 7.912 (d, J:

15.96 Hz, 1H), 7.857-7.804 (m, 3H), 7.742 (d, J: 8.65 Hz, 2H), 7.343 (d, J: 15.82 Hz, 1H), 6.849 (d, J: 8.57 Hz, 2H), 4.758 (q, J: 6.95 Hz, 2H), 1.467 (t, J: 7.03 Hz, 3H).

#### *4.6.1.2 Crystallization and X-ray diffraction characterization.*

DSMI-4NBS, DSEI-4NBS, HPSI-4NBS, and EHPSI-4NBS were crystallized using slow evaporation from methanol to produce single crystals for X-ray diffraction experiments. High-resolution (0.84 Å) data were collected at 100 K using a MACH3 kappa goniometer and Cu $K_\alpha$ radiation from a FR591 rotating anode X-ray source. The resulting diffraction peaks were recorded with a Bruker Apex II CCD detector. The Bruker APEX3 software package was utilized to integrate, scale, and correct the data. The structure was solved using dual-space methods in SHELXT[4] and refined against $F^2$ on all data by full-matrix least squares with SHELXL-2014[5] using established refinement strategies.[6] Details of each crystal structure are summarized below.

**DSMI-4NBS:** *Crystal System*, monoclinic; *Space Group*, $P2_1/n$; *Point group*, 2/m; *a*, 12.6383(4) Å; *b*, 11.6171(4) Å; *c*, 19.9100(6) Å; *α*, 90°; *β*, 107.343(2)°; *γ*, 90°; *z*, 4; $R_1$, 0.0387; $wR_2$, 0.1000; *GOF*, 1.028; *CCDC*: 1911258. A disordered methanol solvent molecule was not modeled due to the presence of smeared residual density. This electron density was eliminated using Platon.[7]

**DSEI-4NBS:** *Crystal System*, monoclinic; *Space Group*, $P2_1/n$; *Point group*, 2/m; *a*, 9.6899(4) Å; *b*, 6.8098(3) Å; *c*, 41.962(2) Å; *α*, 90°; *β*, 90.947(3)°; *γ*, 90°; *z*, 4; $R_1$, 0.0555; $wR_2$, 0.1279; *GOF*, 1.146; *CCDC*: 1911257

**HPSI-4NBS:** *Crystal System*, triclinic; *Space Group*, P-1; *Point group*, -1; *a*, 11.5477(6) Å; *b*, 14.2796(8) Å; *c*, 17.6867(10) Å; *α*, 84.152(2)°; *β*, 74.312(2)°; *γ*, 80.795(2)°; *z*, 4; $R_1$, 0.0369; $wR_2$, 0.0985; *GOF*, 1.048; *CCDC*: 1867838

**EHPSI-4NBS (100K):** *Crystal System*, monoclinic; *Space Group*, Pn; *Point group*, m; *a*, 7.6089(4) Å; *b*, 9.9256(5) Å; *c*, 19.5064(9) Å; *α*, 90°; *β*, 96.738(2)°; *γ*, 90°; *z*, 2; $R_1$, 0.0256; $wR_2$, 0.0667; *GOF*, 1.027; *Flack Parameter*, 0.041(5); *CCDC*: 1867836.

**EHPSI-4NBS (298K):** *Crystal System*, monoclinic; *Space Group*, Pn; *Point group*, m; *α*, 7.51440(10) Å; *b*, 10.0391(2) Å; *c*, 20.1071(3) Å; *α*, 90°; *β*, 96.0920(10)°; *γ*, 90°; *z*, 2; $R_1$, 0.0380; $wR_2$, 0.1034; *GOF*, 1.045; *Flack Parameter*, 0.017(9); *CCDC*: 1947382.

**2OHP-4NBS (298K):** *Crystal System*, monoclinic; *Space Group*, P$2_1$/c; *Point group*, 2/m; *α*, 11.2729(2) Å; *b*, 21.5978(3) Å; *c*, 8.26710(10) Å; *α*, 90°; *β*, 111.1180(10)°; *γ*, 90°; *z*, 4; $R_1$, 0.0421; $wR_2$, 0.1104; *GOF*, 1.060; *CCDC*: 1956349.

**2EOHP-4NBS (298K):** *Crystal System*, monoclinic; *Space Group*, Cc; *Point group*, m; *α*, 14.6254(17) Å; *b*, 10.7062(13) Å; *c*, 13.0794(15) Å; *α*, 90°; *β*, 96.921(5)°; *γ*, 90°; *z*, 4; $R_1$, 0.0304; $wR_2$, 0.0835; *GOF*, 1.052; *Flack Parameter*, 0.007(10); *CCDC*: 1956350.

Additional powder X-ray diffraction experiments were performed to test the homogeneity of the EHPSI-4NBS samples after synthesis. As illustrated in **Figure 4.8**, the single crystal structure at 298K reported above is representative of the bulk material. Molecular packing of DSMI-4NBS and DSEI-4NBS are shown in **Figure 4.9.**

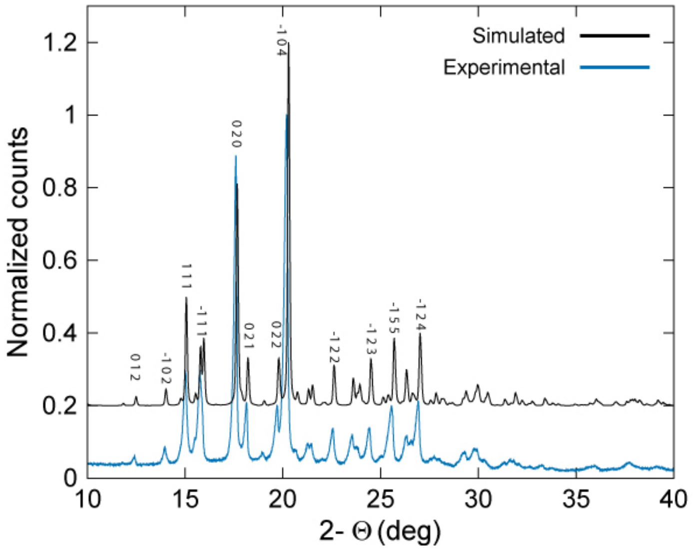

**Figure 4.8** Experimental (blue) and simulated (black) powder X-ray diffraction patterns for EHPSI-4NBS.

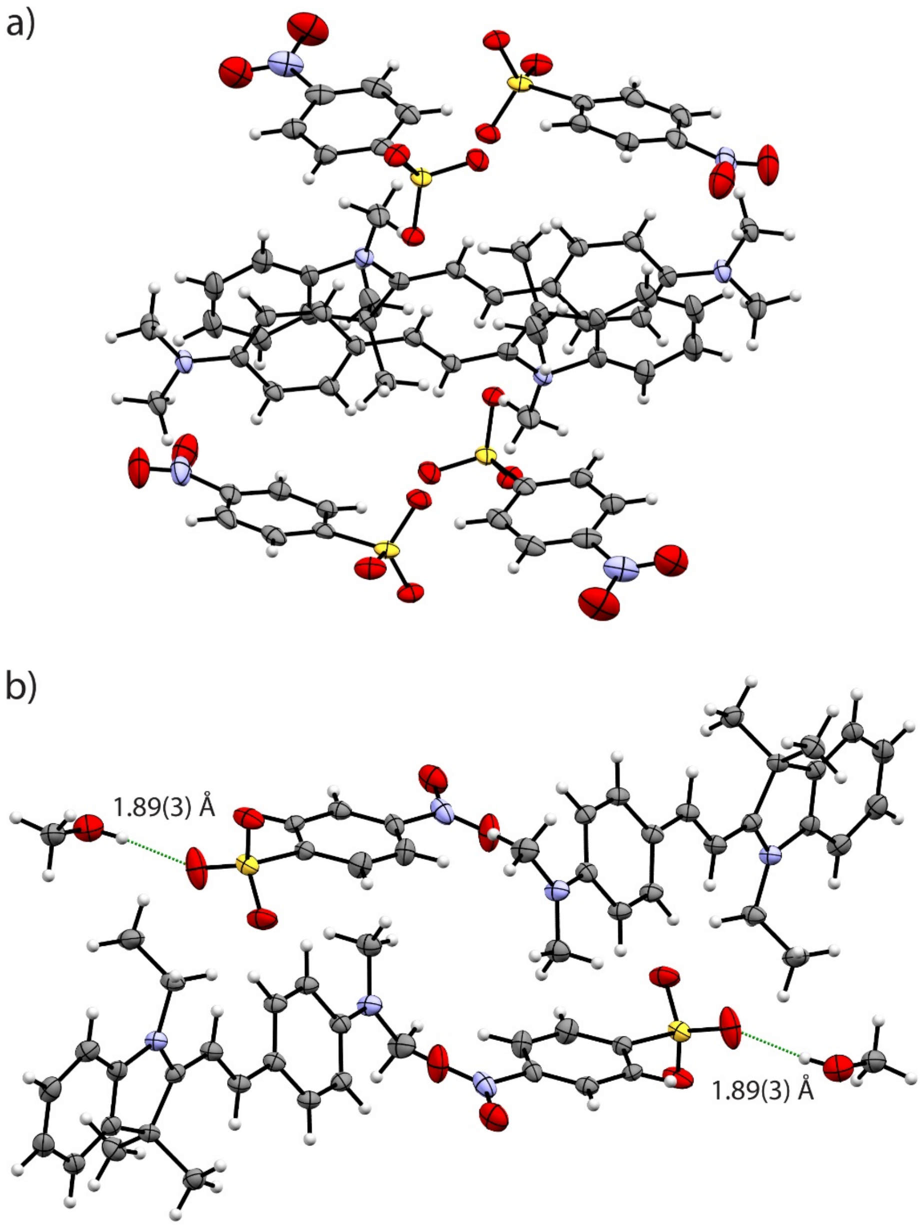

**Figure 4.9** Crystal structures of a) DSMI-4NBS and b) DSEI-4NBS.

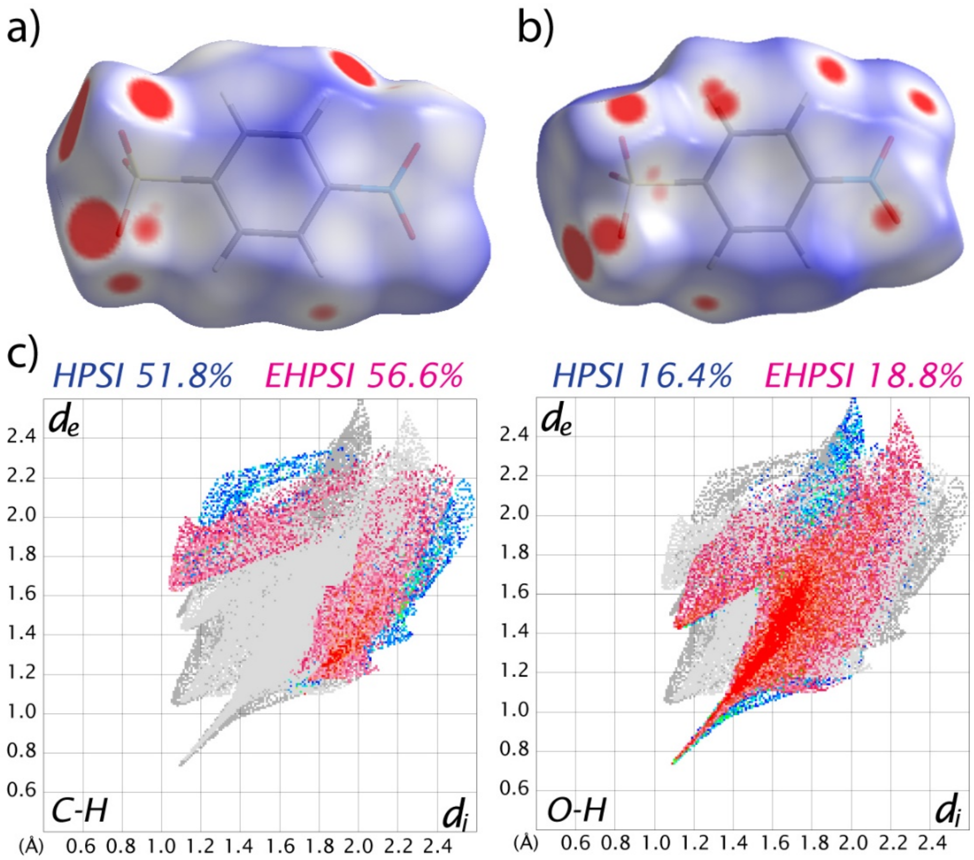

**Figure 4.10** Hirshfeld surface analysis of 4NBS anions for a) HPSI-4NBS and b) EHPSI-4NBS. c) fingerprint plots for C-H and O-H intermolecular interactions.

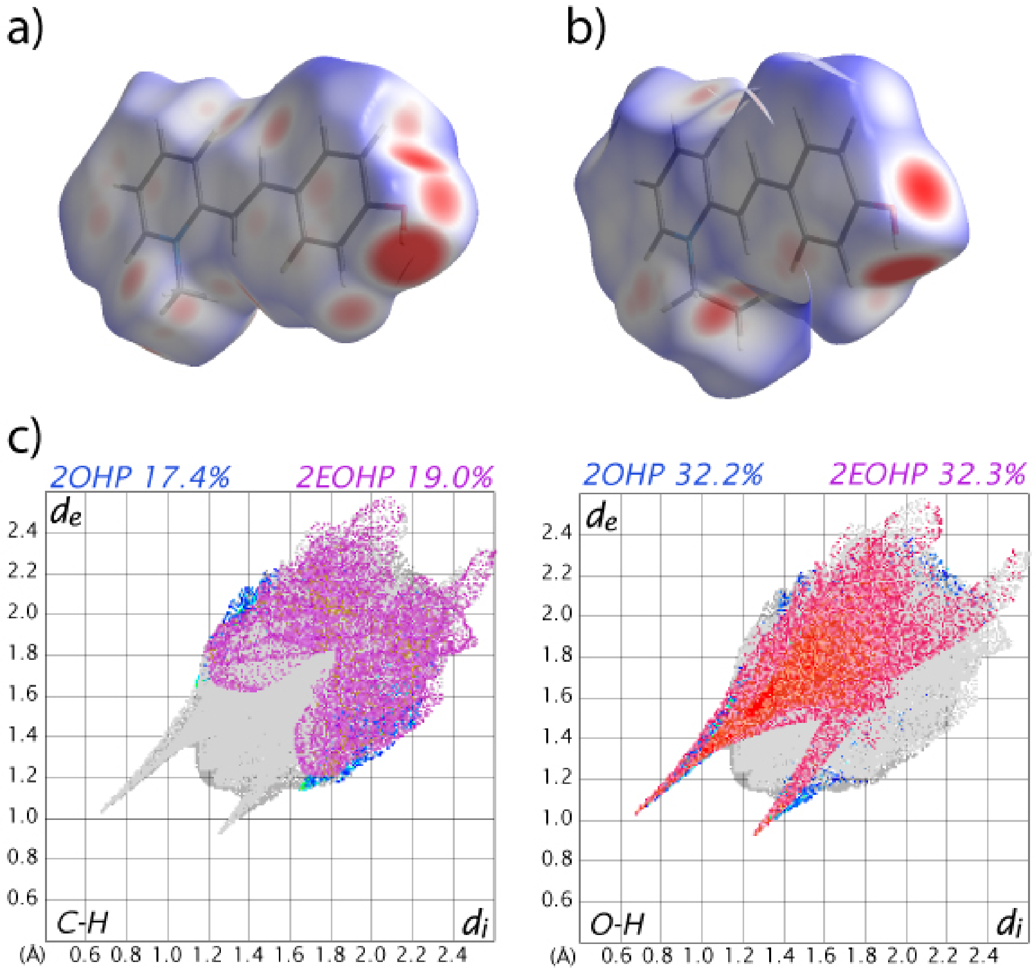

**Figure 4.11** Hirshfeld surface analysis of cations for a) 2OHP-4NBS and b) 2EOHP-4NBS. c) fingerprint plots for C-H and O-H intermolecular interactions

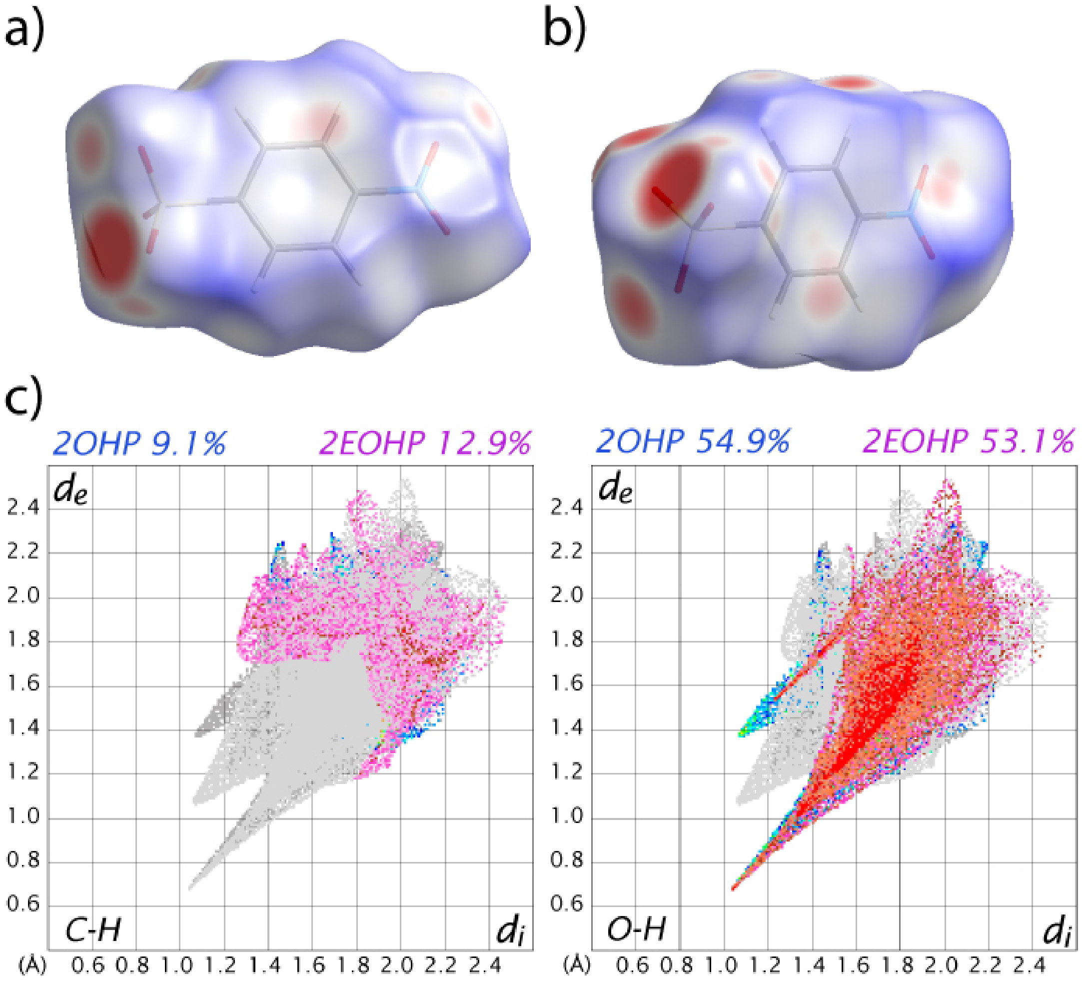

**Figure 4.12** Hirshfeld surface analysis of 4NBS anions for a) 2OHP-4NBS and b) 2EHOP-4NBS. c) fingerprint plots for C-H and O-H intermolecular interactions.

### 4.6.2 Hyperpolarizability calculations

With experimental atomic positions from the x-ray structures, the molecular hyperpolarizability values ($\beta_{exp}$) were calculated utilizing finite field calculations and the x-rays coordinates of HPSI-4NBS and EHPSI-4NBS. The B3LYP functional and the 6-311++G level of theory were chosen to set up the calculations in the Gaussian 09 suite.[8] The components of the first hyperpolarizability tensor were calculated, $\beta_{ijk}$, and the final reported values were calculated using the following equations:

$$\beta_i = \sum_j (\beta_{ijj} + \beta_{jij} + \beta_{jji}) \qquad \textbf{Eq. 4.1}$$

$$\beta_{tot} = \sqrt{\beta_x^2 + \beta_y^2 + \beta_z^2} \qquad \textbf{Eq. 4.2}$$

### 4.6.3 THz generation setup

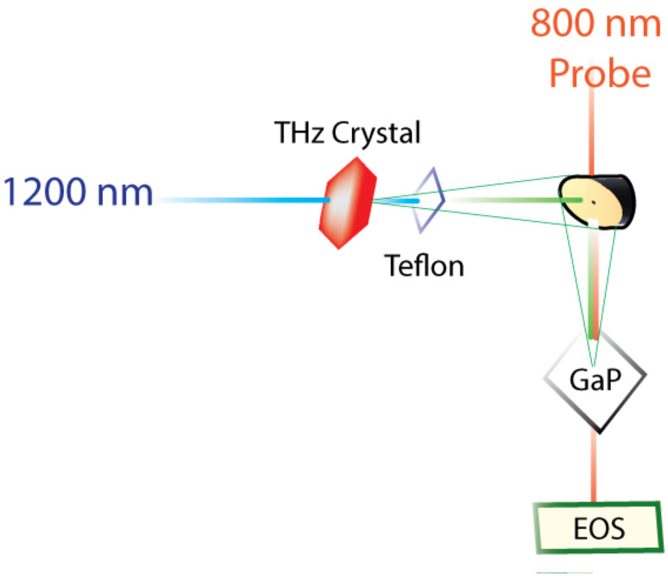

**Figure 4.13** THz generation setup from organic crystals. 1200-nm light passes through the molecular crystal and generates THz via optical rectification. Excess IR light is eliminated with a Teflon filter. Generated THz is then focused to an off-axis parabolic mirror and directed to a GaP electro-optic crystal. 800-nm light is focused onto GaP to probe the generated THz light and subsequently directed to an electro-optic sampling setup (EOS).

## 4.7 References

[1] R. W. Boyd, *Nonlinear optics*, Elsevier, **2003**.

[2] Y. J. Ding, I. B. Zotova, *Optical and quantum electronics* **2000**, 32, 531.

[3] H. Wu, H. Yu, Z. Yang, X. Hou, X. Su, S. Pan, K. R. Poeppelmeier, J. M. Rondinelli, *Journal of the American Chemical Society* **2013**, 135, 4215.

[4] X. Zheng, C. V. McLaughlin, P. Cunningham, L. M. Hayden, *Journal of Nanoelectronics and Optoelectronics* **2007**, 2, 58.

[5] Y.-J. Cheng, J. Luo, S. Hau, D. H. Bale, T.-D. Kim, Z. Shi, D. B. Lao, N. M. Tucker, Y. Tian, L. R. Dalton, P. J. Reid, A. K.-Y. Jen, *Chemistry of materials* **2007**, 19, 1154.

[6] L. R. Dalton, *Journal of Physics: Condensed Matter* **2003**, 15, R897.

[7] V. Krishnakumar, R. Nagalakshmi, *Physica B: Condensed Matter* **2008**, 403, 1863.

[8] J. Zyss, J. L. Oudar, *Physical Review A* **1982**, 26, 2028.

[9] O. P. Kwon, S.-J. Kwon, M. Stillhart, M. Jazbinsek, A. Schneider, V. Gramlich, P. Günter, *Crystal Growth and Design* **2007**, 7, 2517.

[10] G. A. Valdivia-Berroeta, L. K. Heki, E. A. McMurray, L. A. Foote, S. H. Nazari, L. Y. Serafin, S. J. Smith, D. J. Michaelis, J. A. Johnson, *Advanced Optical Materials* **2018**, 1800383.

[11] S. H. Lee, B. J. Kang, J. S. Kim, B. W. Yoo, J. H. Jeong, K. H. Lee, M. Jazbinsek, J. W. Kim, H. Yun, J. Kim, Y. S. Lee, F. Rotermund, O.-P. Kwon, *Advanced Optical Materials* **2015**, 3, 756.

[12] P. Günter, *Nonlinear optical effects and materials*, Springer, **2012**.

[13] S. R. Marder, J. W. Perry, *Advanced Materials* **1993**, 5, 804.

[14] Z. Sun, X. Liu, X. Wang, L. Li, X. Shi, S. Li, C. Ji, J. Luo, M. Hong, *Crystal Growth & Design* **2012**, 12, 6181.

[15] G. A. Valdivia-Berroeta, D. J. Michaelis, J. A. Johnson, S. J. Smith, Cambridge Crystallographic Data Centre, 2019.

[16] F. D. J. Brunner, O. P. Kwon, S.-J. Kwon, M. Jazbinšek, A. Schneider, P. Günter, *Optics express* **2008**, 16, 16496; S. H. Lee, J. Lu, S. J. Lee, J. H. Han, C. U. Jeong, S. C. Lee, X. Li, M. Jazbinšek, W. Yoon, H. Yun, B. J. Kang, F. Rotermund, K. A. Nelson, O. P. Kwon, *Advanced Materials* **2017**, 29, 1701748.

[17] T. Kobkeatthawin, T. Suwunwong, S. Chantrapromma, H. K. Fun, *Acta Crystallographica Section E: Structure Reports Online* **2009**, 65, o76.

[18] K.-H. Lee, S.-H. Lee, H. Yun, M. Jazbinsek, J. W. Kim, F. Rotermund, O. P. Kwon, *CrystEngComm* **2016**, 18, 5832.

[19] S. C. Lee, B. J. Kang, J. A. Lee, S. H. Lee, M. Jazbinšek, W. Yoon, H. Yun, F. Rotermund, O. P. Kwon, *Advanced Optical Materials* **2018**, 6, 1701258.

[20] J. Lu, H. Y. Hwang, X. Li, S.-H. Lee, O. P. Kwon, K. A. Nelson, *Optics express* **2015**, 23, 22723.

[21] F. Pan, M. S. Wong, C. Bosshard, P. Günter, *Advanced Materials* **1996**, 8, 592; C. U. Jeong, B. J. Kang, S. H. Lee, S. C. Lee, W. T. Kim, M. Jazbinsek, W. Yoon, H. Yun, D. Kim, F. Rotermund, O.-P. Kwon, *Advanced Functional Materials* **2018**, 1801143.

[22] T. P. Radhakrishnan, *Accounts of Chemical Research* **2008**, 41, 367.

[23] M. A. Spackman, D. Jayatilaka, *CrystEngComm* **2009**, 11, 19.

[24] S.-J. Kwon, O. P. Kwon, J.-I. Seo, M. Jazbinsek, L. Mutter, V. Gramlich, Y.-S. Lee, H. Yun, P. Günter, *The Journal of Physical Chemistry C* **2008**, 112, 7846.

[25] S. Okada, K. Nogi, K. Tsuji, X.-M. Duan, H. Oikawa, H. Matsuda, H. Nakanishi, *Japanese journal of applied physics* **2003**, 42, 668.

[26] G. A. Valdivia-Berroeta, L. K. Heki, E. W. Jackson, I. C. Tangen, C. B. Bahr, S. J. Smith, D. J. Michaelis, J. A. Johnson, *Optics Letters* **2019**, 44, 4279.

[27] Y. Wang, X. Tan, Y.-M. Zhang, S. Zhu, I. Zhang, B. Yu, K. Wang, B. Yang, M. Li, B. Zou, S. X.-A. Zhang, *Journal of the American Chemical Society* **2015**, 137, 931.

[28] Q. Wu, X. C. Zhang, *Applied Physics Letters* **1997**, 70, 1784.

# Chapter 5 6MNEP: A molecular cation with the highest reported second-order nonlinear susceptibility

## 5.1 Overview

As discussed throughout this dissertation, molecular organic crystals for nonlinear optical applications are usually designed using push-pull chromophores as the core feature. In this approach, electron-donating and accepting groups are connected trough a π-conjugated bridge to obtain planar molecules with high hyperpolarizability. However, the required non-centrosymmetric packing in the solid state is an important challenge to consider in the design of these materials. In this chapter, we present the new organic cation 6MNEP which shows high hyperpolarizability and ideal non-centrosymmetric molecular packing for NLO applications. This cation was obtained by extending the conjugation length of already existing chromophores. The crystal structures of 6MNEP combined with T and 4NBS anions are compared with other crystals that also have extended conjugation lengths, but result in centrosymmetric crystal structures. This work was submitted to Journal of Materials Chemistry C.

## 5.2 Introduction

Many non-centrosymmetric organic crystals have been studied for nonlinear optical (NLO) applications such as second-harmonic (SHG),[4] sum-frequency (SFG),[5] and terahertz (THz) generation.[6] These NLO materials feature ultrafast response times,[7] large second order susceptibilities,[8] and the possibility of incorporating different functional groups to improve the NLO activity.[9] In order to create efficient molecules for NLO applications, the molecular hyperpolarizability (β) can be optimized in organic push-pull electronic systems, however, we must still consider the required non-centrosymmetric packing in the crystalline state.[10]

As shown in **Figure 5.1a**, push-pull chromophores are designed by connecting electron donating (ED) with electron accepting (EA) groups using a π-conjugated aromatic bridge. For instance, the cation in the stilbazolium crystal DAST (4-dimethylamino-N-methyl-4-stilbazolium tosylate) features an ED dimethyl amino group connected through a styryl bridge to a pyridinium EA moiety.[11] Hydrogen bonding ED groups such as hydroxyl,[12] and methoxy[13] have also been employed in fabricating push-pull molecules. On the other hand, EA groups such as quinolinium[14] and indolium[15] have found applications in NLO material design.

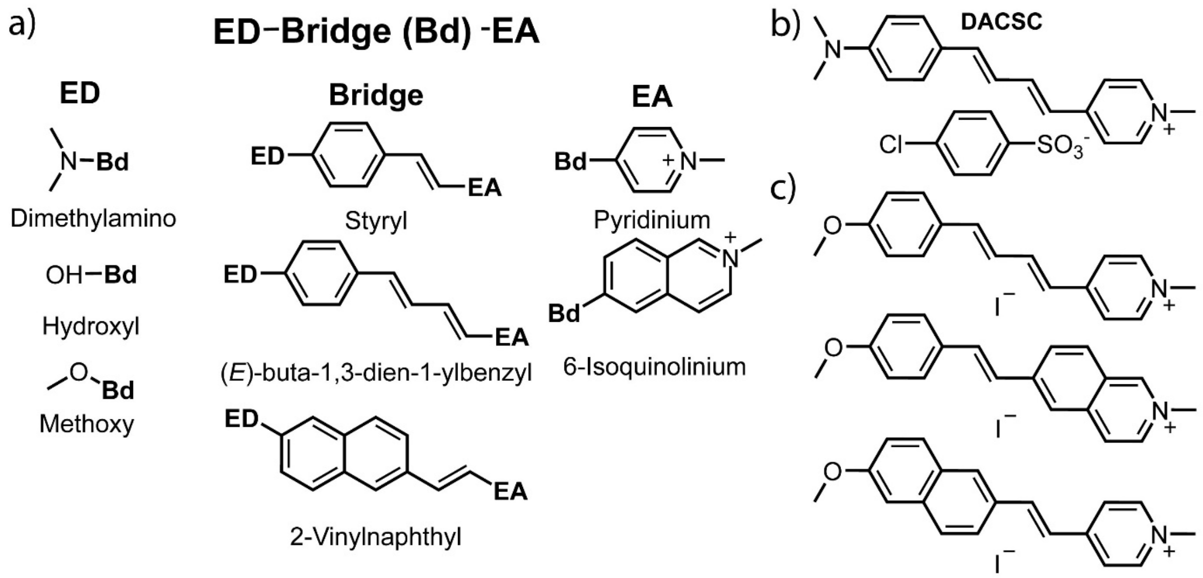

**Figure 5.1** a) Push-pull chromophores design using electron donating (ED), electron accepting (EA), and bridging (Bd) groups, b) DACSC molecular structure, and c) Organic chromophores developed by Ajito et al.

A common approach to increase β, while keeping the ED and EA groups unchanged, is to increase the π-conjugation length. Using this strategy, the bis-alkene derivative of DAST, DACSC (4-((1E,3E)-4-(4-(dimethylamino)phenyl)buta-1,3-dien-1-yl)-1-methylpyridin-1-ium 4-chlorobenzene sulfonate, **Figure 5.1b**),[16] was recently designed and characterized and shows the required non-centrosymmetric packing, but with sub-optimal cation-cation alignment and co-crystallized water molecules. **Figure 5.1c** shows chromophores designed by Tsuji *et al* with methoxy ED groups and extended conjugation lengths using either (E)-buta-1,3-dien-1-ylbenzyl or 2-vinylnaphtyl bridges connected to pyridinium or 6-isoquinolinium EA moieties.[17] Improved β values along with reduced maximum absorption wavelengths were found for the lower two fused-ring molecules. Despite the good characteristics of these π-extended systems, crystal structures were not reported and only qualitative second-harmonic generation tests were performed to prove the NLO activity of the chromophores.[17]

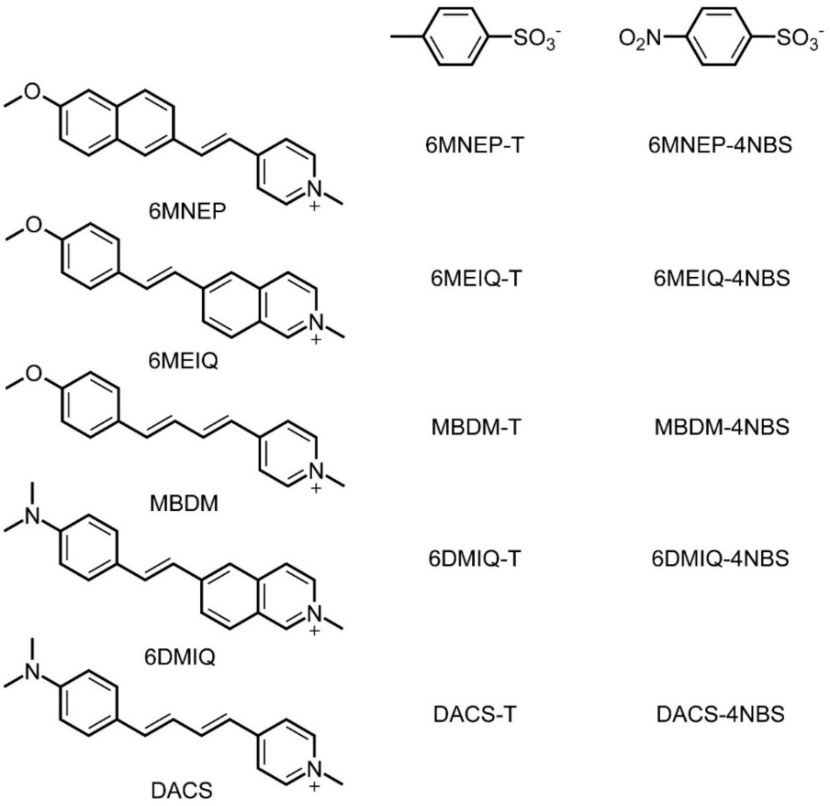

**Figure 5.2** Molecular structures of π-extended chromophores. From top to bottom, 6MNEP, 6MEIQ, MBDM, 6DMIQ, and DACS paired with T and 4NBS anions.

In this article, we report the crystal structures of five molecular cations with π-extended conjugation length. As shown in **Figure 5.2**, methoxy and dimethyl amino donating groups were combined with (E)-buta-1,3-dien-1-ylbenzyl and 2-vinylnaphtyl π-extended bridges in conjunction with pyridinium and 6-isoquinolinium EA groups to yield unique cations. The methoxy derivatives 6MENP, MBDM, and 6MEIQ along with dimethyl amino functionalized chromophores 6DMIQ and DACS were paired with T (p-toluenesulfonate) and 4NBS (4-nitrobenzenesulfonate) anions to form organic salts. Parallel arrangements giving centrosymmetric structures, and therefore no NLO activity, were found for MBDM, 6MEIQ, 6DMIQ and DACS chromophores with both sulfonyl anions. On the other hand, 6MNEP derivatives resulted into non-centrosymmetric packing in the crystalline state with nearly perfect alignment for NLO applications. We find the 6MNEP cation to have the highest hyperpolarizability of any organic crystal reported to date that crystallizes with ideal non-centrosymmetric alignment.

## 5.3 Results and discussions

### 5.3.1 Hyperpolarizability calculations and X-ray crystal structures analysis

In order to compare the molecular hyperpolarizability of the designed π-extended chromophores, *ab-initio* calculations in the gas phase were performed for all the compounds.[18] The $\beta_{gas}$ value of state-of-the-art DAS cation was also computed and utilized as reference. Geometry optimization and single-point hyperpolarizability calculations were obtained as explained in the experimental section. $\beta_{gas}$ values were found to be 286 (6MNEP), 243 (MBDM), 299 (6MEIQ), 394 (6DMIQ), and 282 (DACS) $\times 10^{-30}$ esu. These values are from 56% to 152% higher compared to the $\beta$ obtained for the DAS cation (155 x $10^{-30}$ esu). These results confirm the positive impact of π-extended systems on the molecular hyperpolarizability.

To evaluate the molecular packing of the featured organic salts, the different cations were synthesized with 4-methyl (T) and 4-nitro (4NBS) benzene sulfonate anions, and single crystals were grown via slow evaporation techniques. **Figure 5.3** shows the crystal structures obtained via X-ray diffraction experiments for the methoxy derivatives. Arrows from ED to EA groups are drawn to indicate parallel and anti-parallel arrangements. Lattice and refinement parameters for the obtained crystal structures are detailed in the Supporting information. As observed on the top of **Figure 5.3**, 6MNEP-T and 6MNEP-4NBS feature similar molecular packing and the same triclinic P1 space group with nearly perfect alignment for NLO applications. Other chromophores with known NLO activity, such as DSNS and OHP-CBS (refs), have crystallized in the same space group. As shown in **Figure 5.9** in the supporting information section, 6MNEP was also paired with 3NBS (3-nitrobenzenesulfonate) and 4TFS (4-(trifluoromethyl)benzenesulfonate) anions, however the 3NBS derivative is centrosymmetric and the 4TFS compound, while non-centrosymmetric, features sub-optimal molecular packing.

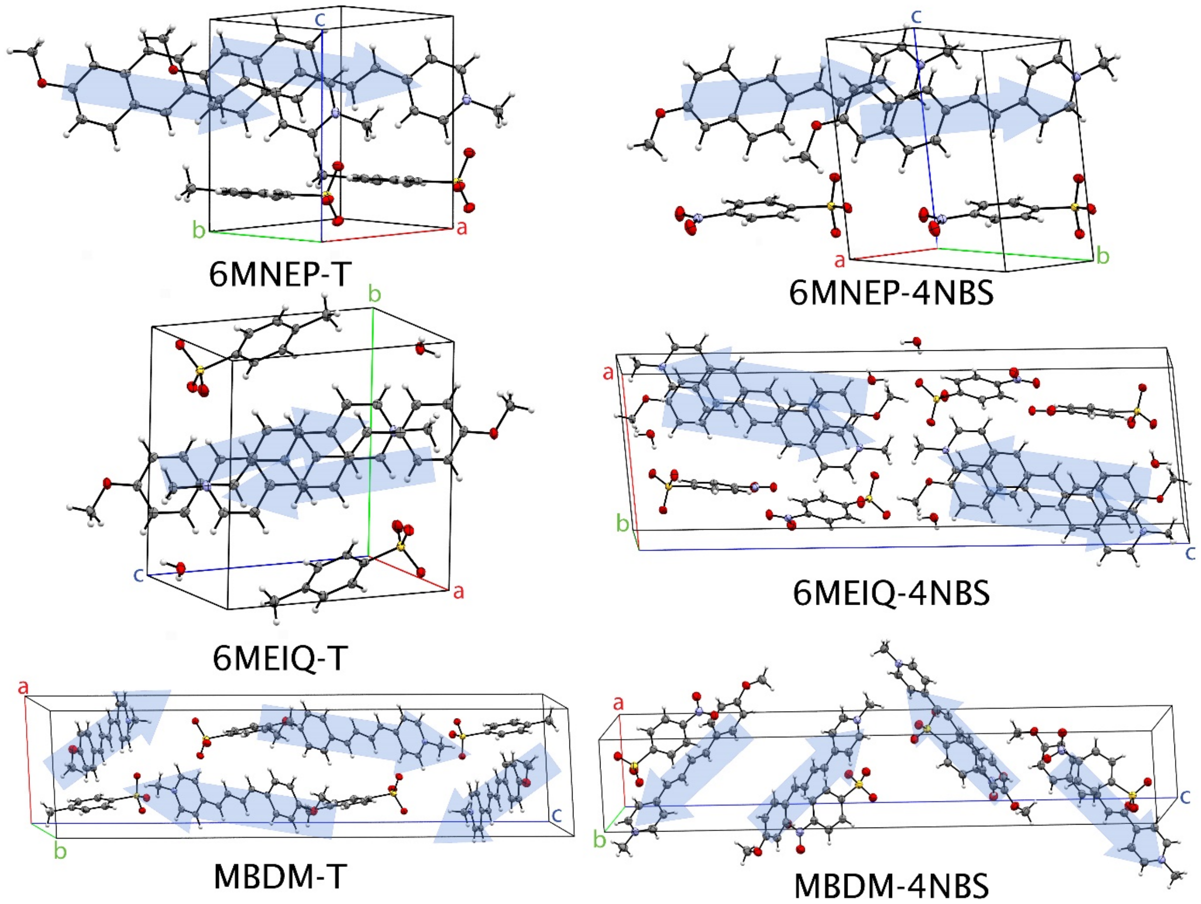

**Figure 5.3** Crystal structures of π-extended methoxy derivatives. Blue arrows point from ED to EA groups and indicate parallel (6MNEP) and anti-parallel (MBDM, 6MEIQ) packing.

Similar to 6MNEP, 6MEIQ also features a fused ring system with extended conjugation, however solvent molecules were co-crystallized in the solid state. This could explain the centrosymmetric molecular packing obtained for 6MEIQ-T and 6MEIQ-4NBS (see **Figure 5.3**). In order to eliminate these crystallized solvent molecules, the methyl attached to the quaternary isoquinolinium nitrogen was replaced by an ethyl group. **Figure 5.10** in the supporting information shows the molecular packing of 6MEIQE-4NBS with no co-crystallized solvent molecules, but the molecular packing maintains its centrosymmetric alignment. On the other hand, the bisalkene chromophore MBDM crystallizes in the centrosymmetric monoclinic space group $P2_1/c$ when combined with the T anion, while MBDM-4NBS features a $P2_12_12_1$ non-centrosymmetric space group, as observed at the bottom of **Figure 5.3**. Despite the acentric nature of the orthorhombic MBDM-4NBS crystal, the arrangement of the molecular cations is anti-parallel, and therefore we don't expect NLO activity. **Figure 5.9c** in the supporting information shows the crystal packing of MBDM-N2S

(N2S = 2-naphthalenesulfonate), which also forms a centrosymmetric arrangement. In order to induce head-to-tail relative conformations, the methyl moiety in the quaternary nitrogen of MBDM was substituted for an ethyl group. As shown in **Figure5.11** in the supporting information, similar conformations with non-centrosymmetric space groups, but poor molecular alignment, were obtained for the ethylated compounds when combined with 3NBS, 4NBS, N2S, and CBS (4-chlorobenzenesulfonate).

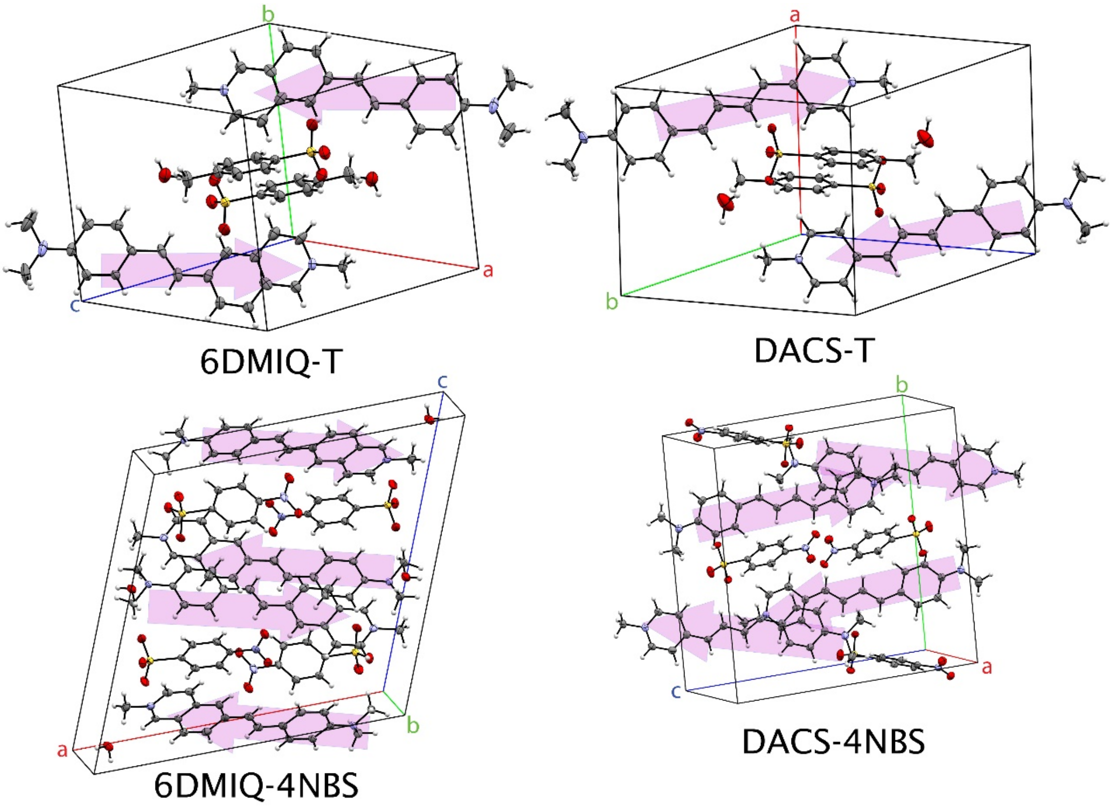

**Figure 5.4** Crystal structures of π-extended dimethylamino derivatives. Pink arrows go from ED to EA groups and indicate parallel and anti-parallel packing.

As shown in **Figure 5.4**, all the chromophores with dimethylamino ED groups (6DMIQ, DACS) feature centrosymmetric space groups. Other organic crystals with dimethylamino groups (DAST and 4DEP) have been shown to form centrosymmetric packing when co-crystallized water molecules are present.[19] However, DACS-4NBS doesn't show any co-crystallized water molecules and the observed molecular packing is still centrosymmetric. To try to eliminate the water molecules from the 6DMIQ crystals, the cation was modified with an N-ethyl group instead of a methyl group on the isoquinolinium nitrogen. The crystal structures for the ethylated molecular cation paired with different anions are shown in **Figure**

**5.12** in the supporting information. Even though co-crystallized water molecules are not present, the molecular packing is still centrosymmetric and therefore NLO inactive.

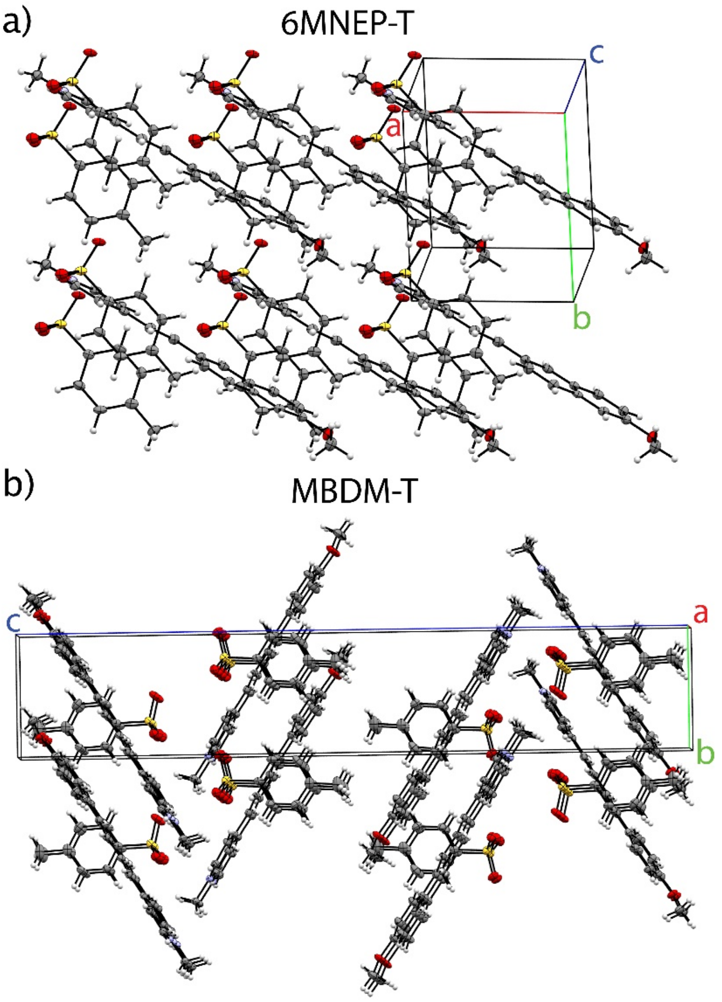

**Figure 5.5** Cation relative conformations for a) MBDM-T and b) 6MNEP-T

As we see above, 6MENP shows optimal molecular packing, and therefore we examine the crystal structure of 6MNEP-T in more detail and compare it with MBDM-T. As shown in **Figure 5.5,** 6MNEP-T features parallel relative conformations in contrast to antiparallel packing observed in MBDM-T. The drastic differences in molecular packing observed in methoxy functionalized chromophores could be attributed to the presence of an extra aromatic ring in the ED side of 6MNEP. The increased Van der Waals volume induced by the extra ring in 6MNEP could be responsible for the favorable interactions in the crystalline state that induce the head-to-tail conformations. However, similar conformations were not observed in 6MEIQ, which also features an extra aromatic ring compared to MBDM. This is mainly due to the presence of co-crystallized solvent molecules, and therefore correlations between one extra aromatic ring and non-centrosymmetric packing are impossible to establish.

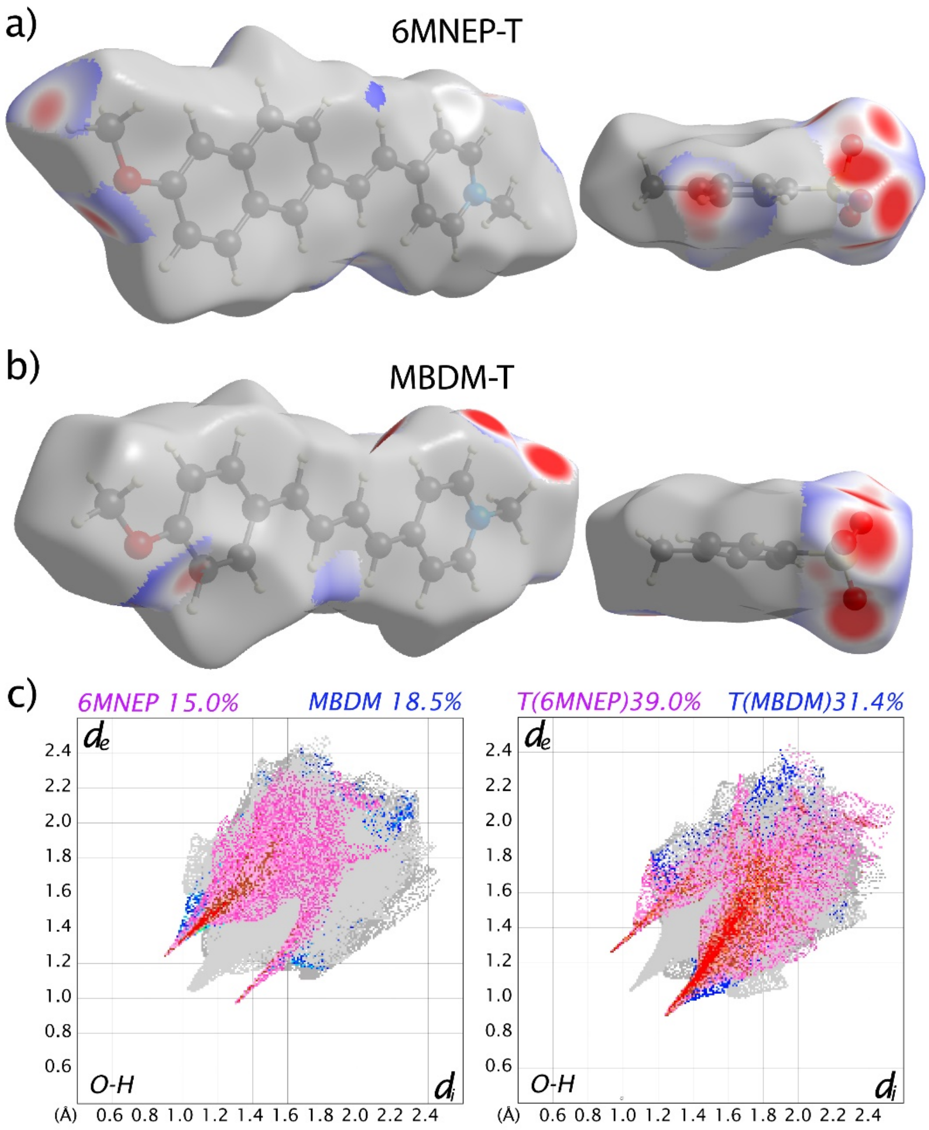

**Figure 5.6** Hirshfeld surfaces of a) 6MNEP-T and b) MBDM-T. c) Fingerprint plots for O-H intermolecular interactions present in 6MENP-T (pink) and MBDM-T (blue)

To characterize specific intermolecular interactions in 6MNEP-T and MBDM-T that could help explain the drastic differences in molecular packing, we calculated Hirshfeld surfaces as explained in the method sections. **Figure 5.6a-b** shows the Hirshfeld surfaces of 6MNEP-T and MBDM-T, normalized to the atomic Van der Waals volumes, characterizing O-H intermolecular interactions. As observed in **Figure 5.6c**, 6MNEP-T features overall shorter interaction distances compared with MBDM-T. This is explained by strong cation-cation interactions between the ED methoxy group and the methyl attached to the quaternary nitrogen of the EA moiety. As seen in **Figure 5.6b**, this same interaction is not observed in MBDM-T and appears to be responsible of the ideal alignment observed in 6MNEP chromophores.

### 5.3.2 Linear and Nonlinear Optical properties

To evaluate the applicability of 6MNEP-T and 6MNEP-4NBS as potential NLO crystals, the second-order nonlinear susceptibility parameters, $\chi^{(2)}$, were calculated using the 1-D chromophore approximation[19] and compared with DAST. We used the 1-D approximation of $\chi^{(2)}$ according to equation 5.1:

$$\chi^{(2)} = F_{ijk} N \beta_{exp} \cos^3(\theta_p) \qquad \textbf{Eq. 5.1}$$

$F_{ijk}$ was assumed to be roughly equal for all of the organic salts, and the chromophore density $N$ was obtained from the ratio between the number of cations in the unit cell and the unit cell volume. $\beta_{exp}$ was obtained from DFT single point calculations using the measured crystal atomic coordinates. The order parameter ($\cos^3(\theta_p)$) was calculated from the angle between $\beta$ and the *ac*-crystallographic plane, as depicted in **Figure 5.7**. The obtained results are summarized in **Table 5.1.** Relative $\chi^{(2)}$ values corresponding to 75% and 78% higher than DAST are observed for 6MNEP-T and 6MNEP-4NBS, respectively. These values correspond to the highest relative $\chi^{(2)}$ (compared to DAST) reported so far in the literature. Another important consideration in designing organic NLO crystals is to keep the wavelength of maximum absorption ($\lambda_{max}$) shifted to values < 410 nm to avoid two-photon absorption processes that occur when the crystals are irradiated with high-power lasers. A common system employed to pump these NLO crystals is the Ti:Sapphire laser with a central wavelength of 800 nm. As observed in **Table 5.1**, the $\lambda_{max}$ values for DAST, 6MNEP-T, and 6MNEP-4NBS are 475, 399, and 399 nm, respectively. Therefore, the likelihood of getting two-photon absorption damage in a DAST crystal when pumped with a Ti:Sapphire system is higher compared with 6MNEP-T and 6MENP-4NBS crystals. Additionally, yellow crystals similar to 6MNEP-T with $\lambda_{max}$ at or below 400 nm have often shown improved phase-matching conditions for NLO experiments compared with orange or red crystals like DAST.[20]

**Table 5.1** Relative $\chi^{(2)}$ and $\lambda_{max}$ for DAST, 6MNEP-4NBS, and 6MNEP-T.

| **Chromophore** | $\beta_{exp}$ **(x10$^{-30}$ esu)** | **cos$^3$($\theta_p$)** | $N$ **(Å$^{-3}$)** | **Relative $\chi^{(2)}$** | $\lambda_{max}$ **(nm)** |
|---|---|---|---|---|---|
| **DAST** | 201 | 0.83 | 0.0019 | **1.00** | **475** |
| **6MNEP-T** | 306 | 0.97 | 0.0018 | **1.78** | **399** |
| **6MNEP-4NBS** | 301 | 0.97 | 0.0018 | **1.75** | **399** |

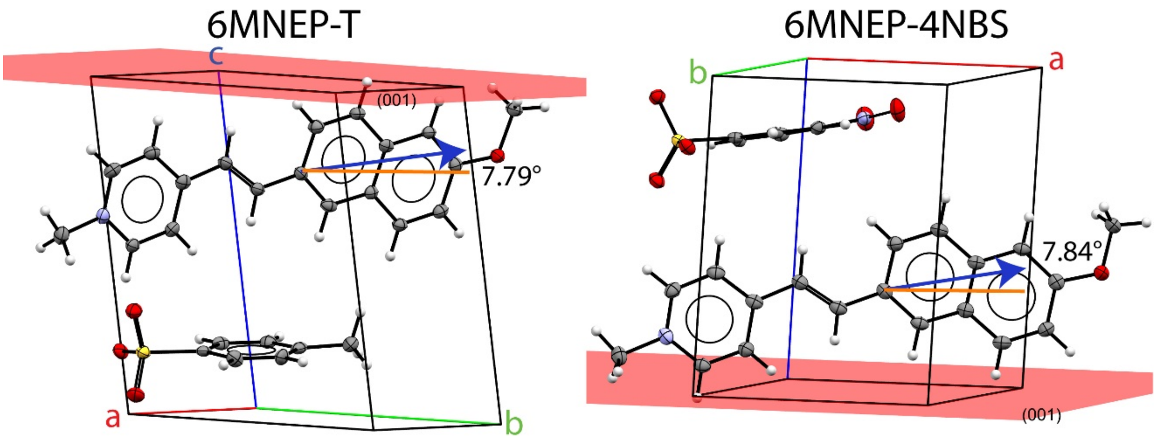

**Figure 5.7** Angle between the molecular hyperpolarizability (blue) and the polar axis (red) for a) 6MNEP-T, and b) 6MNEP-4NBS.

Slow evaporation and slow-cooling methods with different organic solvents are currently being tested to grow large crystals of 6MNEP-T and 6MNEP-4NBS. To date, only polycrystalline solids have been obtained, as confirmed by XRD experiments. Similar crystallization problems have been reported for the nonlinear crystal DSNS,[3] however a study from Guan *et al* showed the possibility of growing DSNS nanowires with detectable SHG activity.[21] We propose that 6MNEP compounds can be utilized for similar applications, and we are currently pursuing these efforts.

## 5.4 Conclusions

Chromophores with π-extended conjugation lengths were synthesized and crystal structures reported for 6MNEP, MBDM, 6MEIQ, 6DMIQ, and DACS with T and 4NBS anions. Despite the improved $\beta$ values for these chromophores, only compounds containing 6MNEP cations crystallized with nearly perfect alignment for NLO applications. The $\chi^{(2)}$ parameters of 6MENP-T and 6MNEP-4NBS were 75% and 78% higher compared with state-of-the-art DAST crystal. Work is currently underway to produce large high-quality crystals optimal for NLO applications.

## 5.5 Experimental Section

*Synthesis and NMR characterization:* 6MNEP, MBDM, and DACS organic salts were synthesized by a condensation reaction at room temperature between the 1,4-dimethyl pyridinium sulfonate salts and the corresponding aldehydes in the presence of piperidine as the catalyst. 6DMIQ and 6MEIQ derivatives were obtained by Wittig reaction of the corresponding benzaldehydes to obtain N,N-dimethyl- and 4-methoxy- 4-vinylaniline. The vinyl compound was reacted with 6-bromoisoquinoline with Pd(OAc) as catalyst to obtain the 6DMIQ and 6MEIQ cation precursors. Anions were added by alkylation reactions in toluene. Additional details about the reaction procedures, yields, and NMR data are provided in the Supporting Information.

*Calculations:* Density functional theory calculations were performed using the Gaussian 16 software. The B3LYP functional along with 6-311++G** level of theory was employed to optimize molecular geometries and then find the β tensor components. The total magnitude of $\beta$ was calculated using the following equations:

$$\beta_i = \sum_j (\beta_{ijj} + \beta_{jij} + \beta_{jji})$$ **Eq. 5.2**

$$\beta_{tot} = \sqrt{\beta_x^2 + \beta_y^2 + \beta_z^2}$$ **Eq. 5.3**

*X-ray crystallography:* Small single crystals for X-ray diffraction experiments were obtained by slow evaporation of the compounds in methanol. The crystals were harvested in oil, mounted in a loop and centered using a video camera. Diffraction data were collected using a Cu ($K_\alpha$, 1.54178 Å) rotating anode as the X-ray source and a CCD camera as the detector. Diffraction peaks were integrated, scaled and corrected using the APEX3 software package. Chemical structures were solved with the dual-space algorithm incorporated in SHELXT.[22] Refinement of the initial structural solutions was performed against $F^2$ on all data using least squares full-matrix strategy as it is included in SHELXL-2014.[23] Unit cell and refinement parameters are reported in the Supporting Information.

*Hirshfeld analysis:* Hirshfeld surfaces were calculated using the Crystal Explorer software. Surfaces were calculated considering the atomic Van der Waals radius of the atoms inside the surface. Plots characterizing the inner atom – surface distances ($d_i$) and the outer atom – surface distances ($d_e$) were also generated.

*Optical Characterization:* UV-Vis absorption measurements were performed in a Carry 5e spectrometer using a 1-cm quartz cell and methanol as solvent. Data were collected from 300 to 500 nm and the absorption intensity was normalized for comparison between chromophores.

## 5.6 General and Supporting Information

### 5.6.1 Organic Synthesis and NMR Characterization

6MNEP, MBDM, and DACS compounds were synthesized in a similar manner. Here, we explain the synthesis of 6MENP-T as procedure example.

***Methyl 4-methylbenzenesulfonate***: Metallic sodium (1.63g, 1eq) was weighed out, washed with hexanes and reacted with dry methanol (80 mL) to produce sodium methoxide. This solution was dropwise added to a 4-methylbenzenesulfonyl chloride/DCM solution (10g in 200 ml of solution) and the solvent evaporated. The resulting solids were extracted with DCM and water, dried over sodium sulfate, and the solvent was removed at reduced pressure. Methyl 4-chlorobenzenesulfonate (83% yield) was obtained and used in the next step without further purification.

***1,4-dimethylpyridin-1-ium 4-methylbenzenesulfonate***: 4-picoline (12g, 2 eq) was combined with 4-methylbenzenesulfonate (10.5g, 1eq) in toluene. The mixture was stirred at 100°C for 3h, then the precipitated solids were filtered and washed with toluene. A white powder was recovered and identified as 1,4-dimethylpyridin-1-ium 4-methylbenzenesulfonate (98% yield)

***(E)-4-(2-(6-methoxynaphthalen-2-yl)vinyl)-1-methylpyridin-1-ium 4-methylbenzenesulfonate (6MNEP-T)***: 1,4-dimethylpyridin-1-ium 4-chlorobenzenesulfonate (17g, 1eq) was combined with 6-methoxy naphtaldehyde (8.13g, 1eq) in ethanol at room temperature. Piperidine (50 drops) was added and the reaction was stirred at room temperature for 3 days. A yellow solid was recovered by filtration and washed with toluene to afford 6MNEP-T (65 %yield).

6DMIQ and MEIQ derivatives were obtained using Wittig and Heck reactions. The different steps to obtain 6DMIQ-T are detailed below:

***N,N-dimethyl-4-vinylaniline*****:** To a stirred solution of methyltriphenylphosphonium bromide in dry THF (1 eq, 0.12 M), *n*-Butyl lithium (1 eq) was added dropwise. The resulting solution was stirred for 15 minutes and then 4-(dimethylamino)benzaldehyde (1 eq) was added. After 3h, saturated ammonium chloride was added and the resulting mixture was extracted with DCM. The extracted organic layers were dried over $Na_2SO_4$ and concentrated *in vacuo*. The final product was purified by column chromatography (1:2, ethyl acetate:hexanes)

***(E)-4-(2-(isoquinolin-6-yl)vinyl)-N,N-dimethylaniline*****:** N,N-dimethyl-4-vinylaniline (1.25 eq) was combined with 6-bromoisoquinoline (1 eq) in dry trimethylamine. The $Pd(OAc)_2$ catalyst (0.02 eq) and tri-otolyl phosphine (0.04 eq) were added and the reaction was stirred for 48h at 80°C. The reaction mixture was concentrated by evaporation of the solvent and column chromatography (1:4, ethyl acetates:hexanes) afforded the purified coupled product.

***(E)-6-(4-(dimethylamino)styryl)-2-methylisoquinolin-2-ium 4-methylbenzenesulfonate (6DMIQ-T)*****:** The coupled product obtained in the previous step was reacted with methyl 4-methylbenzenesulfonate in toluene at 80°C for 24h. The resulting organic salt was collected by filtration. (Yield, 98%)

NMR characterization was performed in a 500 MHz spectrometer. All compounds were dissolved in DMSO-d6 and the shifts are reported with respect to TMS.

***(E)-6-(4-methoxystyryl)isoquinoline (6MEIQ)*****:** $^1$H NMR (500 MHz, $C_2D_6OS$), 9.195 (s, 1H), 8.501 (s, 1H), 7.932 (d, J: 8.01Hz, 1H), 7.826 (d, J: 8.01Hz, 1), 7.784 (s, 1H), 7.612 (s, 1H), 7.520 (d, J: 7.01Hz), 7.296-7.232 (m, 3H), 7.180-7.098 (m, 1H), 6.942 (d, J: 7.01Hz, 2H), 3.853 (s, 3H).

***(E)-4-(2-(6-methoxynaphthalen-2-yl)vinyl)-1-methylpyridin-1-ium 4-methylbenzenesulfonate (6MNEP-T)*****:** $^1$H NMR (500 MHz, $C_2D_6OS$), 8.842 (d, J: 6.72 Hz, 2H) 8.221 (d, J: 6.60 Hz, 2H), 8.126 (t, 2H), 7.915 (m, 3H), 7.574 (d, J: 16.38Hz, 1H), 7.465 (d, J: 7.94 Hz, 2H), 7.391 (d, J: 2.32 Hz, 1H), 7.235 (dd, J1: 2.44 Hz, J2: 6.48 Hz, 1H), 7.10 (d, J: 7.95 Hz, 2H), 4.247 (s, 3H), 3.906 (s, 3H), 2.279 (s, 3H).

***(E)-4-(2-(6-methoxynaphthalen-2-yl)vinyl)-1-methylpyridin-1-ium 4-nitrobenzenesulfonate (6MNEP-4NBS)*****:** $^1$H NMR (500 MHz, $C_2D_6OS$), 8.822 (d, J:6.72 Hz, 2H), 8.205 (m, 4H), 8.105 (t, 2H), 7.917 (m, 3H), 7.8425 (t, 2H), 7.573 (d, J: 16.26 Hz, 1H), 7.441 (d, J: 12.35 Hz, 1H), 7.211 (dd, J1: 2.57 Hz, J2: 6.35 Hz, 1H), 4.247 (s, 3H), 3.906 (s, 3H).

***(E)-6-(4-methoxystyryl)-2-methylisoquinolin-2-ium 4-methylbenzenesulfonate (6MEIQ-T)*****:** $^1$H NMR (500 MHz, $C_2D_6OS$), 9.805 (s, 1H), 8.594 (s, 1H), 8.427-8.374 (m, 2H), 8.375-8.288 (m, 2H), 7.775-7.662 (m, 3H), 7.489-7.296 (m, 3H), 7.106 (d, J: 6.61Hz, 2H), 7.036 (d, J: 6.61Hz, 2H), 4.413 (s, 3H), 3.817 (s, 3H), 2.284 (s, 3H).

***(E)-6-(4-methoxystyryl)-2-methylisoquinolin-2-ium 4-nitrobenzenesulfonate (6MEIQ-4NBS)*****:** $^1$H NMR (500 MHz, $C_2D_6OS$), 9.798 (s, 1H), 8.606 (d, J: 6.88 Hz, 1H), 8.407 (t, J: 6.69 Hz, 2H), 8.356-8.308 (m, 2H), 8.201 (d, J: 6.84 Hz, 2H), 7.832 (d, J: 6.85 Hz, 2H), 7.753-7.696 (m, 3H), 7.452 (d, J: 16.33 Hz, 1H), 7.041 (d, J: 8.78 Hz, 2H), 4.412 (s, 3H), 3.820 (s, 3H).

***4-((1E,3E)-4-(4-methoxyphenyl)buta-1,3-dien-1-yl)-1-methylpyridin-1-ium 4-methylbenzenesulfonate (MBDM-T)*****:** $^1$H NMR (500 MHz, $C_2D_6OS$), 8.8567 (d, J:6.73Hz 2H), 7.8758-7.7821 (m, 4H), 7.5121 (m, 3H), 7.1509 (d, J: 7.46Hz, 2H), 7.0109-6.837 (m, 4H), 6.5653 (d, J: 15.74Hz, 1H), 4.468 (s, 3H), 3.8509 (s, 3H), 2.3367 (s, 3H).

***4-((1E,3E)-4-(4-methoxyphenyl)buta-1,3-dien-1-yl)-1-methylpyridin-1-ium 4-nitrobenzenesulfonate (MBDM-4NBS)*****:** $^1$H NMR (500 MHz, $C_2D_6OS$), 8.758 (d, J: 6.6 Hz, 2H), 8.193 (d, J: 8.68 Hz, 2H), 8.095 (d, J: 6.73 Hz, 2H), 7.827 (d, J: 8.8 Hz, 2H), 7.604 (d, J: 8.55 Hz, 2H), 7.156-1.104 (m, 2H), 7.057-6.977 (m, 3H), 6.824 (d, J: 15.4 Hz, 2H), 4.105 (s, 3H), 3.792 (s, 3H).

***(E)-6-(4-(dimethylamino)styryl)-2-methylisoquinolin-2-ium 4-methylbenzenesulfonate (6DMIQ-T)*****:** $^1$H NMR (500 MHz, $C_2D_6OS$), 9.725 (s, 1H), 8.546 (d, J: 6.84, 1H), 8.345-8.287 (m, 3H), 8.220 (s, 1H), 7.673 (d, J: 16 Hz, 1H), 7.578 (d, J: 8.8 Hz, 2H), 7.463 (d, J: 7.81 Hz, 2H), 7.288 (d, J: 16 Hz, 1H), 7.103 (d, J: 7.82 Hz, 2H), 6.776 (d, J: 8.68, 2H), 4.380 (s, 3H), 2.992 (s, 6H), 2.281 (s, 3H).

***(E)-6-(4-(dimethylamino)styryl)-2-methylisoquinolin-2-ium 4-nitrolbenzenesulfonate (6DMIQ-4NBS)*****:** $^1$H NMR (500 MHz, $C_2D_6OS$), 9.732 (s, 1H), 8.520 (d, J: 6.84, 1H), 8.315-8.287 (m, 3H), 8.220 (s, 1H), 7.873 (d, J: 16 Hz, 1H), 7.653 (d, J: 8.8 Hz, 2H), 7.385 (d, J: 7.81 Hz, 2H), 7.236 (d, J: 16 Hz, 1H), 7.154 (d, J: 7.82 Hz, 2H), 6.798 (d, J: 8.68, 2H), 4.380 (s, 3H), 2.925 (s, 6H), 2.302 (s, 3H).

***4-((1E,3E)-4-(4-(dimethylamino)phenyl)buta-1,3-dien-1-yl)-1-methylpyridin-1-ium 4-methylbenzenesulfonate (DACS-T)*****:** $^1$H NMR (500 MHz, $C_2D_6OS$), 8.690 (d, J: 6.88 Hz, 2H), 8.217-8.8.183 (m, 2H), 8.024 (d, J: 6.88Hz, 2H), 7.859-7.763 (m, 3H), 7.471 (d, J: 8.60 Hz, 2H), 7.021-6.996 (m, 2H), 6.752-6.697 (m, 3H), 4.181 (s, 3H), 3.311 (s, 3H), 2.988 (s, 6H).

***4-((1E,3E)-4-(4-(dimethylamino)phenyl)buta-1,3-dien-1-yl)-1-methylpyridin-1-ium 4-nitrobenzenesulfonate (DACS-4NBS)*****:** $^1$H NMR (500 MHz, $C_2D_6OS$), 8.687 (s, 2H), 8.194 (d, J: 6.70Hz, 2H), 8.018 (s, 2H), 7.857-7.750 (m, 3H), 7.469 (d, J: 7.81Hz, 2H), 7.005 (s, 2H), 6.759-6.690 (m, 3H), 4.177 (s, 3H), 2.986 (s, 6H).

### 5.6.2 X-ray diffraction analysis

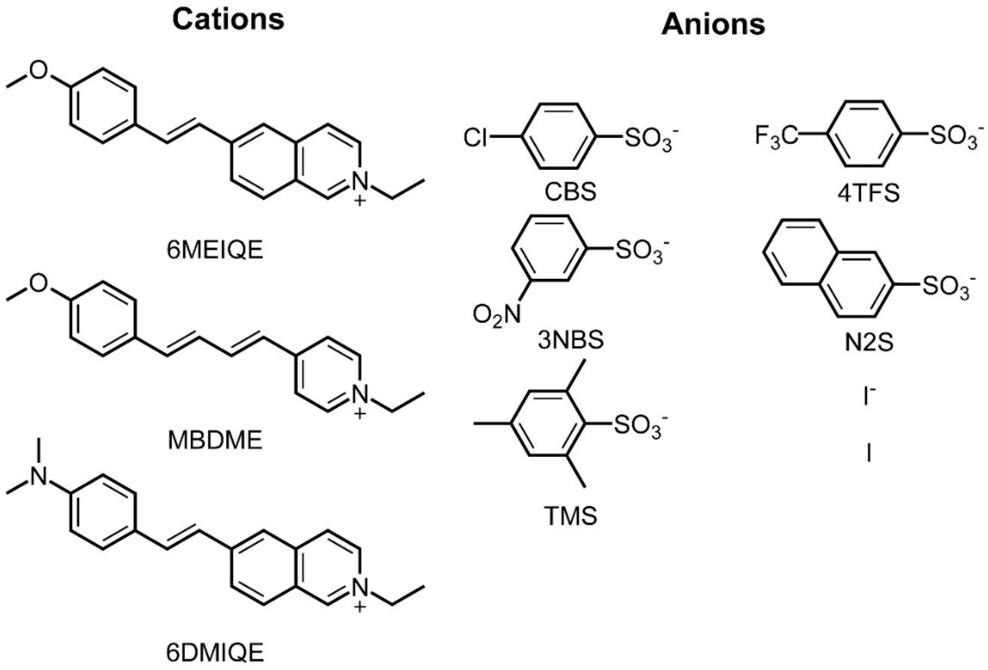

**Figure 5.8** Molecular structures of ethylated cations, sulfonate anions and iodide

**6MNEP-T:** *Crystal System*, triclinic; *Space Group*, P1; *Point group*, -1; a, 6.9488(3) Å; *b*, 8.1027(4) Å; *c*, 9.9927(5) Å; *a*, 104.045(3)°; *β*, 97.177(3)°; *γ*, 93.047(3)°; *z*, 1; $R_1$, 0.0353; $wR_2$, 0.0867; *GOF*, 1.069; *CCDC*: 1867834.

**6MNEP-4NBS:** *Crystal System*, triclinic; *Space Group*, P1; *Point group*, -1; a, 7.1520(2) Å; *b*, 7.9596(3) Å; *c*, 9.8172(3) Å; *a*, 102.972(2)°; *β*, 96.957(2)°; *γ*, 91.888(2)°; *z*, 1; $R_1$, 0.0267; $wR_2$, 0.0692; *GOF*, 1.064; *CCDC*: 1867835.

**6MEIQ-T:** *Crystal System*, triclinic; *Space Group*, P-1; *Point group*, -1; a, 8.2355(5) Å; *b*, 11.1247(7) Å; *c*, 12.4991(6) Å; *a*, 86.568(4)°; *β*, 75.984(4)°; *γ*, 88.350(4)°; *z*, 2; $R_1$, 0.0496; $wR_2$, 0.1192; *GOF*, 1.072; *CCDC*: 1990758.

**6MEIQ-4NBS:** *Crystal System*, monoclinic; *Space Group*, $P2_1/c$; *Point group*, 2/m; a, 10.5725(6) Å; *b*, 6.6821(4) Å; *c*, 32.4379(18) Å; *a*, 90°; *β*, 95.284(3); *γ*, 90°; *z*, 4; $R_1$, 0.0382; $wR_2$, 0.1029; *GOF*, 1.030; *CCDC*: 1973403.

**MBDM-T:** *Crystal System*, monoclinic; *Space Group*, $P2_1/c$; *Point group*, 2/m; a, 8.8320(6) Å; *b*, 6.6710(5) Å; *c*, 36.675(3) Å; *a*, 90°; *β*, 95.170(5); *γ*, 90°; *z*, 4; $R_1$, 0.0418; $wR_2$, 0.1086; *GOF*, 1.045; *CCDC*: 1962606.

**MBDM-4NBS:** *Crystal System*, orthorhombic; *Space Group*, $P2_12_12_1$; *Point group*, 222; a, 6.6719(3) Å; *b*, 7.9424(4) Å; *c*, 39.7008(19) Å; *a*, 90°; *β*, 90°; *γ*, 90°; *z*, 4; $R_1$, 0.0435; $wR_2$, 0.1114; *GOF*, 1.045; *CCDC*: 1961452.

**6DMIQ-T:** *Crystal System*, triclinic; *Space Group*, P-1; *Point group*, -1; a, 10.1028(5) Å; *b*, 10.3242(6) Å; *c*, 13.4088(7) Å; *a*, 101.539(2)°; *β*, 108.960(2)°; *γ*, 106.377(2)°; *z*, 2; $R_1$, 0.0618; $wR_2$, 0.1669; *GOF*, 1.041; *CCDC*: 1960837.

**6DMIQ-4NBS monohydrate 1:** *Crystal System*, monoclinic; *Space Group*, C2/c; *Point group*, 2/m; a, 38.437(2) Å; *b*, 7.1832(5) Å; *c*, 20.0502(13) Å; *a*, 90°; *β*, 121.085(3)°; *γ*, 90°; *z*, 8; $R_1$, 0.0479; $wR_2$, 0.1381; *GOF*, 1.040; *CCDC*: 1916881.

**6DMIQ-4NBS monohydrate 2:** *Crystal System*, monoclinic; *Space Group*, $P2_1/c$;

*Point group*, 2/m; a, 17.8624(4) Å; *b*, 8.1056(2) Å; *c*, 17.3004(4) Å; *a*, 90°; *β*, 110.784°; *γ*, 90°; *z*, 4; $R_1$, 0.0484; $wR_2$, 0.1314; *GOF*, 1.083; *CCDC*: 1916886

**DACS-T:** *Crystal System*, triclinic; *Space Group*, P-1; *Point group*, -1; a, 9.7592(5) Å; *b*, 10.6361(5) Å; *c*, 13.0359(6) Å; *a*, 109.272(3)°; *β*, 99.244(3)°; *γ*, 108.409(3)°; *z*, 2; $R_1$, 0.0396; $wR_2$, 0.1118; *GOF*, 1.040; *CCDC*: 1963594.

**DACS-4NBS:** *Crystal System*, monoclinic; *Space Group*, $P2_1/c$; *Point group*, 2/m; a, 7.5802(6) Å; *b*, 17.0433(13) Å; *c*, 17.5161(14) Å; *a*, 90°; *β*, 91.416(6); *γ*, 90°; *z*, 4; $R_1$, 0.0473; $wR_2$, 0.1212; *GOF*, 1.124; *CCDC*: 1964071

**6MNEP-4CF3:** *Crystal System*, monoclinic; *Space Group*, Pn; *Point group*, m; a, 7.8208(3) Å; *b*, 7.1973(3) Å; *c*, 19.9675(8) Å; *a*, 90°; *β*, 96.700(2)°; *γ*, 90°; *z*, 2; $R_1$, 0.0278; $wR_2$, 0.0727; *GOF*, 1.054; *CCDC*: 1960849.

**6MNEP-3NBS:** *Crystal System*, monoclinic; *Space Group*, $P2_1/c$; *Point group*, 2/m; a, 19.6595(7) Å; *b*, 6.4297(2) Å; *c*, 17.8266(6) Å; *a*, 90°; *β*, 104.903(2)°; *γ*, 90°; *z*, 2; $R_1$, 0.0383; $wR_2$, 0.1015; *GOF*, 1.046; *CCDC*: 1960848.

**6MEIQE-4NBS:** *Crystal System*, triclinic; *Space Group*, P-1; *Point group*, -1; a, 7.085(3) Å; *b*, 7.315(2) Å; *c*, 22.030(7) Å; *a*, 90.112(9)°; *β*, 96.227(10)°; *γ*, 92.400(18)°; *z*, 2; $R_1$, 0.0338; $wR_2$, 0.0859; *GOF*, 1.032; *CCDC*: 1973431.

**MBDM-N2S:** *Crystal System*, triclinic; *Space Group*, P-1; *Point group*, -1; a, 9.6916(4) Å; *b*, 10.6359(5) Å; *c*, 11.1871(5) Å; *a*, 78.992(2)°; *β*, 79.976(2)°; *γ*, 89.669(2)°; *z*, 2; $R_1$, 0.0317; $wR_2$, 0.0828; *GOF*, 1.049; *CCDC*: 1960838.

**MBDME-3NBS:** *Crystal System*, monoclinic; *Space Group*, $P2_1/c$; *Point group*, 2/m; a, 6.3747(2) Å; *b*, 38.0176(14) Å; *c*, 8.8064(3) Å; *a*, 90°; *β*, 92.289(2)°; *γ*, 90°; *z*, 4; $R_1$, 0.0365; $wR_2$, 0.0912; *GOF*, 1.063; *CCDC*: 1960839.

**MBDME-4NBS:** *Crystal System*, orthorhombic; *Space Group*, $P2_12_12_1$; *Point group*, 222; a, 6.7363(3) Å; *b*, 8.1126(4) Å; *c*, 39.4951(19) Å; *a*, 90°; *β*, 90°; *γ*, 90°; *z*, 4; $R_1$, 0.0267; $wR_2$, 0.0685; *GOF*, 1.062; *CCDC*: 1960840.

**MBDME-CBS:** *Crystal System*, orthorhombic; *Space Group*, $P2_12_12_1$; *Point group*, 222; a, 6.8059(2) Å; *b*, 7.9943(3) Å; *c*, 39.4102(13) Å; *a*, 90°; *β*, 90°; *γ*, 90°; *z*, 4; $R_1$, 0.0280; $wR_2$, 0.0726; *GOF*, 1.035; *CCDC*: 1960847.

**MBDME-N2S:** *Crystal System*, triclinic; *Space Group*, P-1; *Point group*, -1; a, 9.7501(6) Å; *b*, 10.9056(6) Å; *c*, 11.4648(6) Å; *a*, 77.261(3)°; *β*, 79.382(4)°; *γ*, 81.917(3)°; *z*, 2; $R_1$, 0.0311; $wR_2$, 0.0834; *GOF*, 1.021; *CCDC*: 1960841.

**6DMIQE-4NBS:** *Crystal System*, triclinic; *Space Group*, P-1; *Point group*, -1; a, 7.5893(7) Å; *b*, 13.5028(11) Å; *c*, 23.829(2) Å; *a*, 95.198(5)°; *β*, 92.280(6)°; *γ*, 99.555(7)°; *z*, 4; $R_1$, 0.0410; $wR_2$, 0.1105; *GOF*, 1.064; *CCDC*: 1916880.

**6DMIQE-3NBS:** *Crystal System*, triclinic; *Space Group*, P-1; *Point group*, -1; a, 8.2165(3) Å; *b*, 9.5708(5) Å; *c*, 15.9375(7) Å; *a*, 97.645(4)°; *β*, 92.675(4)°; *γ*, 93.859(3)°; *z*, 2; $R_1$, 0.0542; $wR_2$, 0.1395; *GOF*, 1.047; *CCDC*: 1916882.

**6DMIQE-CBS:** *Crystal System*, triclinic; *Space Group*, P-1; *Point group*, -1; a, 8.0643(5) Å; *b*, 10.0456(6) Å; *c*, 14.7344(9) Å; *a*, 95.018(3)°; *β*, 96.726(3)°; *γ*, 92.402(3)°; *z*, 2; $R_1$, 0.0357; $wR_2$, 0.0916; *GOF*, 1.049; *CCDC*: 1916884.

**6DMIQE-TMS:** *Crystal System*, triclinic; *Space Group*, P-1; *Point group*, -1; a, 8.6019(5) Å; *b*, 10.1226(6) Å; *c*, 15.5819(8) Å; *a*, 95.347(4)°; *β*, 104.070(4)°; *γ*, 105.448(4)°; *z*, 2; $R_1$, 0.0469; $wR_2$, 0.1172; *GOF*, 1.030; *CCDC*: 1916885.

**6DMIQE-I:** *Crystal System*, orthorhombic; *Space Group*, Pbca; *Point group*, mm2; a, 12.7754(6) Å; *b*, 8.5188(5) Å; *c*, 35.3048(16) Å; *a*, 90°; *β*, 90°; *γ*, 90°; *z*, 8; $R_1$, 0.0422; $wR_2$, 0.1041; *GOF*, 1.047; *CCDC*: 1916883.

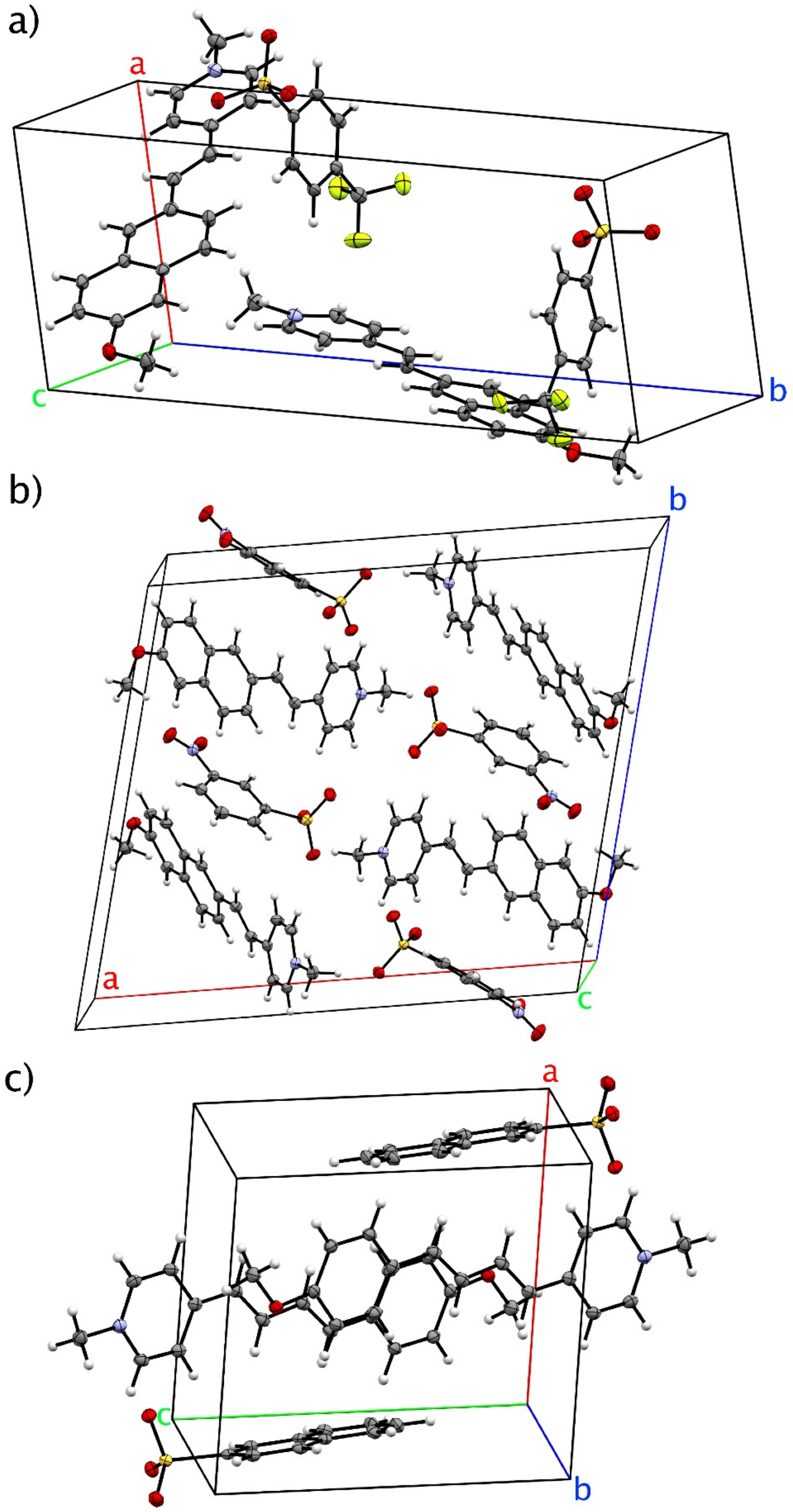

**Figure 5.9** 6MNEP and MBDM cations paired with different anions, a) 6MNEP-4TFS, b) 6MNEP-3NBS, and c) MBDM-N2S.

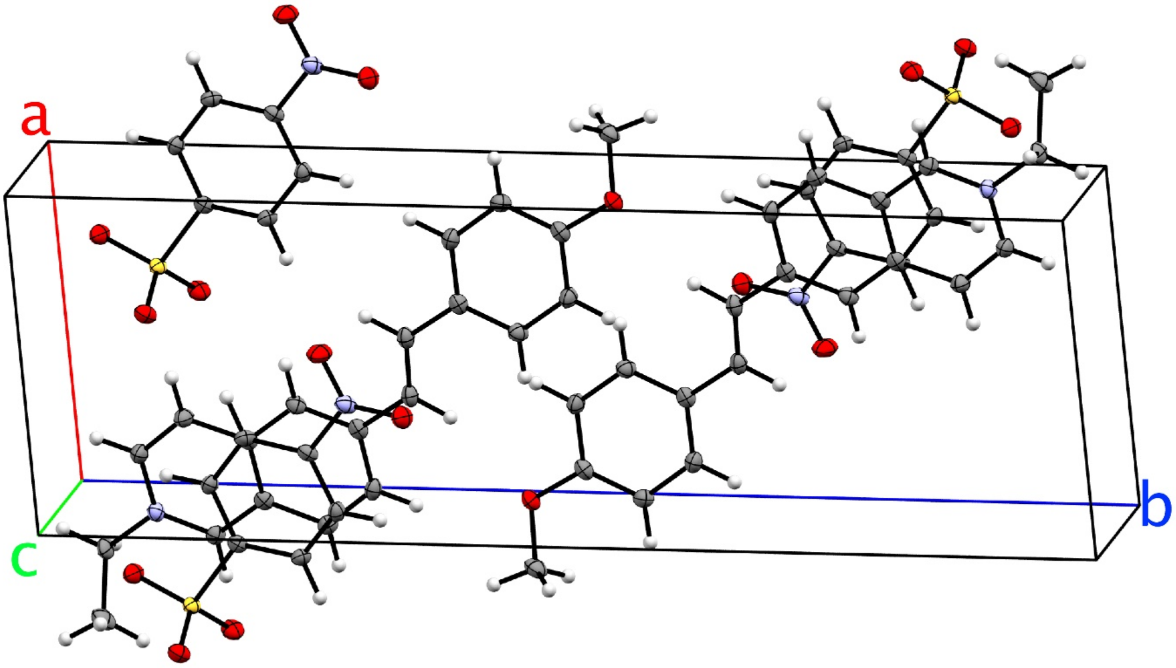

**Figure 5.10** 6MEIQE cation paired with different anions, a) 6MEIQE-4NBS

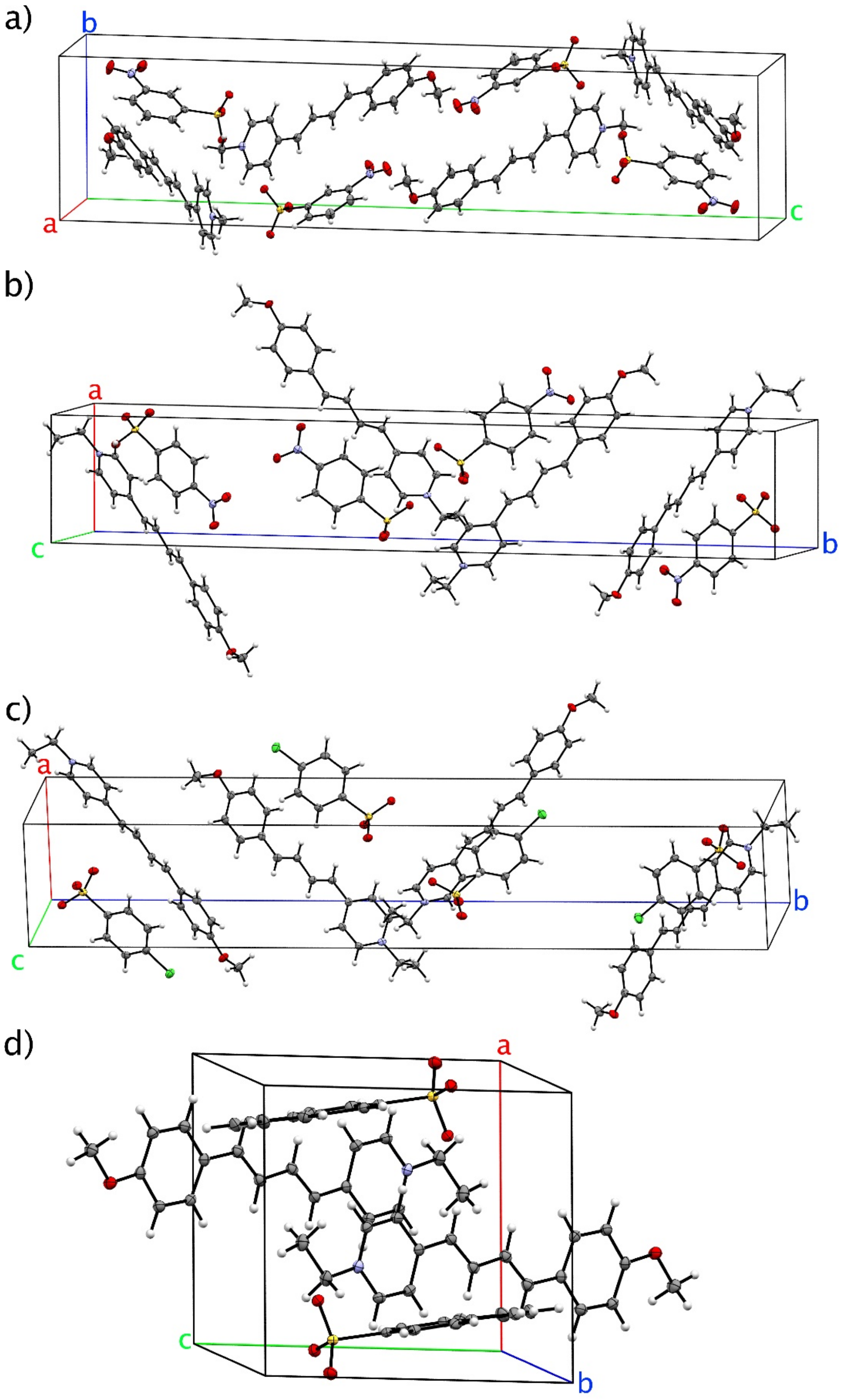

**Figure 5.11** MBDME cation paired with different anions, a) MBDME-3NBS, b) MBDME-4NBS, c) MBDME-CBS, and d) MBDME-N2S

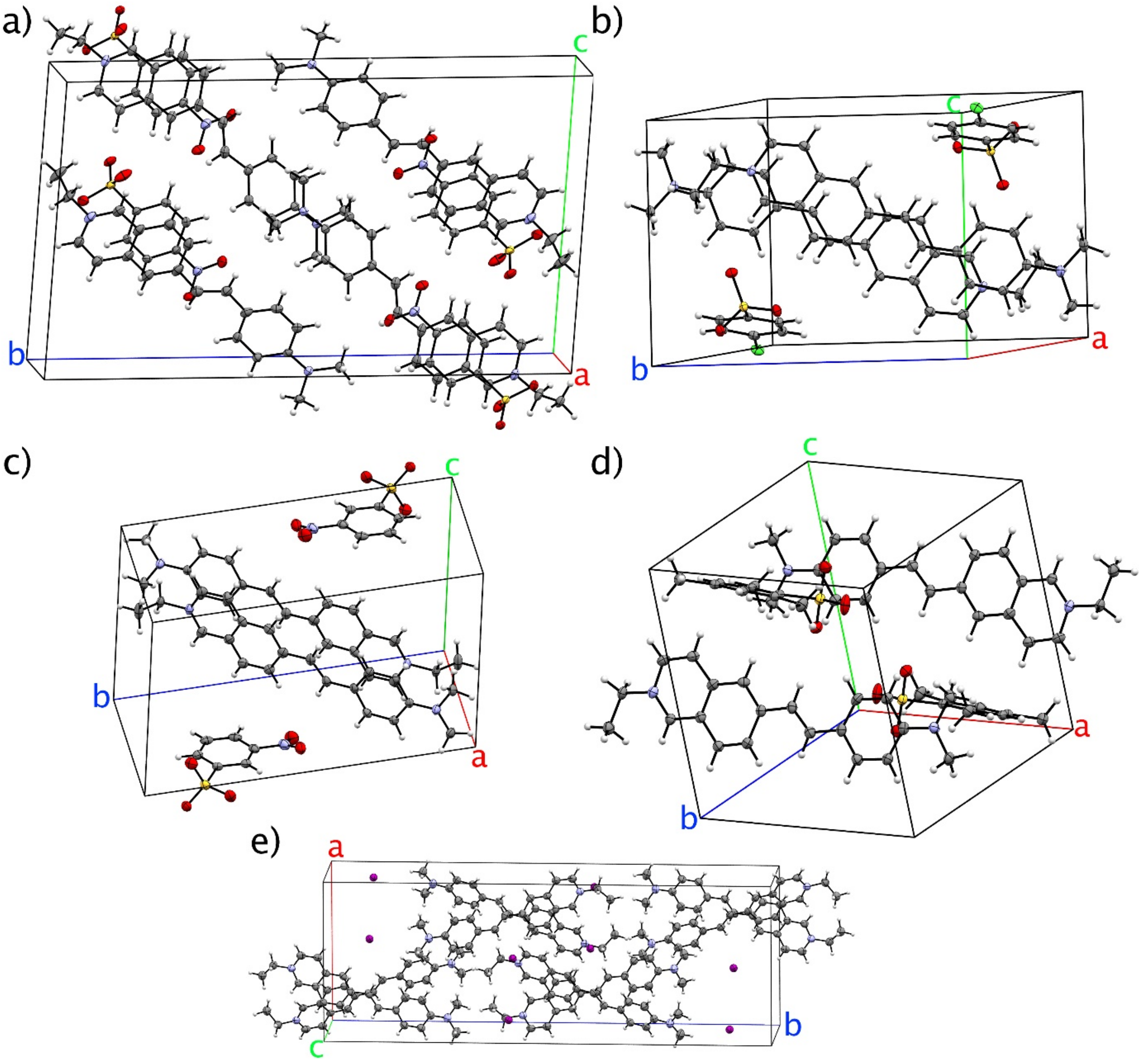

**Figure 5.12** 6DMIQE cation paired with different anions, a) 6DMIQE-4NBS, b) 6DMIQE-CBS, c) 6DMIQE-3NBS, d) 6DMIQE-TMS, and e) 6DMIQE-I.

## 5.7 References

[1] J. Yin, L. Li, Z. Yang, M. Jazbinsek, X. Tao, P. Günter, H. Yang, *Dyes and Pigments* **2012**, 94, 120.

[2] Z. Yang, L. Mutter, M. Stillhart, B. Ruiz, S. Aravazhi, M. Jazbinsek, A. Schneider, V. Gramlich, P. Guenter, *Advanced Functional Materials* **2007**, 17, 2018; Z. Yang, M. Jazbinsek, B. Ruiz, S. Aravazhi, V. Gramlich, P. Günter, *Chemistry of materials* **2007**, 19, 3512; Z. Yang, S. Aravazhi, A. Schneider, P. Seiler, M. Jazbinsek, P. Günter, *Advanced Functional Materials* **2005**, 15, 1072; J. Ogawa, S. Okada, Z. Glavcheva, H. Nakanishi, *Journal of Crystal Growth* **2008**, 310, 836; R. J. Vijay, N. Melikechi, T. Thomas, R. Gunaseelan, M. A. Arockiaraj, P. Sagayaraj, *Journal of Crystal Growth* **2012**, 338, 170.

[3] B. Ruiz, Z. Yang, V. Gramlich, M. Jazbinsek, P. Günter, *Journal of Materials Chemistry* **2006**, 16, 2839.

[4] T. P. Radhakrishnan, *Accounts of Chemical Research* **2008**, 41, 367.

[5] M. Kitazawa, R. Higuchi, M. Takahashi, T. Wada, H. Sasabe, *Applied physics letters* **1994**, 64, 2477.

[6] Z. Yang, L. Mutter, M. Stillhart, B. Ruiz, S. Aravazhi, M. Jazbinsek, A. Schneider, V. Gramlich, P. Günter, *Advanced Functional Materials* **2007**, 17, 2018.

[7] S.-H. Lee, M. Jazbinsek, C. P. Hauri, O. P. Kwon, *CrystEngComm* **2016**, 18, 7180.

[8] R. W. Boyd, *Nonlinear optics*, Elsevier, **2003**.

[9] H. S. Nalwa, S. Miyata, *Nonlinear optics of organic molecules and polymers*, CRC press, **1996**.

[10] S. H. Lee, B. J. Kang, J. S. Kim, B. W. Yoo, J. H. Jeong, K. H. Lee, M. Jazbinsek, J. W. Kim, H. Yun, J. Kim, Y. S. Lee, F. Rotermund, O.-P. Kwon, *Advanced Optical Materials* **2015**, 3, 756.

[11] P. Y. Han, M. Tani, F. Pan, X. C. Zhang, *Optics Letters* **2000**, 25, 675.

[12] F. D. J. Brunner, O. P. Kwon, S.-J. Kwon, M. Jazbinšek, A. Schneider, P. Günter, *Optics express* **2008**, 16, 16496.

[13] F. D. J. Brunner, S.-H. Lee, O. P. Kwon, T. Feurer, *Optical Materials Express* **2014**, 4, 1586.

[14] P. J. Kim, J. H. Jeong, M. Jazbinsek, S. B. Choi, I. H. Baek, J. T. Kim, F. Rotermund, H. Yun, Y. S. Lee, P. Günter, *Advanced Functional Materials* **2012**, 22, 200.

[15] G. A. Valdivia-Berroeta, E. W. Jackson, K. C. Kenney, A. X. Wayment, I. C. Tangen, C. B. Bahr, S. J. Smith, D. J. Michaelis, J. A. Johnson, *Advanced Functional Materials* **2019**, 1904786.

[16] S. J. Sundaram, J. V. Ramaclus, P. Antony, M. Jaccob, P. Sagayaraj, *New Journal of Chemistry* **2018**, 42, 18865.

[17] K. Tsuji, N. Nishimura, X.-M. Duan, S. Okada, H. Oikawa, H. Matsuda, H. Nakanishi, *Bulletin of the Chemical Society of Japan* **2005**, 78, 180.

[18] S.-J. Kwon, O. P. Kwon, J.-I. Seo, M. Jazbinsek, L. Mutter, V. Gramlich, Y.-S. Lee, H. Yun, P. Günter, *The Journal of Physical Chemistry C* **2008**, 112, 7846.

[19] G. A. Valdivia-Berroeta, L. K. Heki, E. A. McMurray, L. A. Foote, S. H. Nazari, L. Y. Serafin, S. J. Smith, D. J. Michaelis, J. A. Johnson, *Advanced Optical Materials* **2018**, 1800383.

[20] C. U. Jeong, B. J. Kang, S. H. Lee, S. C. Lee, W. T. Kim, M. Jazbinsek, W. Yoon, H. Yun, D. Kim, F. Rotermund, O.-P. Kwon, *Advanced Functional Materials* **2018**, 1801143.

[21] S. Guan, X. Wang, Y. Li, T. Tian, G. Xu, S. Yuan, B. Cai, *Crystal Growth & Design* **2019**, 19, 780.

[22] G. M. Sheldrick, *Acta Crystallographica Section A: Foundations and Advances* **2015**, 71, 3.

[23] P. Müller, *Crystallography Reviews* **2009**, 15, 57.

# Chapter 6 Ongoing work and future directions

## 6.1 Overview

In this chapter, the ongoing experiments to characterize EHPSI-4NBS as a THz generator with improved capabilities compared with other state of the art organic crystals are discussed. Additionally, research related to early prediction of non-centrosymmetric crystals is also reviewed. Finally, we discuss the ongoing efforts to find new non-centrosymmetric organic crystals using the Cambridge Crystallographic Database.

## 6.2 EHPSI-4NBS THz generation characterization

The novel THz generating crystal EHPSI-4NBS, presented in chapter 4 of this dissertation, has proven to be promising alternative to other generating crystals such as DAST,[1] OH1,[2] BNA,[3] and HMQ-TMS.[4] **Figure 6.1** shows a grown crystal of EHPSI-4NBS and a polished and mounted crystal that was tested for THz generation

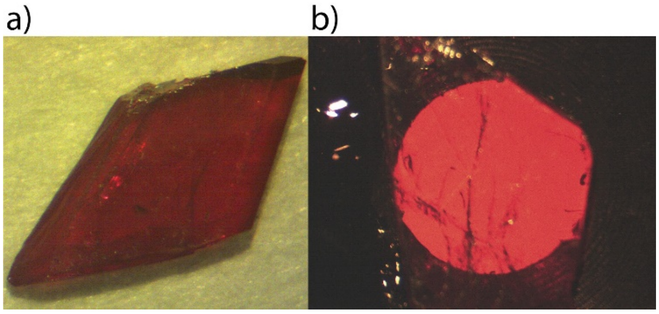

**Figure 6.1** EHPSI-4NBS crystal pictures. a) As-grown crystal of EHPSI-4NBS and b) 350 µm thick crystal mounted on a 3.0 mm diameter aperture.

The obtained THz generation spectrum of EHPSI-4NBS is compared with DAST, OH1, BNA, HMQ-TMS, and the inorganic standard GaP in **Figure 6.2.** EHPSI-4NBS shows improved generation intensity and profile specially from 0 to 3.5 THz, where the new crystal outperforms all the other organic crystals.

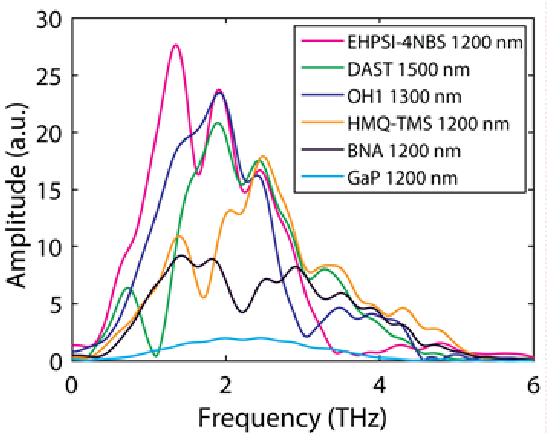

**Figure 6.2** THz generation of EHPSI-4NBS (pink) compared with DAST(green), OH1 (blue), HMQ-TMS (orange), BNA (black) and GaP (light blue).

Additional characterization studies are being performed in our lab to characterize the optical properties of EHPSI-4NBS in the THz and IR regions. As shown in Chapter 3, with this data the THz spectrum of EHPSI-4NBS can be modeled and its applicability under different pumping frequencies and crystal thicknesses can be predicted.

## 6.3 Machine Learning to predict Non-centrosymmetric crystals.

The fabrication of new THz generating crystals is still limited by the difficulty of finding organic molecules that can pack in non-centrosymmetric configurations in the solid state. To solve this problem, in this dissertation we presented the addition of an extra carbon in the quaternary nitrogen of EHPSI and OHP cations. However, as explained in Chapter 4 and 5, this strategy doesn't produce the expected results in molecules containing non-hydrogen bonding electron donating groups. In order to find a more universal approach, we are currently working on developing a Machine Learning[5] based prediction tool that will enables us to asses if a new molecule will feature non-centrosymmetric packing before we spend time and resources on the organic synthesis of potential candidates. Machine Learning is a promising alternative for this task due to its proven ability to predict crystalline space groups using simple properties in inorganic materials.[6]

## 6.4 Development of new neutral organic crystals for THz generation

The novel THz generating molecules presented in this dissertation are classified as organic salts and therefore they contain cations and anions in their structure. However only the cation is active for THz generation and the main role of the anion is to induce non-centrosymmetry and improve the crystallization behavior of the material. The extra volume occupied by the anion reduces the number of active THz generating molecules per unit of volume and therefore lowers the THz output. Neutral crystals such as OH1 and BNA are exclusively formed by active THz generating molecules due to the absence of co-crystallized molecules. This improves the molecular density in the solid state, and these crystals, despite their lower hyperpolarizability compared with organic salts, have shown THz generated electric fields in the same order of magnitude as DAST, HMQ-TMS, and EHPSI-4NBS, as shown in **Figure 6.3**.

We are currently developing methods to improve the crystallization behavior of OH1 and BNA crystals and at the same time working to develop new neutral crystals that can be useful for THz generation. To hasten this process, we are working on new methods to find already existing non-centrosymmetric crystals in the Cambridge Crystallographic Data Center. Then the hyperpolarizability for these compounds can be calculated and the most promising candidates can be synthesized and potentially characterized for THz generation.

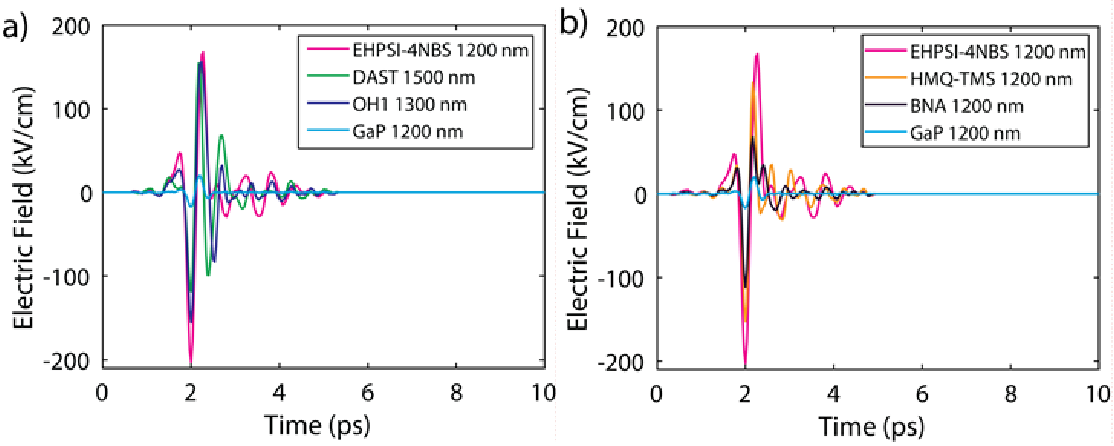

**Figure 6.3** Generated THz electric fields of EHPSI-4NBS (pink) compared with DAST(green), OH1 (blue), HMQ-TMS (orange), BNA (black) and GaP (light blue)

## 6.5 Summary

For this dissertation, we have successfully developed new organic crystals for THz generation. These crystals are being used to improve and explore new applications of THz radiation similar to the examples provided in Chapter 1. The novel EHPSI-4NBS crystal is a promising alternative to state-of-the-art crystals such as DAST, OH1, and HMQ-TMS, due to stronger generated fields and broad spectrum.

## 6.6 References

[1] F. Pan, M. S. Wong, C. Bosshard, P. Günter, *Advanced Materials* **1996**, 8, 592.

[2] F. D. J. Brunner, O. P. Kwon, S.-J. Kwon, M. Jazbinšek, A. Schneider, P. Günter, *Optics express* **2008**, 16, 16496.

[3] C. Bernerd, P. Segonds, J. Debray, T. Notake, M. Koyama, H. Minamide, H. Ito, B. Boulanger, *Optics letters* **2018**, 43, 1818.

[4] F. D. J. Brunner, S.-H. Lee, O. P. Kwon, T. Feurer, *Optical Materials Express* **2014**, 4, 1586.

[5] T. G. Dietterich, *AI magazine* **1997**, 18, 97.

[6] E. V. Podryabinkin, E. V. Tikhonov, A. V. Shapeev, A. R. Oganov, *Physical Review B* **2019**, 99, 064114.